

博士論文

**Ion Transport in Ordered Nanoporous Structures**

(規則性ナノ細孔内部のイオン移動に関する研究)

黄 峻浩

# Ion Transport in Ordered Nanoporous Structures

(規則性ナノ細孔内部のイオン移動に関する研究)

Approved, Thesis committee:

---

Daiguji, Hirofumi  
Professor, Department of Mechanical Engineering  
The University of Tokyo, Japan

---

Jimbo, Yasuhiko  
Professor, Department of Human and Engineered Environmental Studies  
The University of Tokyo, Japan

---

Suzuki, Yuji  
Professor, Department of Mechanical Engineering  
The University of Tokyo, Japan

---

Endo, Akira  
Leader, Energy-Efficient Chemical Systems Group  
National Institute of Advanced Industrial Science and Technology (AIST), Japan

---

Torii, Toru  
Professor, Department of Human and Engineered Environmental Studies  
The University of Tokyo, Japan

## **Declaration**

I, hereby declare that the investigation presented in the thesis entitled “Ion transport in ordered nanoporous structures” submitted to The University of Tokyo, Japan for the award of Doctoral degree is the record of work carried out by me during the period from April 2011 to March 2014 under the supervision of Prof. Hirofumi Daiguji. The work is original and has not been submitted earlier as a whole or in part for a degree at this or any other academic institutions.

# ABSTRACT

Ion Transport in Ordered Nanoporous structures

By

Junho Hwang

The University of Tokyo

Professor Hirofumi Daiguji, Supervisor

Transport of ions and molecules in nanochannels/nanopores has attracted great interest and been extensively investigated to understand the various functions of ion channels. Nanofluidic system with dimensions ranging from 1 to 100 nm, which is comparable to the Debye length that characterizes the range of electrostatic interactions in aqueous solution, exhibits surface charge governed ion transport phenomenon which is not observed in microfluidic system. So far, the majority of studies have been performed in nanofluidic channels with dimensions larger than ~10 nm, since it is fairly challenging to fabricate nanochannels whose dimensions are less than 10 nm by means of approaches that utilize conventional nanolithography. In this thesis, we suggest a new possibility of developing nanofluidic devices using mesoporous silica with well-ordered nanoporous structures synthesized via bottom-up nanofabrication technique and focuses on phenomena that arise in sub-10 nm nanochannel.

First, we synthesized mesoporous silica SBA-16 thin films with highly ordered three-dimensional cubic structures on a Si substrate via the dip-coating method based on evaporation-induced self-assembly and demonstrated ion transport phenomena in nanofluidic device fabricated using those films. When the Debye length of the aqueous solution clearly exceeded the spherical pore radius (~9.5 nm), the measured ionic current exhibited a

nonlinear behavior with increasing an electric potential bias applied. The nonlinear behavior of ionic currents at low concentration can be reasonably attributed to the electric potential barrier created in pores measuring a few nanometers in diameter ( $\sim 2.3$  nm). To quantitatively discuss nonlinear ionic current behavior due to the electric potential barrier, we established the modified Poisson-Nernst-Planck equation, which was applied to express the discreteness of molecules in nanopores, as the governing equation to describe ion transport in nanopores below  $\sim 5$  nm in diameter and successfully analyzed by means of continuum dynamics instead of stochastic or molecular dynamics.

In addition, proton transport behavior through mesopores of SBA-16 showed considerably different result compared to conventional nanofluidic system. When proton current was measured in surface-governed regime, the conductance generally decreases with increasing concentrations of aqueous solution because the surface charge density on the inner surface of mesopores decreases by protonation of silanol groups. However, in the case of nanopores with a few nanometers in diameter, the conductance increases in spite of active protonation. Since the dissociated proton and silanol groups were very close to each other, proton close to silanol sites also became charge carriers and might transport by hopping between silanol sites. The electric potential barrier was therefore lowered, but the density of proton did not decrease appreciably, thus increasing the conductance.

Finally, we developed nanofluidic devices embedded mesoporous silica SBA-15 thin films with two-dimensional hexagonal mesoporous silica SBA-15 thin film with dimensions ranging of  $\sim 6$  nm. Since mesoporous silica SBA-16 has limitations such as complex three-dimensional geometry and too small sized nanopores close to  $\sim 2$  nm, it is somewhat difficult to apply commonly general conditions. Therefore, sub-10 nm nanofluidic devices with more

simple geometry was required to investigate ion or water transport phenomena of aqueous solution confined in mesopores. Before fabricating nanofluidic devices, we investigated to find the best synthesis condition of SBA-15 thin films suitable for transport studies, because thickness and hexagonal pore-array dimensions of film depends on dip-coating rate. As a result, we found that SBA-15 films produced in draining regime featured the most perfect pore structure of the global one-dimensional pore alignment and local two-dimensional hexagonal pore array because a thin film of dilute solution was formed uniformly and the micelle self-assembly proceeded slowly. And then, we measured ionic current passing through the nanofluidic devices, resulting in a linear behavior independently of the aqueous solution concentrations.

# Table of Contents

Table of Contents.....	iv
List of Figures.....	viii
List of Tables.....	xii
<b>Chapter 1</b> Introduction to Ion Transport in Nanochannel and Fabrication of Nanofluidic Devices.....	1
1.1 Nanofluidics.....	1
1.2 Ion transport in nanochannels.....	2
1.2.1 Surface charge.....	3
1.2.2 Electric double layer at an interface between solid and liquid.....	4
1.2.3 Ion distribution in the EDL.....	7
1.2.4 Electrostatic interaction in nanochannels with dimensions below 100nm..	10
1.2.5 Electrokinetic phenomena in nanochannels.....	12
1.2.5.1 Electroosmosis.....	12
1.2.5.2 Electrophoresis.....	14
1.2.5.3 Streaming potential.....	15
1.3 Fabrication of Nanofluidic devices.....	15
1.3.1 Lithography and MEMs based nanofabrication method.....	17
1.3.2 Sol-gel synthesis based nanofabrication method.....	19
1.3.3 Mesoporous silica thin films.....	21
1.3.4 Synthesis method of mesoporous silica thin films.....	24
1.4 Objective of the thesis.....	27
1.5 Reference.....	32

<b>Chapter 2</b>	<b>Ion Transport in Mesoporous Silica SBA-16 Thin Film with Three-Dimensional Cubic Structures.....</b>	<b>41</b>
2.1	Introduction.....	41
2.2	Synthesis of SBA-16 thin films with 3D cubic structures.....	42
2.3	Fabrication of a device for ionic current measurement.....	46
2.4	Structure of the synthesized SBA-16 thin film.....	48
2.5	Measurement of ionic current.....	49
2.5.1	Ionic current–voltage characteristics.....	50
2.5.2	Influence of immersed time for KCl aqueous solution $I - V$ curves.....	52
2.5.3	Details related to the measurement method of $I - V$ curves.....	54
2.5.4	Influence of solvent evaporation on $I - V$ curves.....	56
2.5.5	Time courses of ionic current.....	58
2.6	Calculation of 3D electric potential distributions.....	62
2.7	Calculation of 1D PNP equations .....	66
2.8	Influence of parameters $C_1$ and $C_2$ on $J - V$ curves.....	71
2.9	Comparison between Experiment and Calculation of Conductance.....	75
2.10	Experimental reproducibility of $I - V$ curves.....	77
2.11	Conclusion.....	79
2.12	Reference.....	80
<b>Chapter 3</b>	<b>Proton Transport in Mesoporous Silica SBA-16 Thin film.....</b>	<b>83</b>
3.1	Introduction.....	83
3.2	Measurement of proton current.....	85
3.2.1	Effect of concentration on $I - V$ curves of HCl and KCl aqueous solutions..	85
3.2.2	Effect of concentration on $I - t$ curves of HCl and KCl aqueous solutions...	89

3.2.3 Comparative analysis of $G-n$ curves of HCl and KCl aqueous solutions....	92
3.3 Calculation method of 1D PNP equations and $J_{H^+} - V$ curves.....	96
3.4 Restoration of electric potential barriers by deprotonation reaction.....	100
3.5 Conclusion.....	101
3.6 Reference.....	103
<b>Chapter 4</b> Thickness and Hexagonal Pore–Array Dimensions of SBA-15 Thin Film.....	105
4.1 Introduction.....	105
4.2 Preparation of SBA-15 mesoporous silica thin films.....	109
4.3 Characterization of SBA-15 mesoporous silica thin films.....	110
4.3.1 FE-SEM and TEM measurements.....	111
4.3.2 XRR measurements.....	114
4.3.3 XRD measurements.....	116
4.4 Model of the thickness of films synthesized by dip-coating.....	117
4.4.1 Film thickness in the capillarity regime.....	117
4.4.2 Film thickness in the draining regime.....	118
4.4.3 Combined model.....	119
4.5 1D Alignments and 2D hexagonal arrays of pores .....	119
4.6 Interplanar spacing and pore sizes .....	123
4.7 Interplanar spacing of $d(100)$ before and after calcinations.....	125
4.8 Conclusion.....	127
4.9 Reference.....	129
<b>Chapter 5</b> Fabrication of Nanofluidic Device Embedded SBA-15 (On-going Study).....	134

5.1	Introduction.....	134
5.2	Fabrication of Nanofludic device that has SBA-15 thin film.....	135
5.3	Measurement of ionic current.....	139
5.4	Ionic current–voltage characteristic.....	140
5.5	Conclusion.....	143
5.3	Reference.....	144
<b>Chapter 6</b>	<b>Conclusions.....</b>	<b>146</b>
<b>APPENDIX A:</b>	<b>TEM specimen preparation techniques.....</b>	<b>151</b>

## List of Figures

Figure 1.1 Gouy-Chapman-Stern model of the interface solid-electrolyte with the corresponding potential distribution versus the distance $z$ from the wall. $\psi_s$ is a negative surface potential. Reproduced from Schoch, R. et al. [19].....	6
Figure 1.2 Positively and negatively charged ion distribution of (a) the Gouy-Chapman model and (b) the Debye-Hückel approximation model. Reproduced from Hunter, R. et al. [36].....	9
Figure 1.3 Surface charge effects in (a) nanochannels and (b) microchannels.....	11
Figure 1.4 Schematic image showing the electroosmotic flow in a negatively charged channel within EDL.....	13
Figure 1.5 Schematic overview of different nanostructured materials that can be obtained via a sol-gel process. Reproduced from Lawrence Livermore National Laboratory image.....	21
Figure 1.6 TEM image of several MCM-41 materials having pore sizes of (a) 20, (b) 40, (c) 65, and (d) 100 Å. Reproduced from Beck, J. et al. [84].....	23
Figure 1.7 Micelle structures A. sphere, B. cylinder, C. planar bilayer, D. reverse micelles, E. bicontinuous phase, F. liposomes. Reproduced from Soler-Illia, G. et al.[93].....	25
Figure 1.8 Schematic phase diagram for $C_{16}TMABr$ in water. CMC is exaggerated to higher concentration. Reproduced from Raman, N. et al. [94].....	26
Figure 1.9 Dip-coating process to synthesize the a well-ordered mesostructured silica thin film.....	27
Figure 2.1(a) FE-SEM image of an SBA-16 film synthesized on a Si substrate on the top surface and (b) FE-TEM image of the film in cross section.....	45
Figure 2.2 Schematic of a device for ionic current measurement. (a) Top view, (b) side view, and (c) general view.....	48
Figure 2.3 Schematic structure of the synthesized SBA-16 thin film.....	49
Figure 2.4 Ionic current vs. electric potential bias ( $I - V$ ) curves of an SBA-16 thin film filled with KCl aqueous solutions with concentrations of $10^{-4}$ , $10^{-3}$ , $10^{-2}$ , $10^{-1}$ , and 1M.....	51
Figure 2.5 The conductance vs. ion concentration ( $G - n$ ) curve.....	52
Figure 2.6 Conductance vs. immersed time ( $G - t$ ) curves for KCl aqueous solutions of $10^{-4}$ ,	

$10^{-3}$ , $10^{-2}$ , $10^{-1}$ , and 1 M concentrations.....	54
Figure 2.7 Conductance vs. number of repeat measurements ( $G - N$ ) curves for KCl aqueous solutions of $10^{-4}$ , $10^{-3}$ , $10^{-2}$ , $10^{-1}$ , and 1 M concentrations.....	56
Figure 2.8 Ionic current vs. electric potential ( $I - V$ ) curves of two consecutive measurements for $10^{-4}$ and $10^{-3}$ M KCl aqueous solutions.....	57
Figure 2.9(a) Time course of ionic current passing through an SBA-16 thin film filled with either a $10^{-4}$ , $10^{-3}$ , $10^{-2}$ , $10^{-1}$ , or 1 M KCl aqueous solution and (b) the time course of the applied electric potential.....	58
Figure 2.10 Equivalent electric circuit of ion transport in an SBA-16 thin film.....	59
Figure 2.11 Calculation system of a model pore for calculation of 3D electric potential distributions.....	63
Figure 2.12 Calculated electric potential distribution inside three model pores in the $x - z$ plane. (a) a uniform surface charge density of $-10^{-2}$ C m <sup>-2</sup> is assumed to be present on the whole surface, (b) 18 point charges of $e^-$ are distributed on the surface of the spherical pore and 1 point charge is located on the surface of the cylindrical pore, and (c) 18 point charges of $e^-$ are distributed on the surface of the spherical pore.....	64
Figure 2.13 Electric potential profiles along the $z$ -axis for three different models.....	65
Figure 2.14 Calculation system of a model pore for calculation of 1D PNP equation.....	67
Figure 2.15 Calculated $K^+$ current density vs. electric potential bias ( $J - V$ ) curves showing (a) the effect of $C_2$ and (b) the effect of $C_1$ on $J - V$ curves.....	72
Figure 2.16 Calculated $K^+$ current density vs. electric potential bias ( $J - V$ ) curves showing (a) the effect of $C_1$ at $C_2 = 1$ , (b) the effect of $C_2$ and (c) the effect of $C_1$ on $J - V$ curves.....	76
Figure 2.17 Comparison between calculated and experimental results of the conductance vs. ion concentration ( $G - n$ ) curves.....	77
Figure 2.18 The measured $I - V$ curves to confirm reproducibility at $10^{-4}$ M KCl aqueous solution: (a) 1 day, (b) 3 days, (c) 5 days, and (d) standard deviation, respectively.....	78
Figure 3.1 The measured current vs. electric potential bias ( $I - V$ ) curves of (a) KCl and (b) HCl aqueous solutions at (I) low concentrations ( $10^{-7}$ , $10^{-6}$ , and $10^{-5}$ M), (II) intermediate concentrations ( $10^{-4}$ and $10^{-3}$ M), and (III) high concentrations ( $10^{-2}$ , $10^{-1}$ , and 1 M).....	86

Figure 3.2 The measured current vs. electric potential bias ( $I-V$ ) curves of (a) KCl aqueous solutions at $10^{-7}$ , $10^{-4}$ , and $10^{-3}$ M concentrations, and (b) calculated $K^+$ current density vs. electric potential bias ( $J-V$ ) curves.....	88
Figure 3.3 The measured ionic current vs. time ( $I-t$ ) curves of HCl aqueous solutions with concentrations of (a) $10^{-5}$ M and (b) $10^{-3}$ M.....	89
Figure 3.4 Calculated relaxation rate vs. step potential ( $k-V$ ) curves.....	91
Figure 3.5 The measured ionic current vs. time ( $I-t$ ) curves of (a) KCl and (b) HCl aqueous solutions with concentrations of $10^{-4}$ and $10^{-3}$ M.....	92
Figure 3.6 Comparisons between the measured and calculated conductance vs. concentration ( $G-n$ ) curves of (a) KCl and (b) HCl aqueous solutions.....	93
Figure 3.7(a) Calculated $J_{H^+} - V$ curves for five different values of $V_0$ , 6, 15, 30, 60, and 150 mV, and (b) $J_{H^+}$ at $V = 1.0$ mV as a function of $V_0$ .....	99
Figure 3.8 Effect of soaking duration of a nanofluidic device in DI water on current vs. electric potential bias ( $I-V$ ) curves.....	100
Figure 4.1 Cross-sectional FE-SEM (top) and TEM (bottom) images of SBA-15 thin films synthesized on Si substrates at four different withdrawal speeds: (a) 0.02, (b) 0.5, (c) 1.0, and (d) 3.0 $\text{mm s}^{-1}$ . The scale bar is 50 nm.....	111
Figure 4.2 Cross-sectional TEM images of SBA-15 thin films synthesized on Si substrates at four withdrawal speeds: (a) 0.02, (b) 0.5, (c) 1.0, and (d) 3.0 $\text{mm s}^{-1}$ .....	114
Figure 4.3(a) XRR patterns of SBA-15 thin films synthesized on Si substrates at withdrawal speeds: 0.02, 0.05, 0.1, 0.2, 0.5, 1.0, and 3.0 $\text{mm s}^{-1}$ . (b) Film thickness versus withdrawal speed plots.....	115
Figure 4.4(a) XRD patterns of SBA-15 thin films synthesized on Si substrates at seven different withdrawal speeds: 0.02, 0.05, 0.1, 0.2, 0.5, 1.0, and 3.0 $\text{mm s}^{-1}$ . (b) Plots of the interplanar distance [ $d(100)$ ] versus withdrawal speed.....	117
Figure 4.5 The dried film deposited above the meniscus by dip-coating (a) and thin film deposition process in evaporation regime (b).....	120
Figure 4.6. Cross-sectional FE-SEM images of SBA-15 thin films synthesized on Si substrate s at (a) 0.02 and (b) 3.0 $\text{mm s}^{-1}$ under RH 40%.....	122
Figure 4.7 Cross-sectional TEM image of a SBA-15 mesoporous silica thin film synthesized on a (100)-oriented Si substrate at a withdrawal speed of 0.5 $\text{mm s}^{-1}$ . The direct magnification was 500 000.....	124

Figure 4.8 Cross-sectional FE-SEM images of (a) before and (b) after calcination of a SBA-15 thin film synthesized on Si substrates at a withdrawal speed of $3.0 \text{ mm s}^{-1}$ . The scale bar is 50 nm.....	126
Figure 4.9 Plots of the interplanar distance [ $d(100)$ ] versus withdrawal speed before and after calcination.....	126
Figure 5.1 Fabrication process flow of nanofluidic device embedded mesoporous silica SBA-15 thin film.....	136
Figure 5.2 Schematic of nanofludic device layout. A silicon dioxide film deposited onto Si substrate and mesoporous silica thin film is to prevent leakage of aqueous solutions between both reservoirs.....	137
Figure 5.3 Microscope image (top view) and cross-sectional view of the nanofludic device chip combined with the PDMS microfluidic chip.....	138
Figure 5.4 Ionic current vs. electric potential bias ( $I-V$ ) curves of an SBA-15 thin film with KCl aqueous solutions with concentrations of (a) $10^{-5}$ , $10^{-4}$ , $10^{-3}$ and (b) $10^{-2}$ , $10^{-1}$ , 1M.....	140
Figure 5.5 Conductance vs. ion concentration ( $G-n$ ) curve.....	141
Figure 5.6 Interpore distance of mesoporous silica SBA-15 from 2D hexagonal structures..	142

## List of Tables

Table 1.1 Debye length $\lambda_d$ for typical KCl concentrations.....	11
Table 4.1 The interplanar spacing of $d(100)$ in the XRD patterns of film produced at different withdrawal speeds before and after calcinations.....	127

## ACKNOWLEDGEMENTS

It is a big challenge for me to complete my doctoral program at The University of Tokyo. There are many people to whom I would like to thank for helping me coming through the whole procedure. First and foremost, I would like to express my gratitude to my supervisor, Prof. Hirofumi Daiguji for the tremendous amount of support he has given me throughout this work, for his encouragement and enthusiasm which boosted my research work, and for his patience in correcting my scientific and linguistic error. He also taught me how to technically write and talk about research.

I would also like to thank Prof. Yuji Suzuki, Prof. Yasuhiko Jimbo, Prof. Toru Torii, and Dr. Akira Endo for accepting to be in the my Doctoral Examination Committee and for their valuable comments and advised on my thesis work. I am particularly grateful to Dr. Akira Endo for his discussions and continuous supporting on my research.

I would also like to thank Dr. Kataoka Sho for his assistance in synthesizing mesoporous silica SBA-16 thin films. I would also like to thank Mr. Mitsuhiko Yamada for his support in SEM measurement. I also wish to thank all you guys in the lab and the staff of The University of Tokyo during the year for all your help, discussions, support and making life easier.

Especially, I would like to give my special thanks to my parents for their encouraging and support.



# CHAPTER 1

## Introduction to Ion Transport in Nanochannel and Fabrication of Nanofluidic Devices

*This chapter provides an introduction about nanofluidics and ion transport in nanochannels. We also provide an explanation about the surface charge and its related counter-ions concentration profile in a liquid, away from a surface, which is modeled by the electric double layer. Furthermore, we cover different nanofabrication methods (top-down vs. bottom-up approach) for nanofluidic system and the generalities of the materials made from mesoporous silica materials. The motivation, scope and outline of the thesis are presented at the end of this chapter.*

### 1.1 Nanofluidics

Nanofluidics [1–4] is the study and application of fluid flow in and around nanostructures with at least one characteristic dimension which is less than  $\sim 100\text{nm}$ . With advances in the technique for fabricating nanostructures, and in the methods for measurement and analysis at the nanometer scale, nanofluidics has gain special attention in recent years. Compared to existing macro- and microfluidics, nanofluidics has unique features such as the extremely large surface-to-volume ratio, dimensions comparable to the range of various interfacial forces like steric/hydration interactions ( $\sim 1\text{-}2\text{ nm}$ ), van der Waals interactions ( $\sim 1\text{-}$

50 nm), and electrostatic interactions (~1-100 nm) and it has the same scale of biomolecules (proteins and DNA) which play significant roles in biological processes [5, 6].

At nanometer scale, these aforementioned features generate novel transport phenomena that cannot be observed at the macro- and microfluidic system. For instance, a large surface to volume ratio leads to negative pressure of water plugs in nanochannels due to tensile capillary forces [7, 8]; and its scale comparable to biomolecules allows for the separation of single molecules and DNA analysis [9, 10]. In addition, the electrostatic interactions between the charged surface and ions in nanochannels form overlapped electric double layers (EDL), which results in ion perm-selective transport [11]. From these extraordinary features, nanofluidic system has applications in various fields of science and engineering such as highly sensitive biomolecular sensing [12, 13], ion-selective/separation transport [14], and energy conversion and storage [15–17].

## **1.2 Ion transport in nanochannels**

Among various transport phenomena through nanoscale geometries, the ion transport has attracted great interest and has been extensively investigated to understand the various functions of ion channels. The analysis and control of transport phenomena in fluidic nanochannels are essential to effectively apply them to various technologies for biochemical analysis, power generation, and environmental protection.

A better understanding of the ion transport phenomena in confined nanospaces will enable the development of protein or artificial ion channel sensors, which use the selective and sensitive processes of molecular recognition. In addition, this knowledge will lead to the development of various functional materials, including nanopores and/or nanostructures, such as adsorbents, ion exchangers, ionic conductors, catalysts, and permeable materials [18, 19]. Furthermore, the advances in the synthesis, measurement, and analysis of nanotubes and nanochannels have allowed ion and liquid transport to be routinely examined and controlled in spaces with dimensions that range from 10 to 100 nm [20, 21–23].

### 1.2.1 Surface charge

When solid surfaces are in contact with the liquid, they have surface charges which are due to the electron charges of the ions at an interface between the solid and the liquid. The surface charge has a huge influence on the behavior of liquid in nanochannels because the surface-to-volume ratio increases with reducing the scale. Therefore, a dominating parameter in a nanochannel is the negative surface charge density,  $\sigma_s$ ,

$$\sigma_s = \frac{\sum_i q_i}{A}, \quad (1.1)$$

where  $q_i = z_i e$  is the net charge of ion  $i$ ,  $z_i$  is the valence,  $e$  is the electron charge, and  $A$  is the surface area. In general, the surface charge density depends on the

type of ion [24, 25], concentration of aqueous solution [26, 27], and pH value [28–31].

The value of the surface charge density can be experimentally measured by potentiometric acid-base titrations on colloidal dispersions [32]. In the case of a glass or silica material,  $\text{SiO}^-$  and  $\text{Si}^-$  bonds are formed at a glass surface and these dangling bonds react with the hydroxyl groups of the aqueous solution.



However, since all of the bonds do not react with the hydroxyl group, the surface is charged. The degree of dissociation, and thus the surface charge density, results from the equilibrium between the counterions at the glass surface and the free ions in the bulk electrolyte [33].

### **1.2.2 Electric double layer at an interface between solid and liquid**

A solid surface will gain surface charges when brought into contact with a liquid. These surface charges are due to the ionized surface group, absorbed ions, and protonation/ deprotonation and these affect the distribution of ions in the liquid by electrostatic interaction. Oppositely charged ions (counter-ions) to the surface charge are attracted to the surface due to Coulomb force, while the same charges (co-ions) to surface charges are repelled from surface. This screening region is called electrical double layer (EDL).

The double layer refers to two parallel layers of charge created at the solid-liquid interface. The first layer, the surface charge, comprises ions adsorbed onto

the object. The second layer is composed of counter-ions attracted to the surface charge by electrostatic interaction, some of which are bounded while others are mobile. Several models have been introduced to explain EDL for decades. The Helmholtz model, the earliest and simplest, describes the EDL mathematically as a simple capacitor, based on a physical model in which a single layer of ions is adsorbed at the surface [34]. Later Gouy-Chapman model was introduced to describe the EDL as a surface charge and a charged layer in the liquid in which the shielding ions are diffused and the electric potential decreases exponentially away from the surface to the fluid bulk due to the thermal motion of ions, named diffuse layer [35]. However, the Gouy-Chapman model considers the adsorbed ions to the surface as mobile and has problems to describe highly charged EDL. To address this problem, Stern proposed the combination of the Helmholtz and Gouy-Chapman models [36]. He introduced an inner layer called stern layer between the inner Helmholtz plane and the outer Helmholtz to take into account the finite size of the ions. Figure 1.1 shows the Gouy-Chapman-Stern model of the interface solid-liquid [37], which is separated into three layers. The first layer is at the inner Helmholtz plane with its potential  $\psi_i$  and anion is non-hydrated and specially adsorbed on the surface. The second layer called stern layer is located between the inner Helmholtz plane and the outer Helmholtz plane with its potential  $\psi_d$  and it is composed of fully or partially hydrated counter-ions. The third layer is diffuse layer composed of mobile co-ions and counter-ions. The slip plane with the  $\zeta$  potential comprised in the diffuse layer is closely situated near

the outer Helmholtz and is an imaginary plane dividing the fixed ions at the surface from mobile in aqueous solution. In most cases, the  $\zeta$  potential can be approximated by using  $\psi_d$  for practical purpose.

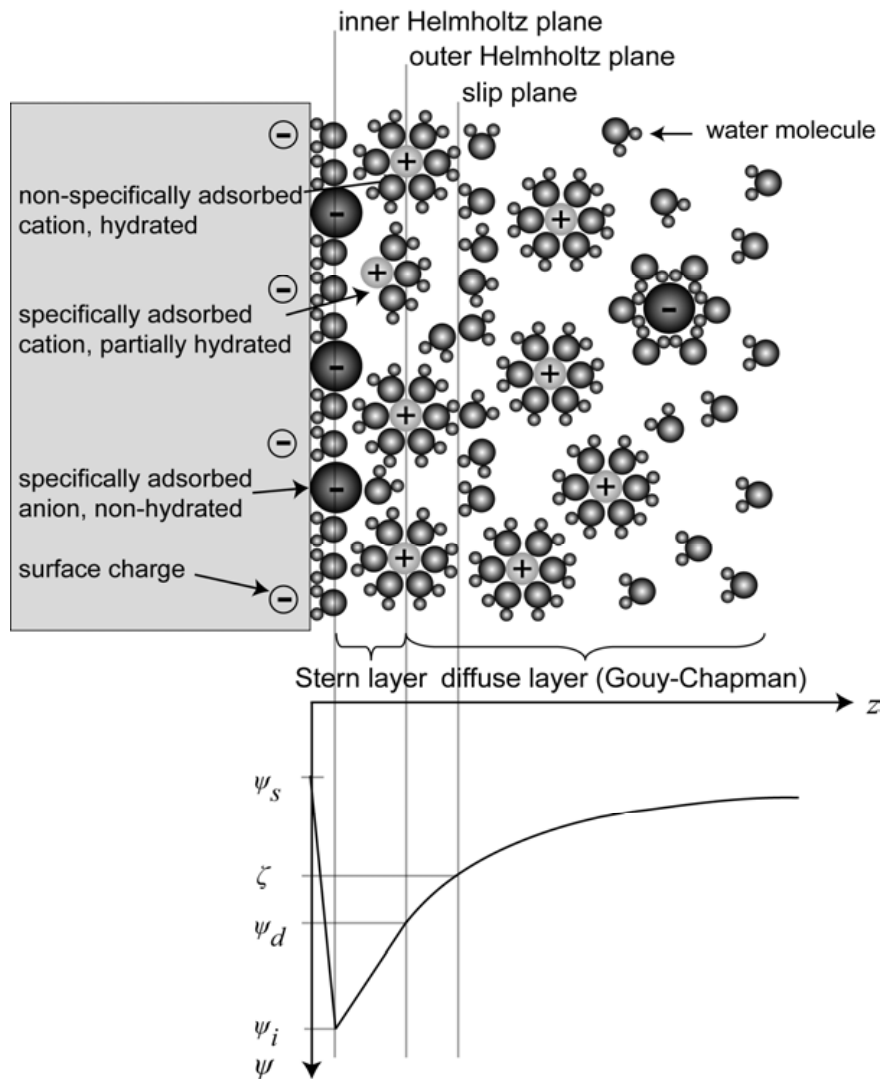


Figure 1.1 Gouy-Chapman-Stern model of the interface solid-electrolyte with the corresponding potential distribution versus the distance  $z$  from the wall.  $\psi_s$  is a negative surface potential. Reproduced from Schoch, R. et al. [19].

### 1.2.3 Ion distribution in the EDL

Before we discuss the ion distribution in the EDL, we need to consider the potential distribution. First, we introduce the electrochemical potential of ion  $i$ ,  $\tilde{\mu}_i$ , in a liquid phase under constant pressure and temperature conditions [5].

$$\tilde{\mu}_i = \underline{\mu}_i + z_i F \psi = \underline{\mu}_i^0 + RT \ln\left(\frac{\gamma_a c_i}{c^0}\right) + z_i F \psi, \quad (1.3)$$

where  $\underline{\mu}_i$  is the chemical potential,  $F$  is the Faraday constant,  $\psi$  is the electric potential,  $\underline{\mu}_i^0$  is the standard chemical potential of ion  $i$  at constant pressure and temperature,  $R$  is the gas constant,  $T$  is the absolute temperature,  $\gamma_a$  is the activity coefficient,  $c_i$  is the molar concentration of ion  $i$ ,  $c^0$  is the standard molarity of 1 mol/l,  $z_i$  is the valence of charge. At equilibrium, the entire electrochemical potential of the ions is the same, i.e.  $\nabla \tilde{\mu}_i = 0$ , [36]

$$\nabla \underline{\mu}_i = -z_i F \nabla \psi \quad (1.4)$$

By substituting the chemical potential into Eq. (1.4) and integrating from a point in the bulk solution where  $\psi = 0$  and  $n_i = n_i^\infty$  ( $n_i^\infty = 1000 N_A c^i$  is the average volume density), we can derive the Boltzmann equation for the local concentration of each type of ion within the EDL.

$$n_i = n_i^\infty \exp\left(-\frac{z_i e \psi}{k_B T}\right), \quad (1.5)$$

where  $k_B$  is the Boltzmann constant. The volume charge density  $\rho$  of all species of ion adjacent to the surface is defined as follows.

$$\rho = \sum_i n_i z_i e \quad (1.6)$$

Also we can apply the Poisson equation for the net excess charge density at a specific distance from the surface. The Poisson equation is

$$\nabla^2 \psi = \frac{d^2 \psi}{dz^2} = -\frac{\rho}{\varepsilon_0 \varepsilon_r} \quad (1.7)$$

where  $z$  is the normal direction to the surface,  $\varepsilon_0$  is the permittivity of vacuum, and  $\varepsilon_r$  is the dielectric constant of the water. By substituting Eq.(1.5) and Eq.(1.6) into Eq.(1.7), the Poisson-Boltzmann equation which describe the electric potential in arbitrary space can be derived.

$$\nabla^2 \psi = \frac{d^2 \psi}{dz^2} = -\frac{1}{\varepsilon_0 \varepsilon_r} \sum_i n_i^\infty z_i e \exp\left(-\frac{z_i e \psi(z)}{k_B T}\right) \quad (1.8)$$

The Gouy-Chapman model is analytically obtained by explicitly solving the Poisson-Boltzmann equation under the assumption of a symmetric electrolyte where the valence of a co-ion is equal to the valence of a counter-ion.

$$\tanh\left(\frac{z_i \underline{\psi}(z)}{4}\right) = \tanh\left(\frac{z_i \underline{\psi}_s(z)}{4}\right) \exp(-\kappa z) \quad (1.9)$$

where  $\underline{\psi} = \frac{e\psi}{k_B T}$  is a dimensionless potential parameter and  $\underline{\psi} = 1$  at 25°C and  $\psi = 25.7\text{mV}$ .  $\kappa$  is the Debye-Hückel parameter. Since the Poisson-Boltzmann Eq.(1.8) is a second-order elliptic partial differential equation, Eq. (1.8) can be analytically solved by assuming that the surface potential,  $z_i \underline{\psi}_s$ , is smaller than 25.7mV at 25°C and by employing the relation  $e^{-z} = 1 - z$  for very small  $z$ . In this

case, the Debye-Hückel approximation from the Poisson-Boltzmann equation (1.8) is as follows

$$\nabla^2 \psi = \frac{d^2 \psi}{dz^2} = \kappa^2 \psi(z) \quad (1.10)$$

where the Debye-Hückel parameter is  $\kappa = \left( \frac{e^2 \sum_i n_i^\infty z_i^2}{\epsilon_0 \epsilon_r k_B T} \right)^{\frac{1}{2}}$ .

Based on the two electric potential models explained above, the ion distribution can be determined.

Figure 1.2 shows the volume densities  $n_+$  and  $n_-$  of ions with distance (the dimensionless number  $\kappa z$ ) from the surface in (a) the Gouy-Chapman model and in (b) the Debye-Hückel approximation model, respectively [36].

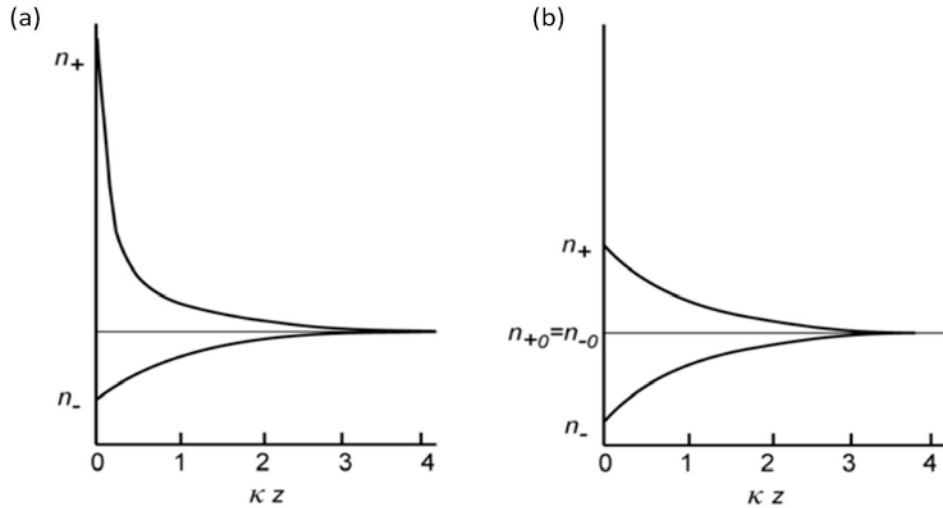


Figure 1.2 Positively and negatively charged ion distribution of (a) the Gouy-Chapman model and (b) the Debye-Hückel approximation model. Reproduced from Hunter, R. et al. [36].

In the case of the Gouy-Chapman model, the positively charged ions rapidly decrease compared to the negatively charged ions. By comparison, the Debye-Hückel approximation model shows that the volume densities  $n_+$  and  $n_-$  of ions is of equal. Currently, the Gouy-Chapman model is mainly applied in considering ion distribution in EDL, as the Debye-Hückel approximation model is not valid for high surface potential [38, 39].

#### **1.2.4 Electrostatic interaction in nanochannels with dimensions below 100nm**

In an electrolyte solution, counter-ions are electrostatically attracted to the negatively charged surface and co-ions are repelled due to the requirement of electro-neutrality within the EDL. The electric potential exponentially decreases across the diffuse layer. The diffuse layer, i.e. the thickness of the EDL, is characterized by the Debye length. For a 1:1 electrolyte, the Debye length is defined as follows,  $\lambda_D = \kappa^{-1}$ ,

$$\lambda_D = \sqrt{\frac{\epsilon_0 \epsilon_r k_B T}{e^2 \sum_i n_i^\infty z_i}} \quad (1.11)$$

which follows the correlation,  $\lambda_D \propto \sqrt{1/n_i^\infty}$ , where  $n_i^\infty$  is the bulk ionic concentration away from the surface. Hence, for monovalent ions in the concentration range of  $10^{-1}$  to  $10^{-5}$  M, the Debye length,  $\lambda_D$ , varies from 1 to 100 nm.

Table 1.1 shows the Debye length which increases with dilution of KCl aqueous solution.

Table 1.1 Debye length  $\lambda_D$  for typical KCl concentrations

KCl concentration (M)	Debye length $\lambda_D$ (nm)
$10^0$	0.3
$10^{-1}$	1.0
$10^{-2}$	3.1
$10^{-3}$	9.6
$10^{-4}$	30.5
$10^{-5}$	96.3

In the case of microchannels, since the Debye length is much smaller than the channel dimensions, it allows for transport of both, co-ions and counter-ions through microchannels regardless of the ionic concentrations as shown in Figure 1.3(b).

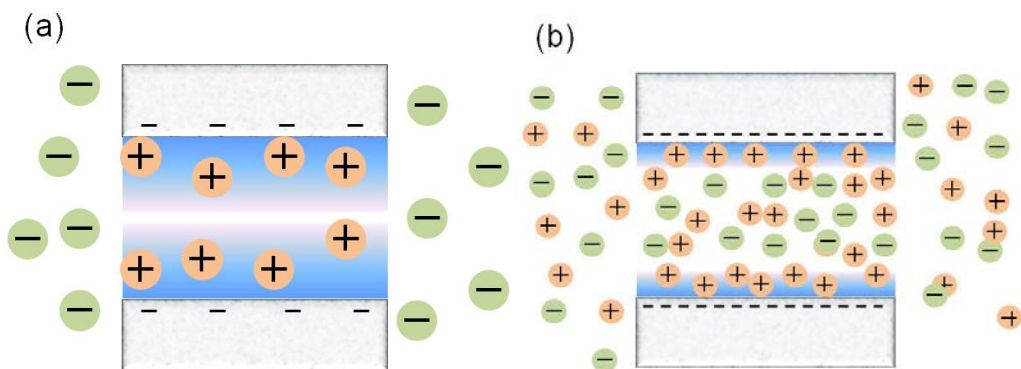


Figure 1.3 Surface charge effects in (a) nanochannels and (b) microchannels.

On the other hand, in the case of nanochannels with at least one dimension comparable to or smaller than the Debye length, counter-ions are accumulated, while co-ions excluded from the channel, yields to counter-ion selective nanochannels as shown in Figure 1.3(a), i.e. unipolar transport phenomenon. Therefore, the direct electrostatic manipulation (such as ion separation [40] and detection [41]) of ions passing through the nanochannels is possible.

### **1.2.5 Electrokinetic phenomena in nanochannels**

Electrokinetic phenomena are a family of several different effects that occur in heterogeneous fluids, or in porous bodies filled with fluid. The term heterogeneous refers to a fluid containing particles, which can be solid, liquid or gas bubbles, with sizes on the micrometer or nanometer scale. In this thesis, a source of electrokinetic phenomena is the double layer of charges, i.e. EDL. The electrokinetic phenomena related to nanofluidic channels typically refer to electroosmosis, electrophoresis and streaming potential/current, which are phenomena due to the interaction of the diffuse layer of EDL and are observed under influence of electric field [36, 42].

#### **1.2.5.1 Electroosmosis**

Electroosmosis is the movement of the liquid adjacent to stationary charged surface, e.g. a capillary or porous plug. If the surface is negatively charged, the net excess of positive ions comprised in EDL, which will draw the liquid together

with them due to viscous interaction, results in a flow towards the cathode as shown in Figure 1.4.

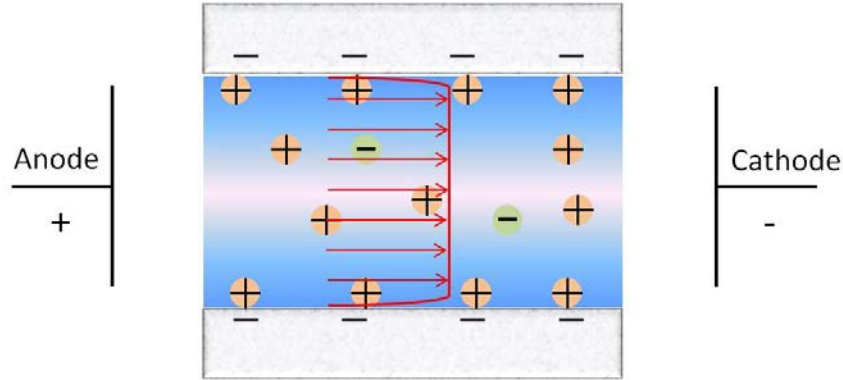


Figure 1.4 Schematic image showing the electroosmotic flow in a negatively charged channel within EDL.

The direction and flow rate of electroosmotic flow is determined by many factors such as the electric field strength, the concentration of electrolytes, the surface charge density on the inner surface of the channel. At the slip plane, the liquid velocity is zero and become a maximum value (plug flow), the so-called electroosmotic velocity  $v_{eo}$ , at some distance from the surface. Electroosmosis was first by Smoluchowski and velocity is defined as follows [43].

$$v_{eo} = \frac{\epsilon_0 \epsilon_r \zeta E}{\eta}, \quad (1.12)$$

where  $\eta$  is the viscosity of fluid and  $E$  is the electric field applied in nanochannel. Since electroosmotic flow velocity does not depend on the size of the channel at high concentration compared to pressure-driven flow, electroosmotic phenomena can be exploited in nanofluidic system. Fluid in nanochannel can be transported by

a pressure difference  $\Delta p$  in the direction across the nanochannel. The pressure drop  $\Delta p$  along the channel from the Hagen-Poiseuille induced by Navier-Stoke equation is calculated as follows [44].

$$\Delta p = \frac{12\eta d Q_p}{wh^3}, \quad (1.13)$$

where  $d$ ,  $w$ ,  $h$  and  $h$  is length, width, and height of channel, respectively and it

is assumed that  $h \ll w$ .  $Q_p = v_f w = \frac{wh^3}{12\eta d} \Delta p$  is the volume flow and  $v_f$  is fluid

velocity. The pressure difference  $\Delta p$  from Eq. (1.13) has  $\Delta p \propto \frac{1}{h^3}$ , requiring

extremely large pressure difference to transport fluid in nanochannel [9].

### 1.2.5.2 Electrophoresis

Electrophoresis is the movement of charged particles adjacent to a stationary charged surface [45]. In an electrokinetic process, electroosmosis and electrophoresis phenomena generally occur simultaneously. In the presence of an electric field, the electric forces acting on the ions drive the ions in opposite direction. In other words, the counter-ions are driven towards the cathode, and the co-ions are driven towards the anode. These migrations of ions result in the transport of fluid (electroosmosis) due to the viscosity of the aqueous solution.

The difference between electroosmosis and electrophoresis can be explained as follows. i) If the channel surface is not charged, there is no electroosmosis, while the electrophoretic effect still exists. ii) Because electroosmosis is the movement

of the fluid (the solution), both, the solute and the solvent are involved in the flow. In contrast, because electrophoresis is the movement of charged particles, the solvent and other neutral particles does not affect the electrophoresis phenomenon. In practice, electrophoresis is also a common method to move ions in nanochannels.

### **1.2.5.3 Streaming potential**

When a liquid is forced to flow through a narrow channel under hydrostatic pressure, the net charge in the mobile part of the EDL is carried and its flow gives rise to a streaming current. Consequently, a potential difference appears[42]. This potential opposes the mechanical transfer of charge by causing backconduction by ion diffusion and electroosmosis. The transfer of charge due to these two effects is called the leak current, and the measuring streaming current relates to an equilibrium condition when the streaming current and the leak current cancel each other. The resultant electrostatic potential difference between the two ends of the narrow channel is referred to as the streaming potential.

## **1.3 Fabrication of Nanofluidic devices**

Transport phenomena in nanoporous systems have extensively been investigated for several decades in the classical disciplines of membrane science and colloid science, yet there was very little understanding about the phenomena occurring in nanopores and thus there were unsolved questions from the geometry

such as pore diameter, length, and non-uniform pore array which are difficult to deduce and manipulate, accurately.

Recent advances in nanofabrication techniques, measurement, and analysis of nanochannels have allowed ion and liquid transport to be routinely examined and controlled in spaces with dimensions that range from 10 to 100 nm. Even if the principle of physical phenomena and forces derived from the classical disciplines is identical to modern nanofluidics using recent nanofabrication techniques, improvements on the fabrication technology, which can exactly control the geometry of the nanofluidic systems, has led to a number of nanofluidic devices available to various experimental conditions, resulting in new phenomena [1].

The modern technology for nanofluidic systems can be generally divided into two main categories: 1) top-down and 2) bottom-up methods[46, 47–51]. In the case of top-down methods, nanostructured materials are derived from a bulk substrate and obtained by progressive removal of a bulk material, until the desired nanostructured material is completed. In contrast, bottom-up methods work in the opposite direction compared to top-down methods. The nanostructured materials are obtained starting from the atomic or molecular precursor and gradually assembling it until the desired nanostructured material is formed. In this chapter, we will briefly review the top-down approach (photolithography and MEMS based nanofabrication) and the bottom-up fabrication techniques using various nanomaterials.

### **1.3.1 Lithography and MEMS based nanofabrication method**

A number of top-down nanofabrication techniques used in nanotechnologies are derived from the fabrication methods used in the semiconductor industry to fabricate the various elements of computer chips (integrated circuits, IC). These methods are collectively called lithography and employ incident light or focused electron beam to selectively remove micro-/ nano- scale structures from a polymer material called resist. Recently, there has been a tremendous advances towards miniaturizing the size of electronic devices and integrating functions into them, which has been possible because of the improvement in lithographic fabrication methods. Nowadays, it is possible to obtain one characteristic length below ~100nm.

Lithographic methods that can fabricate nanostructured materials will be briefly reviewed in this section. Conventional lithography utilizes fabrication technology in which an image is transferred from a mask to a receiving substrate. A typical lithographic process is composed of three main steps as follows.

- i) Coating a substrate such as Si wafer or glass with a sensitive polymer resist
- ii) Exposing the resist to a light, electrons, or ion beams
- iii) Developing the resist image with a suitable chemical (developer) which reveals a positive or negative image on the substrate depending on the type of resist used.

So far, various nanolithography techniques including electron beam lithography (EBL) [52, 53], focused ion beam (FIB) [54, 55], nanoimprint lithography (NIL) [56, 57], interferometric lithography (IL) [58, 59], and sphere lithography (SL) [60 – 63], also named as colloidal lithography, have been developed to fabricate nanostructured materials. In the case of EBL and FIB techniques, they are a proper way to fabricate single or small scale nanochannels. Whereas, other three techniques, NIL, IL, and SL are suitable to create large scale nanopore or nanochannel arrays.

Another promising top-down method is MEMS (microelectromechanical system) based nanofabrication approaches. MEMS is currently one of the most popular nanofabrication method applied to modern nanofluidics thanks to their higher throughput and relatively low-cost compared to photolithography. These MEMS based nanofabrication methods generally involve structure design using standard photolithography and structure formation through a series of deposition or etching processes, resulting in nanostructured materials with depth and/or width in the nanoscale.

To date, several MEMS based nanofabrication methods such as Sacrificial layer releasing (SLR) [64 – 66], etching and bonding [67, 68], etching and deposition [69, 70], edge lithography technique [71], and spacer technique [72], have been developed and employed to create well-defined nanostructured materials. The first two methods mentioned above are more suitable to fabricate 2-D (the number of non-nanoscale dimensions) planar nanochannels with a low

aspect ratio (the ration of channel height to width) and the other three are used to fabricate 2-D vertical nanochannels with a high aspect ratio.

### **1.3.2 Sol-gel synthesis based nanofabrication method**

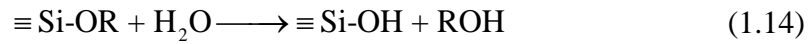
Bottom-up methods can be broadly divided into two categories as follows. In both cases, the nanomaterial are fabricated via a controlled fabrication route that starts from the single atom or molecules.

- i) Gas-phase methods: these include plasma arching and chemical vapor deposition.
- ii) Liquid-phase methods: the most established method is sol-gel synthesis including molecular self-assembly.

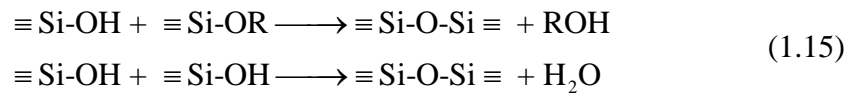
Gas-phase methods are commonly used to produce carbon nanotubes (CNTs) [73 – 76] and liquid-phase methods are employed to make inorganic nanostructured materials such as SiO<sub>2</sub>/Si. In this section, we will shortly review liquid-phase methods (particularly sol-gel synthesis) with regard to fabricating inorganic nanostructured materials which have hydrophilic property.

Sol-gel synthesis is as useful self-assembly method for making nanoparticles as well as nanostructured surfaces such as thin films and three-dimensional nanostructured materials. A typical sol-gel process is composed of three main steps as follows [77, 78].

i) Hydrolysis reaction: the –OR group is replaced with and –OH group.



ii) Condensation/Polymerization: This lead to a growth of particles depending on various conditions such as pH value, temperature, relative humidity, reaction time, and nature of catalyst.



iii) Agglomeration: A network starts to form throughout the liquid medium, resulting in thickening.

Figure 1.5 shows a schematic of different nanostructured materials that can be obtained via a sol-gel process. Dense thin films which have nanostructured silica with controllable pore size, shape, and highly ordered array at nanoscale, suitable for nanofluidic systems by using spray, dip-coating, or spin coat methods (EISA, evaporation-induced self-assembly) and chemical substances or nanomaterials can be fabricated[79 – 81]. The synthesis of nanomaterials using sol-gel process involve the self-assembly of small units such as monomer molecular, resulting in a well-defined shape. Molecules arrange themselves into ordered nanoscale structures by physical or chemical interactions between them.

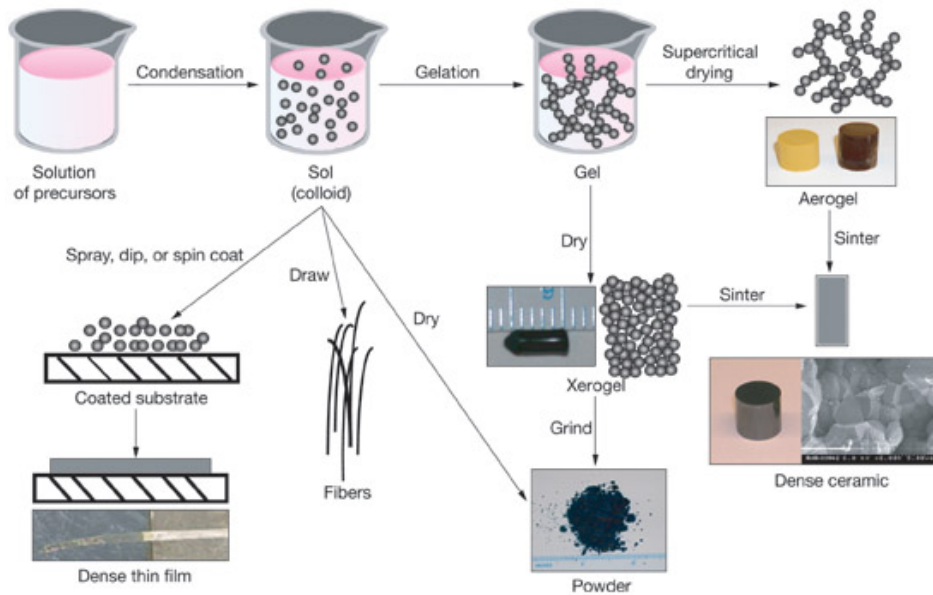


Figure 1.5 Schematic overview of different nanostructured materials that can be obtained via a sol-gel process. Reproduced from Lawrence Livermore National Laboratory image.

### 1.3.3 Mesoporous silica thin films

Recent nanofabrication techniques using inorganic materials enable the control of channel size down to  $\sim 10$  nm and of surface properties of channel walls. A lot of research on ion transport has been in the inorganic nanofluidics device chips fabricated elaborately by nanolithography and MEMS based nanofabrication (top-down approaches). In contrast, although nanomaterial based nanofabrication (bottom-up approaches) employing ion selective polymer, nanoporous materials, and nanoparticle crystal has many advantages such as mass production, high cost-efficient and easy-to-fabricate, few studies have been carried out to investigate ion transport phenomena in nanofluidic systems [82]. Furthermore, the conventional

lithographic fabrication technique has intrinsic difficulties in manufacturing nanofluidic devices with  $< 10\text{nm}$  in diameter and high pore density in large-scale [83, 84].

These issues can be solved by using nanomaterials. Among nanostructured materials made by the nanomaterial based nanofabrication, micelle-templated mesoporous silica materials, which is synthesized by the self-assembly of surfactant molecules used as the structure-directing agent have particularly attracted considerable interest in a variety of practical fields such as adsorbent, catalysts, PEM of fuel cell, and separation due to large porosity, highly ordered structures, uniform pore size in the range of 2 to 50nm, and high surface area to volume ratio [85 – 89].

According to the IUPAC definition[90], depending on the pore size, nanoporous materials fall into three categories: i) microporous materials with pore diameters less than 2 nm, ii) mesoporous materials that have a pore diameter ranging from 2 to 50 nm, and iii) macroporous materials that have pore diameters larger than 50nm. Microporous and mesoporous materials are generally referred to as nanoporous materials. It was the development of mesoporous silica with highly ordered pore arrangement and tunable pore size in the range 2-50 nm that allowed applications such as sensing and electronics.

The mesoporous silica was first reported by Mobil Research and Development on surfactant-templated materials and it was designated as MCM-41 [83, 84]. They reported that the synthesis of mesoporous materials form the calcinations of

aluminosilicate gels in the presence of surfactants. The synthesized mesoporous material showed regular arrays of uniform channels with the dimension in the range of 1.6~10 nm, which can be tailored by determining the kind of surfactant and the sol-gel conditions. The TEM image shown in Figure 1.6 shows a regular, hexagonal array of uniform channels for various MCM-41 materials with pore sizes from 20 to 100 Å.

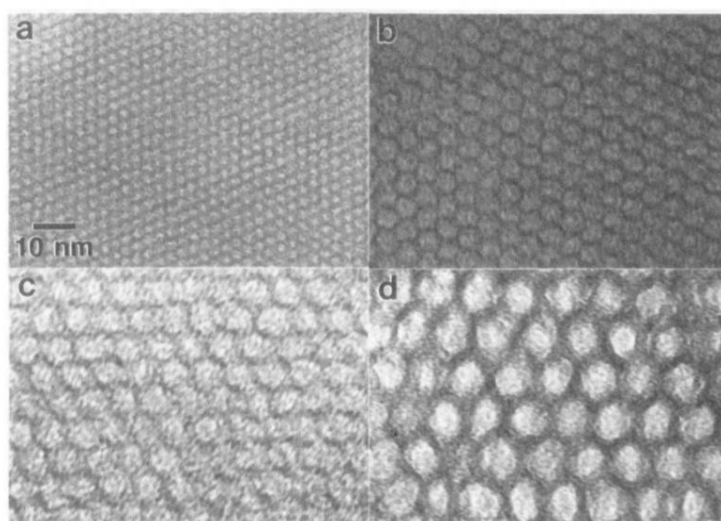


Figure 1.6 TEM image of several MCM-41 materials having pore sizes of (a) 20, (b) 40, (c) 65, and (d) 100 Å. Reproduced from Beck, J. et al. [84]

Mesoporous materials present a unique opportunity to create a new paradigm of materials that may be used as films for thin-layer chromatography, separation membrane, micron scale elements for lab-on-a-chip analysis system due to the controlled tunability of porous properties at the mesoscale, and well-defined structure (textures and morphologies) [91]. In particular, the synthesis of mesoporous materials in the form of homogeneous thin films was a very

important achievement because it allowed the development of materials for use in optoelectronic devices, membrane-based separations, nanofluidic systems, sensors/actuator arrays, and for the fabrication of nanowires [91 – 96].

#### **1.3.4 Synthesis method of mesoporous silica thin films**

Mesoporous silica thin films are generally synthesized through evaporation process (EISA, Evaporation-Induced Self-Assembly) of solutions containing an inorganic precursor, tetraethoxysilane (TEOS), an organic supermolecular template (ionic, nonionic or polymeric surfactants), and some acidic additives to control pH condition to avoid extended condensation of the inorganic precursor dissolved in a volatile solvent such as EtOH. The EISA process is based on the processes that occur during the formation of mesostructured silica thin films. Self-assembly organizes supramolecules into well-define assemblies [75, 76].

Surfactants used commonly to synthesize mesoporous silica materials are amphiphilic molecules or tri-blockcopolymer composed of hydrophobic and hydrophilic components. It is well-known that amphiphilic molecules in water can form various supramolecular aggregates (micelle structure) such as spherical, cylindrical, and lamellar aggregates. These supramolecular aggregates are arranged in highly ordered structures with different symmetries such as cubic, hexagonal, and lamellar [97]. Some typical micelle structures are presented in Figure 1.7. Their symmetries and morphologies strongly depend on solution conditions such as pH value, surfactant concentration, or temperature.

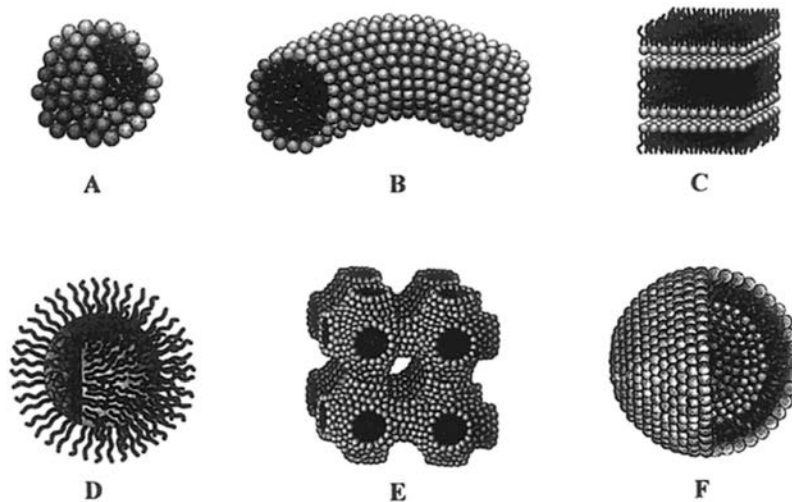


Figure 1.7 Micelle structures A. sphere, B. cylinder, C. planar bilayer, D. reverse micelles, E. bicontinuous phase, F. liposomes. Reproduced from Soler-Illia, G. et al. [93]

Figure 1.8 shows a schematic phase diagram for cationic surfactant in water. At very low concentration, the surfactant is present as free molecules dissolved in solution and adsorbed at interfaces. At slightly higher concentrations, called the critical micelle concentration (CMC<sub>1</sub>), the individual surfactant molecules start to form spherical aggregates (micelles). At higher concentration more than CMC<sub>2</sub>, spherical micelles coalesce to form elongated cylindrical micelles, cubic, or lamellar structures [98]. There are various deposition techniques such as dip- or spin-coating to make thin films from a sol-gel process [99–101]. In general, mesoporous silica thin films are fabricated using the dip-coating method because of the increased ability to align the pores parallel to the substrate in the desired direction as compared to spin-coating [102], and thus in this work, the dip-coating deposition method was used. Using the dip-coating process, a well-ordered

mesostructured thin film can be deposited onto the substrate by evaporation-induced self-assembly [103 – 105].

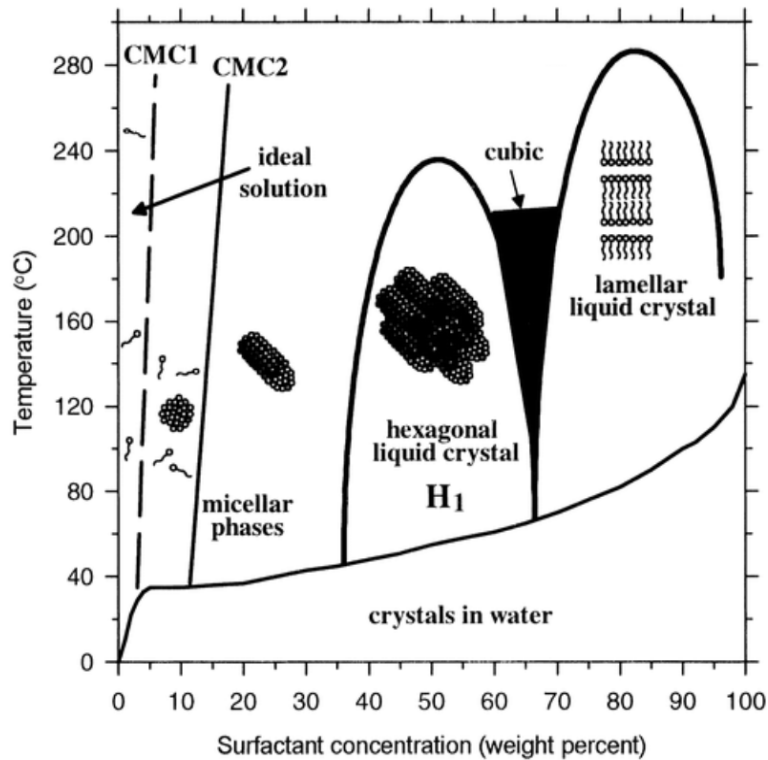


Figure 1.8 Schematic phase diagram for  $C_{16}TMABr$  in water. CMC is exaggerated to higher concentration. Reproduced from Raman, N. et al. [94]

In the dip-coating process shown in Figure 1.9, a substrate is vertically immersed into the precursor solution and withdrawn at a constant speed. Due to the solution-substrate wettability, a very thin liquid layer is formed on the substrate. At this time, the thin film thickness depends on the withdrawn speed and the viscosity of the precursor solution. After the substrate is dragged from the solution, the wet liquid thin film rapidly begins to evaporate, causing an increase of the surfactant concentration and thereby triggering micelle formation around

dynamic meniscus region. Furthermore, the micelles start to interact with the silica inorganic precursor, and finally form a well-ordered nanostructured thin film on the substrate.

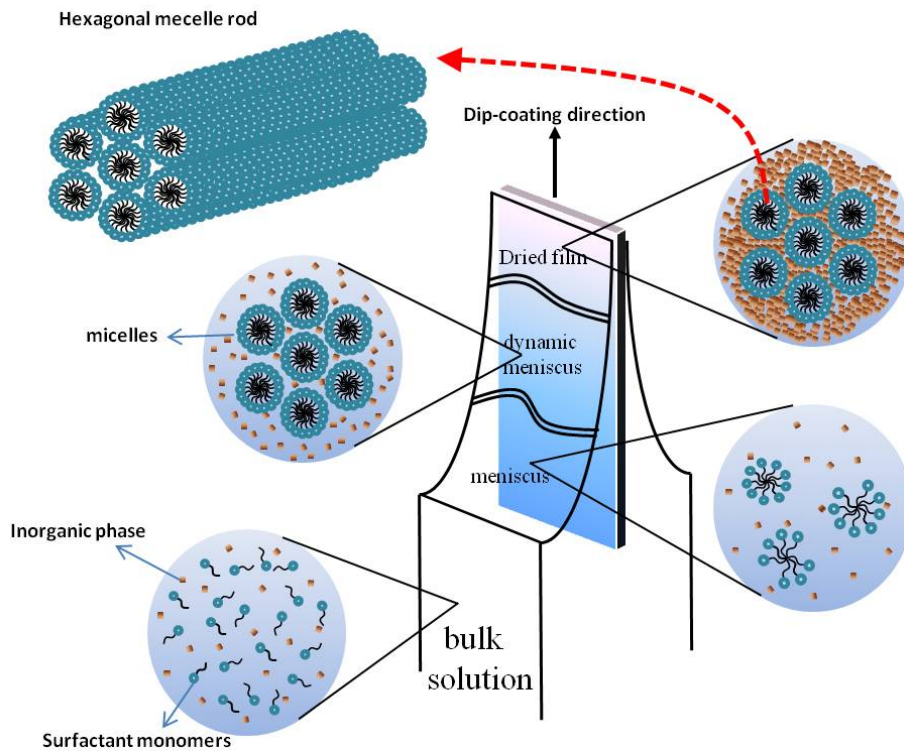


Figure 1.9 Dip-coating process to synthesize the a well-ordered mesostructured silica thin film.

## 1.4 Objective of the thesis

Transport of ions and molecules through nanoscale geometries has attracted broad interests in various fields. In the case of nanochannels/nanopores comparable to Debye length,  $\lambda_D$ , new transport phenomena such as ion-perm

selective nanochannels (unipolar transport) occur due to the electrostatic interaction. Such new phenomenon opens up the possibility of using electric field to control the flow of charged ion or the fluid in nanochannels.

Nanochannels having dimensions comparable to the size of biomolecules such as proteins and DNAs have started to be exploited in biotechnology because a lot of separation [106, 107] and sensing processes [108–111] requires pores with nanometer scale. For instance,  $\alpha$ -hemolysin, one type of biological nanopores, has been employed to provide materials for experimental due to single molecule sensitivity [112]. However, the drawback of biological materials with nanopores is that it is very unstable and difficult to control.

In contrast, artificial inorganic nanochannels, fabricated by lithography/MEMS based method on solid substrate such as  $\text{SiO}_2/\text{Si}$ , are robust and of more flexibility and precise control in terms of nanostructured material geometries. For that reason, many studies have been reported on nanofluidic system fabricated by conventional photolithography, top-down approach. However, these nanofabrication methods have also intrinsic limitations in making sub-10 nm, a large scale system, complex nanostructured materials such as three-dimensional cubic structures, and low cost efficient. For that reason, few studies have been conducted on nanofluidic system with nanochannels less than ~10 nm.

Chemical synthesis techniques as an alternative to solve these difficulties provide a practical solution using self-assembled soft templates to create nanoporous inorganic materials. Among these things, mesoporous silica with

uniform pore sizes from 2 nm to 50 nm and regular pore array can be excellent alternative of nanofluidic system to investigate ion or molecular transport phenomena.

In this thesis, ion transport arising from electrokinetic phenomena at the interface between liquid and solid was investigated to propose a new possibility of mesoporous silica materials as nanofluidic system with nanochannels less than ~10 nm. Furthermore, ion transport in complex geometry which hasn't been reported was studied with the aim of exploring new science and developing novel applications for modern nanofluidics. In this thesis we want:

1) To study the ion or proton transport phenomena in mesoporous silica. Mesoporous silica SBA-16 thin films with highly ordered three-dimensional cubic structures (ink-bottle-like geometry) were synthesized on a Si substrate via the dip-coating method. After these films were filled with KCl or HCl aqueous solutions, the ionic or proton current passing through the mesopores was experimentally measured by applying electrochemical measurement under DC electric fields.

2) To quantitatively discuss ion transport behavior of mesoporous silica SBA-16 thin films. The ionic current in the steady state was analyzed by means of continuum dynamics. If the length scale is larger than ~5 nm, it is well known that continuum dynamics provides an adequate description of transport phenomena. In the case of SBA-16, since the narrowest length scale is approximately 2nm,

stochastic or molecular dynamics simulation generally can provide a practical method for the description of ion channel conductance. However, in this study, we found that the modified Poisson-Nernst-Planck equation was the governing equation and was suitable to quantitatively model the system.

3) Because SBA-16 has limitations such as complex three-dimensional geometry and too small sized nanopores close to  $\sim 2$  nm in diameter, it is somewhat difficult to apply commonly general conditions. Therefore, two-dimensional hexagonal mesoporous silica SBA-15 thin film with dimensions ranging of 5-10 nm and more simple geometry was synthesized to investigate ion or water transport phenomena of aqueous solution confined in mesopores. The effect of the withdrawal speed on the thickness of the films, one-dimensional pore alignments and two-dimensional hexagonal pore arrays was very detail elucidated to make nanofluidic device suitable for ion transport study.

4) Mesoporous silica SBA-16 thin film has a relatively complex geometry compared to previously studied nanofluidic system. It needs to investigate on simple geometry with two-dimensional structure (mesoporous silica SBA-15) to generalize ion transport arising in nanofluidic system with nanochannels less than  $\sim 10$  nm. To utilize synthesized SBA-15 thin films as nanofluidic system, hybrid top-down (photolithography) and bottom-up (sol-gel synthesis based on Evaporation-Induced Self-Assembly) fabrication method was employed. To compare with ion transport behavior of mesoporous silica SBA-16 thin films, the

ion current was experimentally measured using the fabricated nanofluidic device with SBA-15 thin films under DC electric fields.

The nanofluidic devices using mesoporous silica materials described here can easily be integrated into other nanofluidic system and may be applied in the development of nanopores, such as artificial ion channels and polymer electrolyte membranes with complex structures, for smooth proton transport. Furthermore, exploring fundamental characteristics of transport phenomena on well-ordered nanoporous materials with 1 nm order structures makes it possible to achieve better understanding and improving membrane nanofiltration, adsorbents, electrochemical cells such as fuel cells for energy generation, sensors, and desalination technologies.

The rest of the thesis is organized as follows. Chapter 2 presents the experimental observation and numerical description to analyze ion transport phenomena occurring in mesoporous silica SBA-16 thin film. Chapter 3 describes the proton transport in comparison with ion transport in SBA-16. Chapter 4 presents the effect of withdrawal speed on film thickness and hexagonal pore-array dimensions of SBA-15 mesoporous silica thin film by using SEM, TEM, XRR, XRD analysis techniques. In Chapter 5, development of nanofluidic devices using mesoporous silica SBA-15 thin films and future work are discussed. Finally, conclusions are described in chapter 5.

## 1.5 Reference

1. Eijkiel, J.; Van Den Berg, A. Nanofluidics: What is it and what can we expect from it? *Microfluid Nanofluid* **2005**, *1*, 249-267.
2. Sparreboom, W.; Van Den Berg, A.; Eijikel, J. Principles and application of nanofluidic transport. *Nat. Nanotechnol.* **2009**, *4* (11), 713-720.
3. Bocquet, L.; Charlaix, E. Nanofluidics, from bulk to interfaces. *Chem. Soc. Rev.* **2010**, *39*, 1073-1095.
4. Kovarik, M.; Jacobson, S. Nanofluidics in Lab-on-a-Chip Devices. *Anal. Chem.* **2009**, *81*, 7133-7140.
5. Israelachvili, J. Intermolecular and Surface Forces. Academic Press, London, 1992.
6. Hille, B. *Ion Channels of Excitable Membranes*, 3rd ed.; Sinauer Associates Inc.: Sunderland. MA, 2001.
7. Tas, N. R.; Mela, P.; Berenschot, J. W.; Berg, A. v. d. Capillarity induced negative pressure of water plugs in nanochannels. *Nano Lett.* **2003**, *3* (11), 1537-1540.
8. Tas, N.; Escalante, M.; Honschoten, J. V.; Jansen, H.; Elwenspoek, M. Capillary negative pressure measured by nanochannel collapse. *Langmuir* **2010**, *26* (3), 1473-1476.
9. Tegenfeldt, J.; Prinz, C.; Cao, H.; Huang, R.; Austin, R.; Chou, S.; Cox, E.; Sturm, J. Micro- and nanofluidics for DNA analysis. *Anal. Bioanal. Chem.* **2004**, *378*, 1678-1692.
10. Healy, K.; Schiedt, B.; Morrison, A. Solid-state nanopore technologies for nanopore-base DNA analysis. *Nanomedicine* **2007**, *2* (6), 875-897.
11. Stein, D.; Kruithof, M.; Dekker, C. Surface-charge-governed ion transport in nanofluidic channels. *Phys. Rev. Lett.* **2004**, *93* (3), 035901.
12. Chang, H.; Kosari, F.; Andreadakis, G.; Alam, M.; Vasmataziz, G.; Bashir, R. DNA-Mediated Fluctuations in Ionic Current through Silicon Oxide Nanopore Channels. *Nano Lett.* **2004**, *4*, 1551-1556.
13. Goldberger, J.; Fan, R.; Yang, P. Inorganic Nanotubes: A Novel Platform for Nanofluidics. *Acc. Chem. Res.* **2006**, *39*, 239-248.
14. Vlassioux, I.; Smirnov, S.; Siwy, Z. Ionic Selectivity of Single Nanochannels. *Nano Lett.* **2008**, *8*, 1978-1985.
15. Daiguji, H.; Yang, P.; Szeri, A.; Majumdar, A. Electrochemomechanical Energy Conversion in Nanofluidic Channels. *Nano Lett.* **2004**, *4* (12), 2315-2321.
16. Van Der Heyden, F.; Bonthuis, D.; Stein, D.; Meyer, C.; Dekker, C. Electrokinetic Energy Conversion Efficiency in Nanofluidic Channels. *Nano Lett.* **2006**, *6*, 2232-2237.

17. Van Der Hyden, F.; Stein, D.; Besteman, K.; Dekker, C. Charge Inversion at High Ionic Strength Studied by Streaming Current. *Phys. Rev. Lett.* **2006**, *96*, 224502.
18. Daiguji, H. Ion transport in nanofluidic channels. *Chem. Soc. Rev.* **2010**, *39*, 901-911.
19. Schoch, R.; Han, J.; Renaud, P. Transport phenomena in nanofluidics. *Rev. Mod. Phys.* **2008**, *80*, 839-883.
20. Pu, Q.; Yun, J.; Temkin, H.; Liu, S. Ion-Enrichment and Ion-Depletion Effect of Nanochannel Structures. *Nano Lett.* **2004**, *4* (6), 1099-1103.
21. Karnik, R.; Fan, R.; Yue, M.; Li, D.; Yang, P.; Majumdar, A. Electrostatic Control of Ion and Molecules in Nanofluidic Transistors. *Nano Lett.* **2005**, *5* (5), 943-948.
22. Karnik, R.; Duan, C.; Castelino, K.; Daiguji, H.; Majumdar, A. Rectification of Ionic Current in a Nanofluidic Diode. *Nano Lett.* **2007**, *7* (3), 547-551.
23. Goldberger, J.; Fan, R.; Yang, P. Inorganic Nanotubes: A Novel Platform for nanofluidics. *Acc. Chem. Res.* **2006**, *39* (4), 239-248.
24. Sonnefeld, J.; Gobel, A.; Vogelsberger, W. Surface-Charge density on Spherical Silica Particles in Aqueous Alkali Chloride Solutions. 1. Experimental Results. *Colloid and Polymer Science* **1995**, *273*, 926-931.
25. Sonnefeld, J. Surface-Charge Density on Spherical Silica Particles in Aqueous Alkali Chloride Solutions. 2. Evaluation of the Surface-Charge Density Constants. *Colloid and Polymer Science* **1995**, *273*, 932-938.
26. Hunter, R.; Wright, H. Dependence of Electrokinetic Potential on Concentration of Electrolyte. *Journal of Colloid and Interface Science* **1971**, *37*, 564-580.
27. Sabia, R.; Ukrainczyk, L. Surface Chemistry of SiO<sub>2</sub> and TiO<sub>2</sub>-SiO<sub>2</sub> glasses as determined by titration of soot particles. *Journal of Non-Crystalline Solids* **2000**, *277*, 1-9.
28. Perram, J.; Hunter, R.; Wright, H. Charge and Potential at Oxide-Solution Interface. *Chemical Physics Letters* **1973**, *23*, 265-269.
29. Davis, J.; James, R.; Leckie, J. Surface Ionization and Complexation at Oxide-Water Interface. 1. Computation of Electrical Double-Layer Properties in Simple Electrolytes. *Journal of Colloid and Interface Science* **1978**, *63*, 480-499.
30. Yates, D.; Levine, S.; Healy, T. Site-Binding Model of Electrical Double-Layer at Oxide-Water Interface. *Journal of the Chemical Society-Faraday Transactions I* **1974**, *70*, 1807-1818.
31. Kosmulski, M. The Surface Charging at Low Density of Protonatable Surface Sites. *Langmuir* **2005**, *21*, 7421-7426.
32. Iler, R. K. *The Chemistry of Silica*; Wiley: New York, 1979.
33. Behrens, S.; Grier, D. The charge of glass and silica surfaces. *Journal of Chemical Physics* **2001**, *115*, 6716-6721.

34. Kovacs, G. "Introduction to the theory, design and modeling of thin-film microelectrodes for neural interfaces" in *Enabling technologies for cultured neural networks*; Academic Press, Inc.: San Diego, USA, 1994.
35. Overbeek, J. "Electrokinetic Phenomena," in *Colloid Science*; Elsevier: Amsterdam, 1952; Vol. 1.
36. Hunter, R. *Zeta Potential in Colloid Science*; Academic Press, Inc.: London, UK, 1981.
37. Schoch, R.; Han, J.; Renaud, P. Transport phenomena in nanofluidics. *Rev. Mod. Phys.* **2008**, *80* (3), 839-883.
38. Conlisk, A. The Debye-Hückel approximation: Its use in describing electroosmotic flow in micro- and nanochannels. *Electrophoresis* **2005**, *26*, 1896-1912.
39. Conlisk, A.; McFerran, J.; Zheng, Z.; Hansford, D. Mass Transfer and Flow in Electrically Charged Micro- and Nanochannels. *Analytical Chemistry* **2002**, *74*, 2139-2150.
40. Nishizawa, M.; V. Menon, C. M. Metal Nanotube Membranes with Electrochemically Switchable Ion-Transport Selectivity. *Science* **1995**, *268*, 700-702.
41. Kobayashi, Y.; Martin, C. Highly Sensitive Methods for Electroanalytical Chemistry Based on Nanotubule Membranes. *Anal. Chem.* **1999**, *71*, 3665-3672.
42. Shaw, D. *Introduction to Colloid and Surface Chemistry*, 4th ed.; Elsevier Science Ltd., 1992.
43. Smoluchowski, M. Versuch einer mathematischen Theorie der Koagulationskinetik kolloider Lösungen. *Zeitschrift für physikalische Chemie* **1917**, *92*, 129-168.
44. Sze, A.; Erickson, D.; Ren, L.; Li, D. Zeta-potential measurement using the Smoluchowski equation and the slope of the current-time relationship in electroosmotic flow. *Journal of Colloid and Interface Science* **2003**, *261*, 402-410.
45. Morgan, H.; Green, N. G. *AC Electrokinetics: colloids and nanoparticles*; Research Studies Press Ltd.: Hertfordshire, UK, 2003.
46. Mijatovic, D.; Eijkel, J.; Berg, A. v. d. Technologies for nanofluidic systems: top-down vs. bottom-up - a review. *Lap Chip* **2005**, *5*, 492-500.
47. Abgrall, P.; Nguyen, N. Nanofluidic devices and their applications. *Anal. Chem* **2008**, *80* (7), 2326-2341.
48. Xia, D.; Yan, J.; Hou, S. Fabrication of nanofluidic biochips with nanochannels for application in DNA analysis. *Small* **2012**, *8* (18), 2787-2801.
49. Perry, J.; Kandlikar, S. Review of fabrication of nanochannels for single phase liquid flow. *Microfluid. Nanofluid.* **2005**, *2* (3), 185-193.
50. Dekker, C. Solid-state nanopores. *Nat. Nanotechnol.* **2007**, *2* (4), 209-215.
51. Prakash, S.; Piruska, A.; Gatimu, E.; Bohn, P.; Sweedler, J.; Shannon, M.

- Nanofluidic: Systems and applications. *IEEE Sens. J.* **2008**, *8* (5), 441-450.
52. Perry, J.; Zhou, K.; Harms, Z.; Jacobson, S. Ion transport in nanofluidic funnels. *ACS Nano* **2010**, *4* (7), 3897-3902.
  53. Kim, S.; Cui, Y.; Lee, M.; Nam, S.; Oh, D.; Kang, S.; Kim, Y.; Park, S. Simple fabrication of hydrophilic nanochannels using the chemical bonding between activated ultrathin PDMS layer and cover glass by oxygen plasma. *Lab Chip* **2011**, *11* (2), 348-353.
  54. Tseng, A. Recent development in nanofabrication using focused ion beams. *Small* **2005**, *1* (10), 924-939.
  55. Tseng, A. Recent developmetns in micromilling using focused ion beam technology. *J. Micromech. Microeng.* **2004**, *14* (4), 15-34.
  56. Guo, L. Nanoimprint lithography: Methods and material requirement. *Adv. Mater.* **2007**, *19* (4), 495-513.
  57. Cho, Y.; Park, J.; Park, H.; Cheng, X.; Kim, B.; Han, A. Fabrication of high-aspect-ratio polymer nanochannels using a novel Si nanoimprint modl and solvent-assisted sealing. *Microfluid. Nanofluid.* **2009**, *9* (2-3), 163-170.
  58. Xia, D.; Ku, Z.; Lee, S.; Brueck, S. Nanostructures and functional materials fabricated by interferometric lithography. *Adv. Mater.* **2011**, *23* (2), 147-179.
  59. O'Brien, M.; Bisong, P.; Ista, L.; Rabinovich, E.; Garcia, A.; Sibbett, S.; Lopez, G.; Brueck, S. Fabrication of an integrated nanofluidic chip using interferometric lithography. *J. Vac. Sci. Technol. B* **2003**, *21* (6), 2941-2945.
  60. Zhang, G.; Wang, D. Colloidal lithography-The art of nanochemical patterning. *Chem. Asian J.* **2009**, *4* (2), 236-245.
  61. Li, Y.; Cai, W.; Duan, G. Ordered micro/nanostructured arrays based on the monolayer colloidal crystals. *Chem. Mater.* **2008**, *20* (3), 615-624.
  62. Vogel, N.; Weiss, C.; Landfester, K. From soft to hard: The generation of functional and complex colloidal monolayers for nanolithography. *Soft Matter* **2012**, *8* (5), 4044-4061.
  63. Whitney, A.; Myers, B.; Duyne, R. V. Sub-100 nm triangular nanopores fabricated with the reactive ion etching variant of nanosphere lithography and angle-resolved nanosphere lithography. *Nano Lett.* **2004**, *4* (8), 1507-1511.
  64. Sordan, R.; Miranda, A.; Traversi, F.; Colombo, D.; Chrastina, D.; Isella, G.; Masserini, M.; Miglio, L.; Kern, K.; Balasubramanian, K. Vertical arrays of nanofluidic channels fabricated without nanolithography. *Lab Chip* **2009**, *9* (11), 1556-1560.
  65. M. Stern, M. G.; Curtin, J. Nanochannel fabrication for chemical sensors. *J. Vac. Sci. Technol. B* **1997**, *15* (6), 2887-2891.
  66. Barton, R.; Ilic, B.; Verbrige, S.; Cipriany, B.; Parpia, J.; Craighead, H. Fabrication

- of a nanomechanical mass sensor containing a nanofluidic channel. *Nano Lett.* **2010**, *10* (6), 2058-2063.
67. Haneveld, J.; Jansen, H.; Berenschot, E.; Tas, N.; Elwenspoek, M. Wet anisotropic etching for fluidic 1D nanochannels. *J. Micromech. Microeng* **2003**, *13* (4), 62-66.
  68. Abgrall, P.; Low, L.; Nguyen, N. Fabrication of Planar nanofluidic channels in a thermoplastic by hot-embossing and thermal bonding. *Lab Chip* **2007**, *7* (4), 520-522.
  69. Ilic, B.; Czaplewski, D.; Zalalutdinov, M.; Schmidt, B.; Craighead, H. Fabrication of flexible polymer tubes for micro and nanofluidic applications. *J. Vac. Sci. Technol. B* **2002**, *20* (6), 2459-2465.
  70. Mao, P.; Han, J. Massively-parallel ultra-high-aspect-ratio nanochannels as mesoporous membranes. *Lab Chip* **2009**, *9* (4), 586-591.
  71. Love, J.; Paul, K.; Whitesides, G. Fabrication of nanometer-scale features by controlled isotropic wet chemical etching. *Adv. Mater.* **2001**, *13* (8), 604-607.
  72. Smith, R.; Goldman, K.; Fissell, W.; Fleischman, A.; Zorman, C.; Roy, S. Removal of endotoxin from deionized water using micromachined silicon nanopore membranes. *J. Micromech. Microeng.* **2011**, *21* (5), 054029.
  73. Huang, Z.; Xu, J.; Ren, Z.; Wang, J.; Siegal, M.; Provencio, P. Growth of highly oriented carbon nanotubes by plasma-enhanced hot filament chemical vapor deposition. *Applied Physics Letters* **1998**, *73* (23), 3845-3847.
  74. Ren, Z.; Huang, Z.; Xu, J.; Wang, J.; Bush, P.; Siegal, M.; Provencio, P. Synthesis of Large Arrays of Well-Aligned Carbon Nanotubes on Glass. *Science* **1998**, *282* (5391), 1105-1107.
  75. Chhowalla, M.; Teo, K.; Ducati, C.; Rupesinghe, N.; Amaratunga, G.; Ferrari, A.; Roy, D.; Robertson, J.; Milne, W. Growth process conditions of vertically aligned carbon nanotubes using plasma enhanced chemical vapor deposition. *Journal of Applied Physics* **2001**, *90* (10), 5308-5317.
  76. Bower, C.; Zhu, W.; Jin, S.; Zhou, O. Plasma-induced alignment of carbon nanotubes. *Applied Physics Letters* **2000**, *77* (6), 830-832.
  77. Hench, L.; West, J. The sol-gel process. *Chem. Rev.* **1990**, *90* (1), 33-72.
  78. Brinker, C.; Scherer, G. *SOL-GEL SCIENCE: The Physics and Chemistry of Sol-Gel Processing*; Academic press, Inc.: San Diego, 1990.
  79. Brinker, C.; Lu, Y.; Sellinger, A.; Fan, H. Evaporation-Induced Self-Assembly: Nanostructures Made Easy. *Adv. Mater.* **1999**, *11* (7), 579-585.
  80. Grosso, D.; Cagnol, F.; Soler-Illia, G.; Crepaldi, E.; Amenitsch, H.; Brunet-Bruneau, A.; Bourgeois, A.; Sanchez, C. Fundamentals of Mesostructuring Through Evaporation-Induced Self-Assembly. *Advanced Functional Materials* **2004**, *14* (4), 309-322.

81. Lu, Y.; Fan, H.; Doke, N.; Loy, D.; Assink, R.; LaVan, D.; Brinker, C. Evaporation-Induced Self-Assembly of Hybrid Bridged Silsesquioxane film and Particulate Mesophase with Integral Organic Functionality. *J. Am. Chem. Soc.* **2000**, *122* (22), 5258-5261.
82. Shin, S.; Kim, B.; Song, J.; Lee, H.; Cho, H. A facile route for the fabrication of large-scale gate-all-around nanofluidic field-effect transistors with low leakage current. *Lab Chip* **2012**, *12*, 2568-2574.
83. Mao, P.; Han, J. Fabrication and Characterization of 20nm Planar Nanofluidic Channels by Glass-Glass and Glass-Silicon Bonding. *Lab Chip* **2005**, *5*, 837-844.
84. Cao, H.; Yu, Z.; Wang, J.; Tegenfeldt, J.; Austin, R.; Chen, E.; Wu, W.; Chuo, S. Fabrication of 10nm Enclosed Nanofluidic channels. *Appl. Phys. Lett.* **2002**, *81* (1), 174-176.
85. Yang, P.; Zhao, D.; Margolese, D.; Chmelka, B.; Stucky, G. Generalized Syntheses of Large-Pore Mesoporous Metal Oxides with Semicrystalline Frameworks. *Nature* **1998**, *396*, 152-155.
86. Miyata, H.; Suzuki, T.; Fukuoka, A.; Sawada, T.; Watanabe, M.; Noma, T.; Takada, K.; Mukaide, T.; Kuroda, K. Silica Films with a Single-Crystalline Mesoporous Structure. *Nat. Mater.* **2004**, *3*, 651-656.
87. Kresge, C.; Leonowicz, M.; Roth, W.; Vartuli, J.; Beck, J. Ordered Mesoporous Molecular Sieves Synthesized by a Liquid-Crystal Template Mechanism. *Nature* **1992**, *359*, 710-712.
88. Beck, J.; Vartuli, J.; Roth, J.; Leonowicz, M.; Kresge, C.; Schmit, K.; Chu, C.; Sheppard, E.; McCullen, S.; Higgins, J.; Schlenker, J. A New Family of Mesoporous Molecular Sieves Prepared with Liquid Crystal Templates. *J. Am. Chem. Soc.* **1992**, *114*, 10834-10843.
89. Ariga, K.; Vinu, A.; Yamaguchi, Y.; Ji, Q.; Hill, J. Nanoarchitectonics for Mesoporous Materials. *Bull. Chem. Soc. Jpn.* **2012**, *85*, 1-32.
90. Rouquerol, J.; Avnir, D.; Fairbridge, C.; Everett, D.; Haynes, J.; Pericone, N.; Ramsay, J.; Sing, K.; Unger, K. Recommendation for the characterization of porous solids. *Pure Appl. Chem.* **1994**, *66* (8), 1739-1758.
91. Craighead, H. Future lab-on-a-chip technologies for interrogating individual molecules. *Nature* **2006**, *442*, 387-393.
92. Fan, R.; Huh, S.; Yan, R.; Arnold, J.; Yang, P. Gated Proton Transport in Aligned Mesoporous Silica Films. *Nat. Mater.* **2008**, *7*, 303-307.
93. Bearzotti, A.; Bertolo, J.; Innocenzi, P.; Falcaro, P.; Traversa, E. Humidity Sensors Based on Mesoporous Silica Thin Films Synthesized by Block Copolymers. *J. Eur. Ceram. Soc.* **2004**, *24*, 1969-1972.
94. Sakai, H.; Baba, R.; Hashimoto, K.; Fujishima, A.; Heller, A. Local Detection of Photoelectrochemically Produced H<sub>2</sub>O<sub>2</sub> with a "Wired" Horseradish Peroxidase

- Microsensor. *J. Phys. Chem.* **1996**, *99*, 11896-11900.
95. Tamagawa, C.; Schiller, P.; Polla, D. Pyroelectric PbTiO<sub>3</sub> Thin Films for Microsensor Applications. *Sens. Actuators, A* **1992**, *35*, 77-83.
  96. Li, W.; Xie, S.; Qian, L.; Chang, B.; Zou, B.; Zhou, W.; Zhao, R.; Wang, G. Large-Scale Synthesis of Aligned Carbon Nanotubes. *Science* **1996**, *274*, 1701-1703.
  97. Soler-Illia, G.; Sanchez, C.; Lebeau, B.; Patarin, J. Chemical Strategies To Design Textured Materials: from Microporous and Mesoporous Oxides to Nanonetworks and Hierarchical Structures. *Chem. Rev.* **2002**, *102*, 4093-4138.
  98. Raman, N.; Anderson, M.; Brinker, C. Template-Based Approaches to the preparation of Amorphous Nanoporous silicas. *Chem. Mater.* **1996**, *8*, 1682-1701.
  99. Lu, Y.; Ganguli, R.; Drewien, C. A.; Anderson, M. T.; Brinker, C. J.; Gong, W.; Guo, Y.; Soyez, H.; Dunn, B.; Huang, M. H.; Zink, J. I. Continuous Formation of Supported Cubic and Hexagonal Mesoporous Films by Sol-Gel Dip-Coating. *Nature* **1997**, *389*, 364-368.
  100. Ogawa, M. Formation of Novel Oriented Transparent Films of Layered Silica-Surfactant Nanocomposites. *J. Am. Chem. Soc.* **1994**, *116*, 7941-7942.
  101. Ogawa, M. A Simple Sol-Gel Route for the Preparation of Silica-Surfactant Mesostructured Materials. *Chem. Commun.* **1996**, 1149-1150.
  102. Wu, C.; Yamaguchi, Y.; Ohsuna, T.; Kuroda, K. Structural Study of Highly Ordered Mesoporous Silica Thin Films and Replicated Pt Nanowires by High-Resolution Scanning Electron Microscopy (HRSEM). *J. Mater. Chem.* **2006**, *16*, 3091-3098.
  103. Grosso, D.; Cagnol, F.; Soler-Illia, G.; Crepaldi, E.; Amenitsch, H.; Brunet-Bruneau, A.; Bourgeois, A.; Sanchez, C. Fundamentals of Mesostructuring through Evaporation-Induced Self-Assembly. *Adv. Funct. Mater.* **2004**, *14*, 309-322.
  104. Brinker, C.; Frye, G.; Hurd, A.; Ashley, C. Fundamentals of Sol-Gel Dip-Coating. *Thin Solid Films* **1991**, *201*, 97-108.
  105. Brinker, C.; Hurd, A.; Schunk, P.; Frye, G.; Ashley, C. Review of Sol-Gel Thin Film Formation. *J. Non-Cryst. Solids* **1992**, *147-148*, 424-436.
  106. Han, J.; Craighead, H. Separation of long DNA molecules in a microfabricated entropic array. *Science* **2000**, *288* (5468), 1026-1029.
  107. Foquet, M.; Korlach, J.; Zipfel, W.; Webb, W.; Craighead, H. DNA fragment sizing by single molecule detection in submicrometer-sized closed fluidic channels. *Anal. Chem.* **2002**, *74* (6), 1415-1422.
  108. Kasianowicz, J.; Brandin, E.; Branton, D.; Deamer, D. Characterization of individual polynucleotide molecules using a membrane channel. *Proceedings of the National Academy of Sciences of the United States of America* **1996**, *93* (24), 13770-13773.
  109. Li, J.; Stein, D.; McMullan, C.; Branton, D.; Aziz, M.; Golovchenko, J. Ion-Beam sculpting at nanometre length scales. *Nature* **2001**, *412* (6843), 166-169.

110. Saleh, O.; Sohn, L. An artificial nanopore for molecular sensing. *Nano Lett.* **2003**, *3* (1), 37-38.
111. Chang, H.; Kosari, F.; Andreadakis, G.; Alam, M.; Vasmataz, G.; Bashir, R. DNA-mediated fluctuations in ionic current through silicon oxide nanopore channels. *Nano Lett.* **2004**, *4* (8), 1551-1556.
112. Vercoutere, W.; Winters-Hilt, S.; Olsen, H.; Deamer, D.; Haussler, D.; Akeson, M. Rapid discrimination among individual DNA hairpin molecules at single-nucleotide resolution using ion channel. *Nature Biotechnology* **2001**, *19* (3), 248-252.



# CHAPTER 2

## Ion Transport in Mesoporous Silica SBA-16 Thin Film with Three-Dimensional Cubic Structures

*Mesoporous silica SBA-16 thin films with highly ordered 3D cubic structures were synthesized on a Si substrate via the dip-coating method. After these films were filled with KCl aqueous solutions, the ionic current passing through the mesopores was measured by applying DC electric fields. At low ion concentrations, the measured  $I-V$  curves were nonlinear and the current increased exponentially with respect to voltage. As the ion concentration increased, the  $I-V$  curve approached linear behavior. The nonlinear behavior of  $I-V$  curves can be reasonably attributed to the electric potential barrier created in nanopores.*

### 2.1 Introduction

Advances in the synthesis, measurement, and analysis of nanotubes and nanochannels have allowed ion and liquid transport to be routinely examined and controlled in spaces with dimensions that range from 10 to 100 nm [1,2]. Since the distance from the pore wall is close to the Debye length of confined ionic solutions with a wide range of ion concentrations, the field effect control of ion transport could be demonstrated effectively [3]. Furthermore, the enhancement of proton and ion mobility was reported, which was suggested to be due to the hydrogen bond networks forming strongly in a confined nanospace [4]. The

difference in formation and deformation of the hydrogen bond networks in a confined nanospace can create unique water properties, such as high proton mobility[5,6] and low freezing/melting point [7].

Another interesting topic related to ion transport in pores that are a few nanometers in diameter is the effect of an energy barrier either inside the pore or at the pore entrances. In larger diameter pores, even if an electric potential barrier is created inside the pore, counterions mask the barrier completely. Conversely, in pores measuring a few nanometers in diameter, the discreteness of molecules cannot be neglected. Therefore, an electric potential barrier cannot be masked completely. As a result, the barrier affects ion transport, yielding unique transport properties that are observed in many biological systems [8,9]. When we select mesopores with ink-bottle-like pore geometry, the effect of an electric potential barrier on ion transport could be clarified. In such pores, even with a uniform surface charge density, the electric potential barrier could be created inside the pores due to complex geometry.

In this chapter, we focused on ion transport in a well-dimensioned mesoporous silica SBA-16 thin film with a 3D cubic pore structure. It is reported that SBA-16 mesoporous silica has an ink-bottle pore structure with spherical cavities of 9.5 nm diameter that are connected by a narrow cylindrical pore having approximately 2.3 nm diameter and 2.0 nm length [10]. The highly ordered mesoporous silica films and particles have been widely used as catalysts, filters, and adsorbents. However, a limited number of studies have reported the transport

properties of ions and molecules inside the mesopores on electrode surfaces to modify the electrode properties [11,12]. The detailed analysis of transport phenomena inside mesoporous silica remains to be elucidated in order to effectively apply them to various technologies.

## **2.2 Synthesis of SBA-16 thin films with 3D cubic structures**

The poly(ethylene oxide)-poly(propylene oxide)-poly(ethylene oxide) triblock copolymer, F127, was employed as the structure-directing agent for mesoporous silica SBA-16 thin films [13,14]. The film was formed on a Si substrate using the dip-coating method. We referred to the method of synthesis of SBA-16 films with 3D cubic structures that was reported in Kataoka et al [15,16]. Si substrates were first cleaned with n-hexane, acetone, and water assisted by ultrasonication. The substrates were then immersed in piranha solution and subsequently rinsed with pure water. Finally, they were cleaned with 2-propanol using ultrasonication and dried in air. The precursor solution for SBA-16 was prepared as follows: TEOS (Tetraethyl orthosilicate) (2.0 g), EtOH (11.28 g), water (1.40 g), and 1 M HCl (0.20 g) were stirred at 333 K for 30 min. Triblock copolymer F127 (0.35 g) and EtOH (11.28 g) were added to this solution and stirred at room temperature for 30 min. The final molar ratio of the precursor solution was 1:9.2:0.021:51:0.0029 TEOS/H<sub>2</sub>O /HCl/EtOH/F127.

The liquid film of the precursor solution was then formed on a Si substrate using the dip-coating method. The cleaned Si substrate was vertically immersed in

the precursor solution and withdrawn at a rate of  $0.7 \text{ mm s}^{-1}$ . This coating process was performed at 298 K at a relative humidity (RH) of 60% inside a glove box. Subsequently, the coated samples were dried at 343 K for 8 h and calcined at 713 K for 4 h.

The synthesized mesoporous silica films were observed by using a field-emission scanning electron microscope (FE-SEM) (S-4800, Hitachi High-Technologies, Japan). Furthermore, transmission electron microscopy images of the film cross-sections were obtained with a field-emission transmission electron microscope (FE-TEM) (HF-2000, Hitachi High-Technologies, Japan) at an acceleration voltage of 200 kV. The TEM specimen was prepared by ion-thinning the SBA-16 film on the Si wafer.

Figure 2.1(a) shows an FE-SEM image of the uniform open pores, approximately 8 nm in diameter, on the top surface. An  $Im\bar{3}m$  (1, 1, 1) surface plane that possesses 3-fold symmetry appears in this image [15, 16]. Figure 2.1(b) shows a cross-sectional FE-TEM image of the synthesized film. In this image, the film thickness is approximately 35 nm.

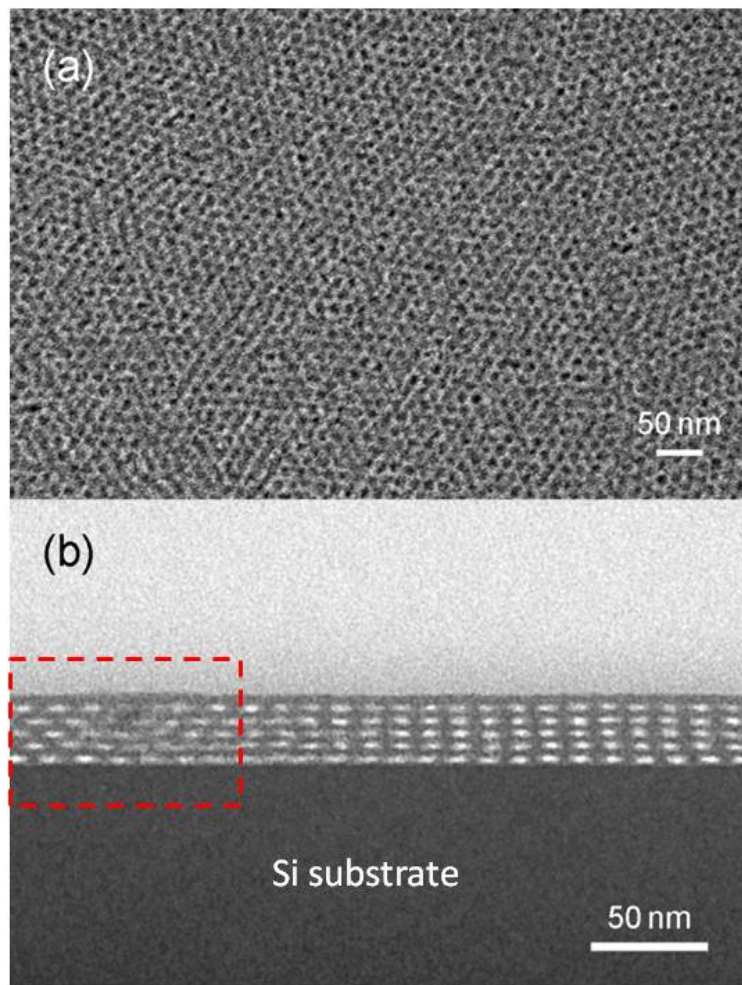


Figure 2.1 (a) FE-SEM image of an SBA-16 film synthesized on a Si substrate on the top surface and (b) FE-TEM image of the film in cross section.

The pores on the left end (the red dotted rectangular) of the film have a checkered flag pattern, where rectangular pores are aligned alternately. Conversely, the pores on the right side have a grid pattern, where rectangular pores are aligned in a row in the film's normal direction. The left side image is the view along the  $[1, 1, 0]$  zone axis, while the right side image is the view along the  $[\bar{2}, 1, 1]$  zone axis. These images suggest that the film thickness and the local pore

alignment were well controlled, while the pores were not aligned perfectly in the 3D cubic structure over the entire film.

In general, the 3D cubic structure,  $Im\bar{3}m$ , can be confirmed by checking 3 fold-symmetry on the surface plane from SEM image. However, in reality, it is very difficult to identify the ink-bottle-like pore structures from TEM and SEM image. The pore size distribution of mesoporous silica powder materials can be determined using the  $N_2$  adsorption–desorption isotherm measurement, while the thin films has great difficulty in confirming the characterization of pore-size distribution because it was difficult to acquire a sufficient amount of sample for the measurement. As a way to identify the 3D cubic structure ( $Im\bar{3}m$ ), Kataoka et al. has applied TEM image viewed from different angle at the same area, [110] zone axis [15]. In the case of the 3D cubic structures, the checkered-flag patterns were viewed at  $0^\circ$  and the grid patterns were observed at  $42.5^\circ$  with respect to [110] zone axis, respectively. The distribution of nanopores viewed at  $42.5^\circ$  correspond with  $(-2\ 1\ 1)$  plane.

### **2.3 Fabrication of a device for ionic current measurement**

To construct a device for ionic current measurement, polydimethylsiloxane (PDMS) reservoirs were fabricated by the standard PDMS chip fabrication processes. Two rectangular parallelepiped reservoir molds of 3 mm (length)  $\times$  1 mm (width)  $\times$  100  $\mu\text{m}$  (depth) were made by patterning a Si wafer. The gap between the two reservoirs was 100  $\mu\text{m}$ . PDMS was mixed in a 10:1 ratio of

monomer and curing agent as per manufacturer instructions (Sylgard 184, Dow Corning, Midland, MI) and then poured over the mold. The PDMS was degassed and cured at 70–80 °C for 20–25 min and then removed from the mold. Two inlet holes were formed on each PDMS reservoir using a 1 mm-diameter disposable biopsy punch with a plunger system (Kai Industries Co. Ltd., Japan). The PDMS reservoirs with inlet holes were then bonded to a Si chip covered with an SBA-16 mesoporous silica thin film. Since SBA-16 mesoporous silica thin films have access holes on the surface due to 3D cubic structures, the PDMS chip was directly bonded without particular treatment to fill with aqueous solutions in nanopores. We referred to the binding procedures reported in Satyanarayana et al [17].

To confirm that there was no leakage on the bonding surface, the PDMS reservoirs were bonded to a Si chip as well as a chip covered with an SBA-16 mesoporous silica thin film and the same ionic current measurements were performed for these two chips. When ionic current measurements were performed using a Si chip without an SBA-16 mesoporous silica thin film bonded with PDMS reservoirs, no ionic currents were detected, suggesting that there was no leakage on the bonding surface. On the other hands, if there is leakage on the bonding surface, the measured current (the order of microampere) was much larger than those (the order of nanoampere) measured on the well-bonded surface. The ionic current is detected in the chip covered with an SBA-16 mesoporous silica thin film bonded with PDMS reservoirs, the ionic current should pass

through an SBA-16 mesoporous silica thin film.

Figure 2.2 shows the schematic of a device for ionic current measurement. To enlarge the reservoirs and maintain a constant ion concentration in the reservoirs, another PDMS layer with two rectangular reservoirs was bonded to the top surface of the device.

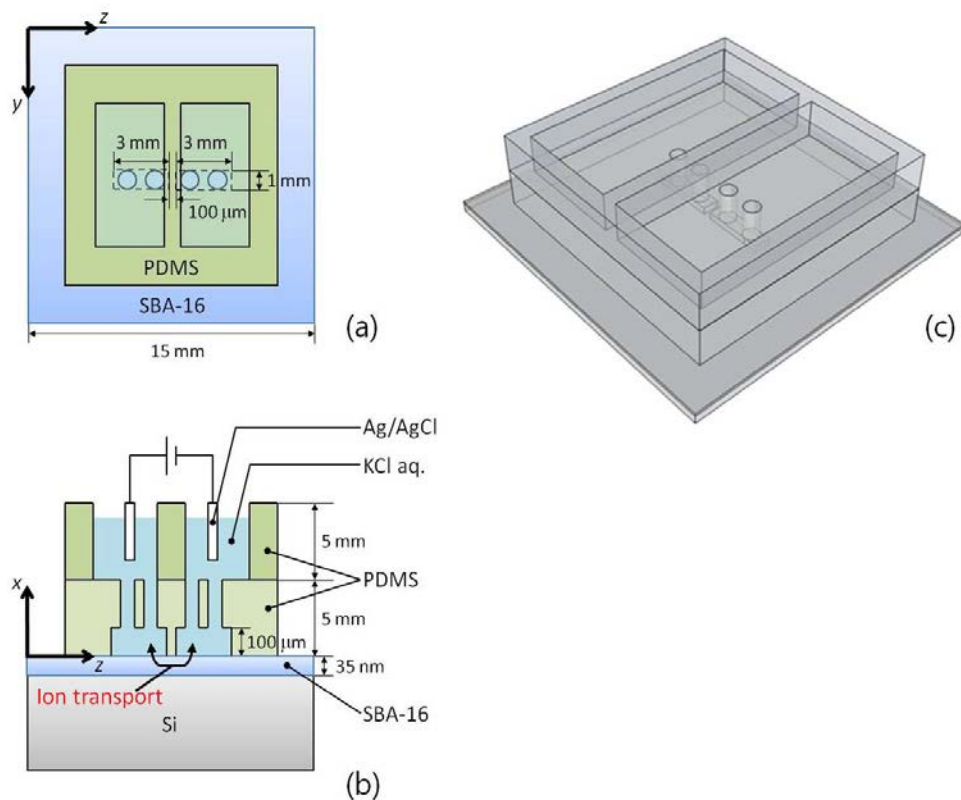


Figure 2.2 Schematic of a device for ionic current measurement. (a) Top view, (b) side view, and (c) general view.

## 2.4 Structure of the synthesized SBA-16 thin film

Figure 2.3 shows the structure of the synthesized SBA-16 thin film. The circles show the spherical cavities. The spherical cavities having 9.5 nm diameters are

arranged in a body-centered-cubic (bcc) array and that the cavities are connected through cylindrical pores of 2.3 nm diameters and 2 nm lengths. The lattice constant of the bcc unit cell is expressed as  $a$ . The FE-SEM and FE-TEM images of the synthesized SBA-16 thin film (Figure 2.1(a) and 2.1(b)) show that the direction of  $[1, 1, 1]$  zone axis is along the  $x$  direction in Figure 2.2.

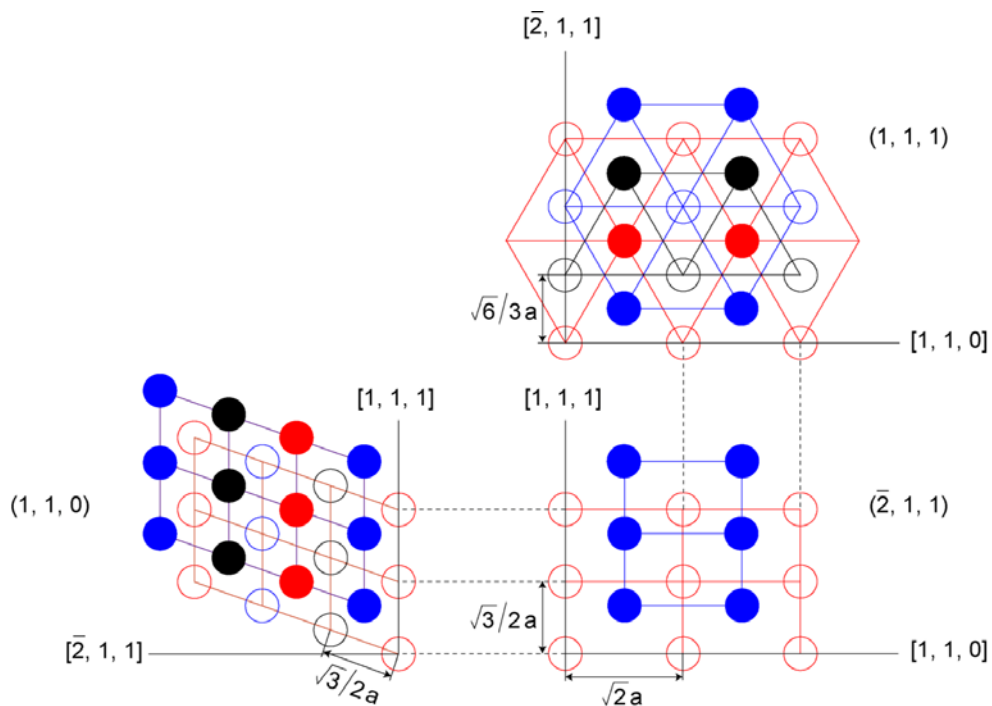


Figure 2.3 Schematic structure of the synthesized SBA-16 thin film.

## 2.5 Measurement of ionic current

Before measuring the ionic current, the reservoirs were filled with KCl aqueous solutions, and then Ag/AgCl electrodes were inserted into the reservoirs. An electric potential bias was applied between the two electrodes, and the ionic current passing through the mesopores was measured by an electrochemical

research system with the femtoammeter option (Modulab System, Solartron Analytical). Furthermore, all measurements were carried out in a shielding box to eliminate the influence of external electromagnetic waves. Ag/AgCl electrodes, fabricated by a chemical method using a chloride solution, were used to measure ionic current. At  $10^{-4}$  and  $10^{-3}$  M, the ionic current measurement was performed in the voltage range from 0 to  $\pm 3.3$  V to detect the nonlinear regime of the ionic current vs. electric potential ( $I-V$ ) curves. At  $10^{-2}$ ,  $10^{-1}$ , and 1 M concentrations, the applied voltage ranged from 0 to  $\pm 4.5$  V because of the expansion of the linear regime. The interval of the applied voltage was 0.3 V.

### 2.5.1 Ionic current–voltage characteristics

Figure 2.4 shows the measured  $I-V$  curves of KCl aqueous solutions with five different concentrations. The measured  $I-V$  curves were almost symmetric and became nonlinear at  $10^{-4}$  and  $10^{-3}$  M despite a linear Ohmic region. Since the narrow pore diameter is approximately 2.3 nm, it is close to the Debye length  $\lambda_D$  of the solution. The  $\lambda_D$  at 300 K was 30.4, 9.7, 3.04, 0.97, and 0.304 nm at  $10^{-4}$ ,  $10^{-3}$ ,  $10^{-2}$ ,  $10^{-1}$ , and 1 M, respectively. At  $10^{-4}$  and  $10^{-3}$  M, the  $\lambda_D$  clearly exceeded the spherical pore radius. In this concentration range, the measured  $I-V$  curves became nonlinear. The nonlinear behavior of  $I-V$  curves observed in nanofluidic diodes can be explained as the accumulation or depletion of ions at the electric potential barrier [18,19].

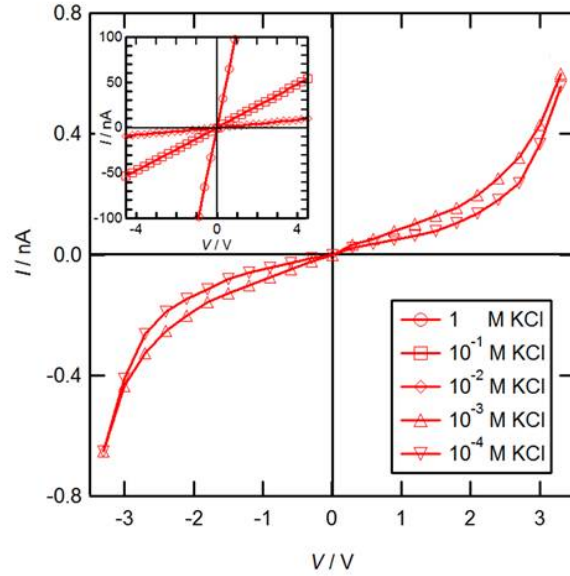


Figure 2.4 Ionic current vs. electric potential bias ( $I-V$ ) curves of an SBA-16 thin film filled with KCl aqueous solutions with concentrations of  $10^{-4}$ ,  $10^{-3}$ ,  $10^{-2}$ ,  $10^{-1}$ , and 1 M.

However, in this concentration range, the pores were filled with a unipolar solution of  $K^+$  and ions could not accumulate inside the pore [20]. Therefore, different mechanism responsible for the nonlinear  $I-V$  curve was required. At  $10^{-2}$ ,  $10^{-1}$  and 1 M, the measured  $I-V$  curves were almost linear.

Figure 2.5 shows the conductance vs. ion concentration ( $G-n$ ) curves. The conductance was calculated from the gradient at the origin in the measured  $I-V$  curves. The result shows that the conductance decreased with decreasing ion concentration and that it decreased rapidly at approximately  $10^{-3}$  M. Figure 2.5 also shows the differential conductance,  $dI/dV$ , at  $|V|=3.15$  V for  $10^{-4}$  and  $10^{-3}$  M KCl aqueous solutions. The  $I-V$  curves of  $10^{-4}$  and  $10^{-3}$  M were nonlinear

and the differential conductance increased with increasing  $|V|$ . These two values were almost the same and approximately 30% of the conductance at  $10^{-2}$  M.

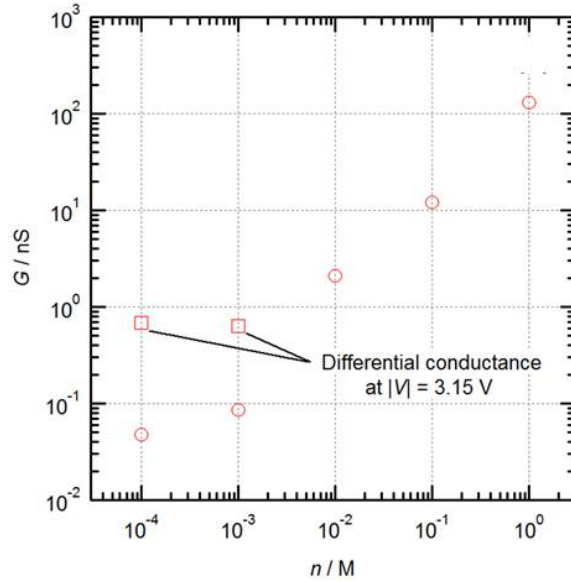


Figure 2.5 The conductance vs. ion concentration ( $G-n$ ) curve.

## 2.5.2 Influence of immersed time for KCl aqueous solution on $I-V$ curves

In the present study, the mesopores were completely filled with KCl aqueous solutions by exposing the device to water vapor for 2 h and then immersing it in deionized (DI) water ( $18.2 \text{ M}\Omega\cdot\text{cm}$ ) for at least 12 h. Finally, the device chip was immersed in KCl aqueous solutions for 12 h to achieve the saturation state. When a KCl aqueous solution was replaced by another solution with a different concentration, the mesopores needed to be rinsed thoroughly with DI water for at

least 12 h so as to restore the silanol group on the silica surface. Ionic conductance along nanochannels, which have a height of approximately 2 nm, has been reported to change with immersed time in the solution owing to a slow protonation exchange process [4]. Ionic conductance through SBA-16 mesoporous silica with an ink-bottle pore structure was investigated. SBA-16 also has narrow cylindrical pores that are approximately 2.3 nm in diameter and 2.0 nm in length, and a dependence of the ionic conductance on the immersed time was observed.

Figure 2.6 shows ionic conductance vs. immersed time curves for KCl aqueous solutions of  $10^{-4}$ ,  $10^{-3}$ ,  $10^{-2}$ ,  $10^{-1}$ , and 1 M concentrations. Since the total length of the mesopores used in the present study was 100  $\mu\text{m}$ , ions should penetrate the mesopores within approximately 5 s in the bulk condition  $t = L^2 D^{-1} = (10^{-4} \text{ m})^2 (2 \times 10^{-9} \text{ m}^2 \text{ s}^{-1})^{-1} = 5 \text{ s}$ .  $D$  is the diffusion coefficient of KCl aqueous solution at 298.15 K. In general, the diffusion coefficient varies with the concentration of aqueous solutions (for instance,  $D$  is  $1.964 \text{ m}^2 \text{ s}^{-1}$  at  $10^{-3} \text{ M}$  KCl and  $1.891 \text{ m}^2 \text{ s}^{-1}$  at 1 M KCl) [21], but in the formula above, the value of  $D$  was assumed to be 2 for simplicity. However, 12 h elapsed before the saturation state was attained at  $10^{-4}$ ,  $10^{-3}$ ,  $10^{-2}$ ,  $10^{-1} \text{ M}$ . Less time was required to attain the saturation state with increasing ion concentrations. At 1 M, approximately 1 h was required, which was still much longer than the estimated time of 5 s. We determined an appropriate immersed time for experimental procedures by considering these experimental results. In order to obtain the ionic conductance in the saturation state, the ionic conductance measurement was carried out after a

nanofluidics device was immersed in the solution for more than 12 h.

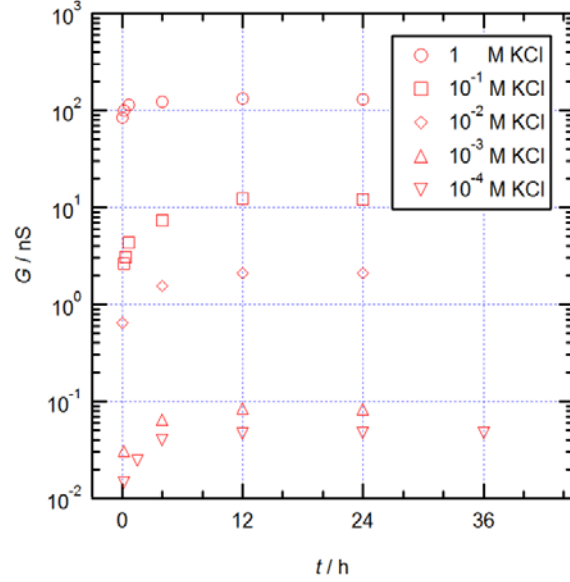


Figure 2.6 Conductance vs. immersed time ( $G-t$ ) curves for KCl aqueous solutions of  $10^{-4}$ ,  $10^{-3}$ ,  $10^{-2}$ ,  $10^{-1}$ , and 1 M concentrations.

### 2.5.3 Details related to the measurement method of $I-V$ curves

In order to obtain the ionic conductance in the steady state, the measurement of ionic conductance was repeated until the conductance reached a constant value. Figure 2.7 shows the measured ionic conductance vs. the number of repeat measurement curves for each ion concentration. At  $10^{-2}$ ,  $10^{-1}$ , and 1 M concentrations, the measured conductance decreased monotonically as the number of repeat measurements increased, and eventually reached a constant value. Conversely, at  $10^{-4}$  and  $10^{-3}$  M concentrations, the measured ionic conductance remained constant, independent of the number of repeat measurements.

At low ion concentrations, it is well known that perm-selective ion transport is generated through mesopores and that the surface charge is dominant because of the overlapping of the electrical double layer [22]. Under such a condition, co-ions are repelled from the entrance of mesopores and only counter-ions pass through the mesopores. Consequently, the measured conductance was independent of the number of repeat measurements in the surface charge governed regime, as shown in Figure 2.7.

In contrast, at high ion concentrations, the ionic conductance depends on the geometry of the mesopores and on the ion concentration. It is reported that SBA-16 mesoporous silica has an ink-bottle pore structure with spherical cavities of 9.5 nm diameter that are connected by a narrow cylindrical pore having approximately 2.3 nm diameter and 2.0 nm length. The junction between the spherical cavity and the narrow cylindrical pores could cause ion concentration polarization (ICP) [23]. As the measurement was repeated, ICP was reduced, and the ionic conductance decreased gradually. The ionic conductance reached a constant value much faster at the  $10^{-2}$  M concentration than at the  $10^{-1}$  and 1 M concentrations. The concentration of  $10^{-2}$  M is in the transition state between the surface charge governed regime and the bulk concentration governed regime. The Debye length of the  $10^{-2}$  M KCl aqueous solution was greater than the cylindrical pore radius and smaller than the spherical pore radius. Thus, both  $K^+$  and  $Cl^-$  ions could be present in the pores. However, most charge carriers were likely to be  $K^+$  ions.

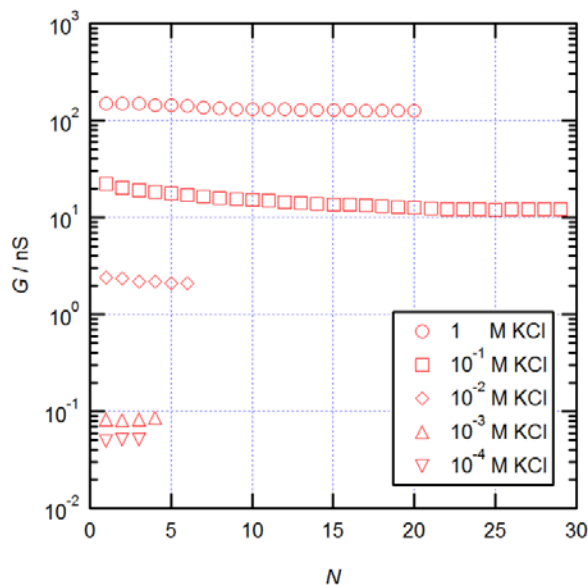


Figure 2.7 Conductance vs. number of repeat measurements ( $G - N$ ) curves for KCl aqueous solutions of  $10^{-4}$ ,  $10^{-3}$ ,  $10^{-2}$ ,  $10^{-1}$ , and 1 M concentrations.

### 2.5.4 Influence of solvent evaporation on $I - V$ curves

When the ionic current passing through an SBA-16 thin film was measured at  $10^{-4}$  and  $10^{-3}$  M concentrations, the relaxation time required to reach the steady state was approximately 3 min owing to electric potential barriers. At  $10^{-4}$  and  $10^{-3}$  M concentrations, ionic current was measured at 22 different electric potential biases from 0 to  $\pm 3.3$  V with an interval of 0.3 V. Accordingly, more than 1 h elapsed while completing a series of measurements. In this situation, the evaporation of solvent due to relative long measurement time can lead to concentration change of the solution inside both reservoirs, affecting the  $I - V$  curve characteristic.

Figure 2.8 shows ionic current vs. electric potential curves of two consecutive measurements for  $10^{-4}$  and  $10^{-3}$  M KCl aqueous solutions. After completing the first series of ionic current measurements, the second series of measurements was performed consecutively in the same condition. The results show that the measured ionic currents were almost the same, especially in the linear regime. When the electric potential bias was more than 2.4 V (in the nonlinear regime), the ionic current of the second measurement was slightly larger than that of the first measurement. This may be attributed to the KCl aqueous solution concentration increase due to the evaporation of solvent. This result suggests that the influence of solvent evaporation on  $I - V$  curves was marginal.

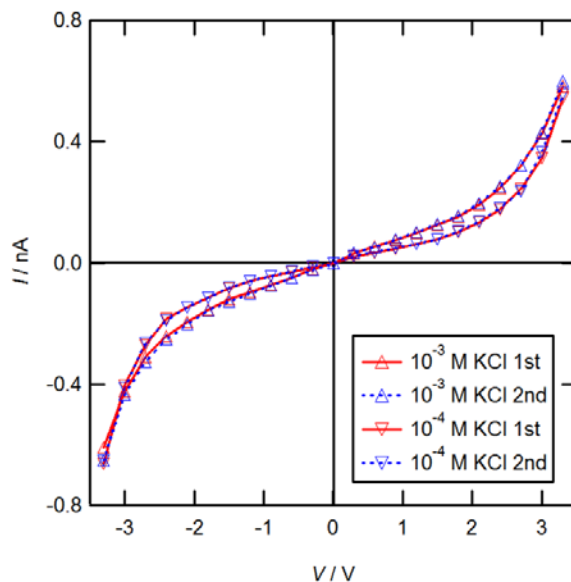


Figure 2.8 Ionic current vs. electric potential ( $I - V$ ) curves of two consecutive measurements for  $10^{-4}$  and  $10^{-3}$  M KCl aqueous solutions.

## 2.5.5 Time courses of ionic current

Figure 2.9(a) and 2.9(b) show the time course of an ionic current passing through an SBA-16 thin film filled with either a  $10^{-4}$ ,  $10^{-3}$ ,  $10^{-2}$ ,  $10^{-1}$ , or 1 M KCl aqueous solution and the time course of the applied electric potential, respectively.

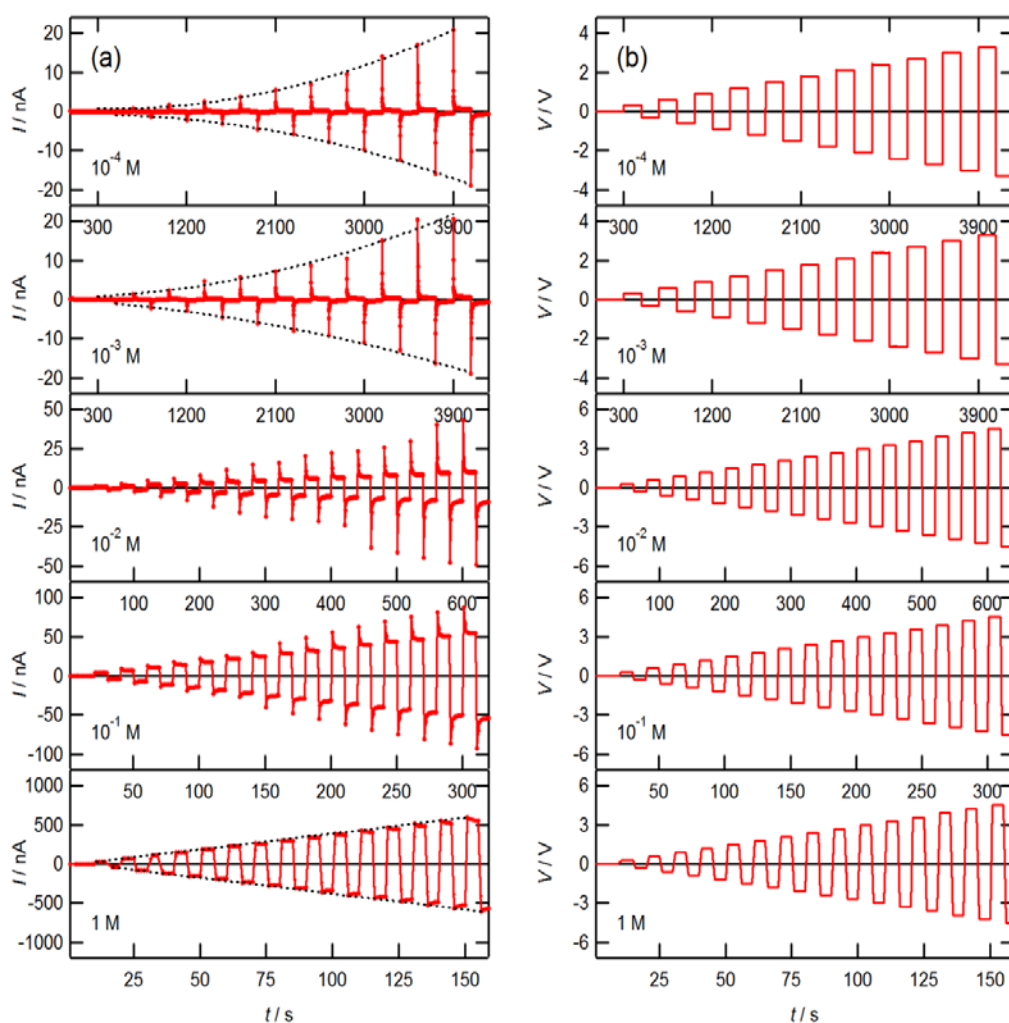


Figure 2.9 (a) Time course of ionic current passing through an SBA-16 thin film filled with either a  $10^{-4}$ ,  $10^{-3}$ ,  $10^{-2}$ ,  $10^{-1}$ , or 1 M KCl aqueous solution and (b) the time course of the applied electric potential.

The pHs of KCl aqueous solutions were 6.5, 6.8, 7.1, 7.4 and 7.8 for  $10^{-4}$ ,  $10^{-3}$ ,  $10^{-2}$ ,  $10^{-1}$  and 1 M, respectively. It took more than 1 h to perform a series of measurements at  $10^{-4}$  and  $10^{-3}$  M; however, we confirmed through the measurements that the influence of solvent evaporation on the  $I-V$  curves was marginal.

Silica surface bears electrostatic charges when it is in contact with a polar liquid. The ion concentration dependence in the time course of an ionic current could be attributed to the surface charge of the mesopores. We proposed a model, in which electric potential barriers were created inside the thin film and ions were either polarized or transported at the electric potential barriers and ions were transported conductively except for the barriers. Figure 2.10 shows the equivalent electric circuit: a capacitance  $C$  and a resistance  $R$  are connected in parallel and the unit is connected to a resistance  $r$  in series.

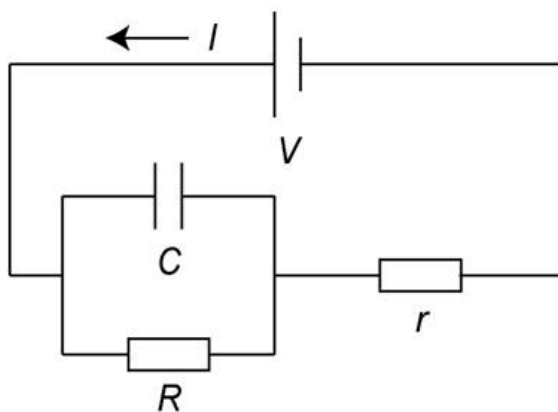


Figure 2.10 Equivalent electric circuit of ion transport in an SBA-16 thin film.

When a step potential  $V$  is applied to the electric circuit at  $t = 0$ , the current  $I(t)$  is given by

$$I(t) = \frac{V}{r+R} + \frac{V-V_{-1}}{r+R} \left( \frac{R}{r} \right) \exp \left[ - \left( \frac{1}{r} + \frac{1}{R} \right) \frac{t}{C} \right] \quad (2.1)$$

, where  $V_{-1}$  is the applied step potential one step before, which is given by  $V_{-1} = -V + \Delta V$ . Here,  $\Delta V$  is the increment of the applied step potential ( $\Delta V = 0$  or  $0.3$  V). If the resistance at the electric potential barriers  $R$  is more dominant than the total resistance  $r$  including the electrodes except for the barriers, i.e.  $\frac{r}{R} \ll 1$ , the current  $I(t)$  is approximately given by

$I(t) \approx \frac{V-V_{-1}}{r} \exp \left( - \frac{t}{rC} \right)$ . On the other hand, if  $r$  is more dominant than  $R$ , i.e.

$\frac{R}{r} \ll 1$ , the current  $I(t)$  is approximately given by  $I(t) \approx \frac{V}{r}$ . Figure 2.9(a) shows

that the current decayed exponentially at  $10^{-4}$  and  $10^{-3}$  M, whereas the current almost remained constant at 1 M. It was suggested that the resistance  $R$  was more dominant at  $10^{-4}$  and  $10^{-3}$  M, whereas the resistance  $r$  was more dominant at 1 M.

The dotted curves in Figure 2.9(a) show the current at  $t = 0$  vs. the applied step potential ( $I_0 - V$ ) curves. The current  $I_0$  is given by  $I_0 = \frac{r + (1 - V_{-1}/V)R}{r + R} \left( \frac{V}{r} \right)$ .

If  $\frac{r}{R} \ll 1$ ,  $I_0 \approx \frac{V - V_{-1}}{r} = \frac{2V - \Delta V}{r}$ .

Whereas, if  $\frac{R}{r} \ll 1$ ,  $I_0 \approx \frac{V}{r}$ . Therefore, the resistance  $r$  should decrease with increasing  $V$  at  $10^{-4}$  and  $10^{-3}$  M, whereas the resistance  $r$  should be a constant at 1 M. This result can reasonably be explained as follows: At low ion concentrations, the electric potential barriers affected ion transport in the entire thin film. As the applied step potential  $V$  increased, ions overcame the electric potential barriers more frequently, thus the resistance  $r$  should decrease with increasing  $V$ . On the other hand, at high ion concentrations, the electric potential barriers were masked by the counterions, thus the resistance  $r$  should be constant. The current in the steady states can be obtained as  $I = \frac{V}{r + R}$  by substituting  $t = \infty$  into Eq. (2.1)

From aforementioned discussion, the current  $I$  is approximately given by  $I \approx \frac{V}{R} (\approx 0)$  at  $10^{-4}$  and  $10^{-3}$  M. On the other hand, the current  $I$  is approximately given by  $I \approx \frac{V}{r} (\approx I_0)$  at 1 M. At  $10^{-4}$  and  $10^{-3}$  M, the resistance  $R$  should also decrease with increasing  $V$  as discussed in the resistance  $r$ . The  $I - V$  curves were analyzed in more detail later on. The time constant to achieve the steady state,  $\tau$ , can be defined as  $\tau = \frac{rR}{r + R} C$  from Eq. (2.1).

Figure 2.9(a) shows that the relaxation time was approximately 3 min at  $10^{-4}$  and  $10^{-3}$  M, whereas it was approximately 5 s at 1 M. Since the resistances of  $r$  and  $R$  decreased with increasing ion concentration and the capacitance  $C$  could

be less sensitive to ion concentration, the relaxation time decreased with increasing ion concentration.

## 2.6 Calculation of 3D electric potential distributions

The transient response of ionic current to a step electric potential and the nonlinear behavior of  $I-V$  curves could be reasonably attributed to the electric potential barrier inside SBA-16 mesoporous silica. To confirm this assumption, a simple model pore was proposed and the electric potential inside the model pore was analyzed. Figure 2.11 shows the calculation system of a model pore. In the hemispherical pore, the position of a given point,  $A(x, y, z)$ , was expressed by the coordinate  $(r, \varphi, \theta)$  as follows:

$$\begin{pmatrix} x \\ y \\ z \end{pmatrix} = \overrightarrow{OO'} + \overrightarrow{O'A} = \pm \begin{pmatrix} 0 \\ 0 \\ r_0 + l/2 \end{pmatrix} + \begin{pmatrix} r \sin \theta \cos \varphi \\ r \sin \theta \sin \varphi \\ r_0 \cos \theta \end{pmatrix}, \quad (2.2)$$

where  $r_0$  is the radius of the spherical pore ( $r_0 = 5$  nm) and  $l$  is the length of the cylindrical pore ( $l = 2$  nm). The sign in the first term was negative for the left hemisphere and positive for the right hemisphere. The range of  $\theta$  was  $0 \leq \theta \leq \pi/2$  for the left hemisphere and  $\pi/2 \leq \theta \leq \pi$  for the right hemisphere. In the cylindrical pore, the position of any point was expressed by the coordinate  $(r, \varphi, z)$ , as follows:

$$\begin{pmatrix} x \\ y \\ z \end{pmatrix} = \begin{pmatrix} r \cos \varphi \\ r \sin \varphi \\ z \end{pmatrix} \quad (2.3)$$

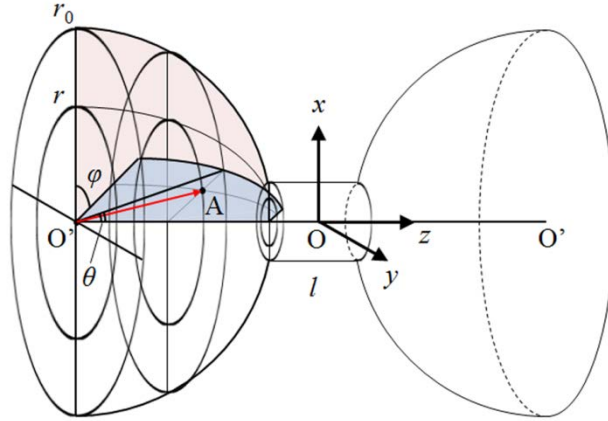


Figure 2.11 Calculation system of a model pore for calculation of 3D electric potential distributions.

The surface charge was assumed to be distributed homogeneously, and its density was assumed to be  $-10^{-2} \text{ C m}^{-2}$  [24]. The electric potential inside the model pore was calculated by solving the Poisson equation under the periodic boundary condition. The calculated electric potential distribution inside three model pores in the  $x-z$  plane was shown in Figure 2.12(a). Assuming that discrete point charges were distributed on the pore surface, the equivalent number of electronic charges was calculated to be 19.2 in the sphere and 0.8 in the cylinder. In this study, 18 negative point charges were located on the surface of the sphere and 1 negative point charge was located on the surface of the cylinder. 18 point charges of  $e^{-}$  were distributed on the surface of the spherical pore, as follows:

$$\begin{pmatrix} r \\ \varphi \\ \theta \end{pmatrix} = \begin{pmatrix} r_0 \\ 0^\circ, 60^\circ, 120^\circ, 180^\circ, 240^\circ, 300^\circ \\ 70^\circ \end{pmatrix}, \begin{pmatrix} r_0 \\ 30^\circ, 150^\circ, 270^\circ \\ 30^\circ \end{pmatrix}, \begin{pmatrix} r_0 \\ 0^\circ, 120^\circ, 240^\circ \\ 150^\circ \end{pmatrix}, \begin{pmatrix} r_0 \\ 30^\circ, 90^\circ, 150^\circ, 210^\circ, 270^\circ, 330^\circ \\ 110^\circ \end{pmatrix} \quad (2.4)$$

On the surface of the cylindrical pore, one point charge of  $e^-$  was located at the following position.

$$\begin{pmatrix} r \\ \varphi \\ z \end{pmatrix} = \begin{pmatrix} r_1 \\ 180^\circ \\ 0 \end{pmatrix} \quad (2.5)$$

, where  $r_1$  is the radius of the cylindrical pore ( $r_1 = 1 \text{ nm}$ ).

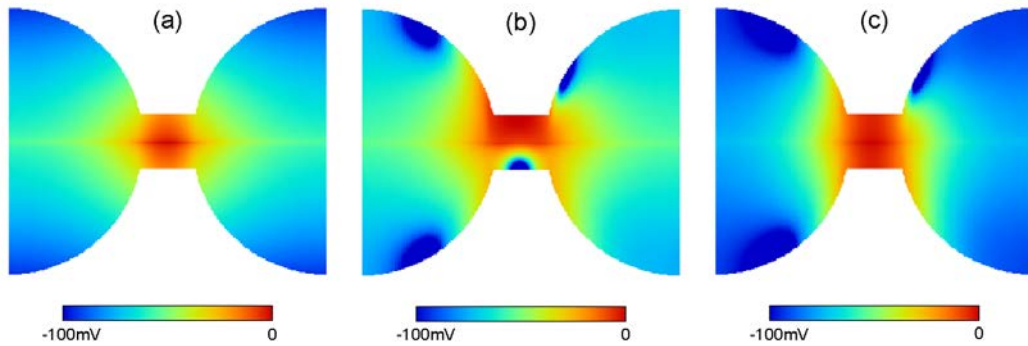


Figure 2.12 Calculated electric potential distribution inside three model pores in the  $x-z$  plane. (a) a uniform surface charge density of  $-10^{-2} \text{ C m}^{-2}$  is assumed to be present on the whole surface, (b) 18 point charges of  $e^-$  are distributed on the surface of the spherical pore and 1 point charge is located on the surface of the cylindrical pore, and (c) 18 point charges of  $e^-$  are distributed on the surface of the spherical pore.

Figure 2.12(b) shows the calculated electric potential distribution in the point charge model. Figure 2.12(c) shows the electric potential distribution when no point charge was located at the cylindrical pore. In both models, an electric potential barrier formed around the cylindrical pore.

Figure 2.13 shows the electric potential profiles along the  $z$ -axis for the three different models.

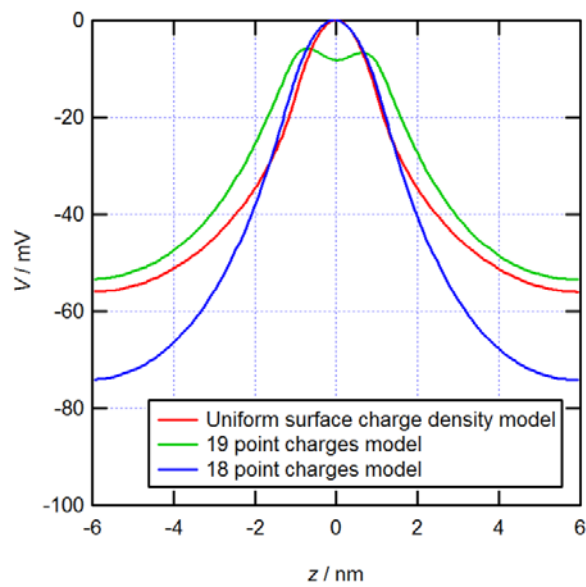


Figure 2.13 Electric potential profiles along the  $z$ -axis for three different models.

When the uniform surface charge density of  $-10^{-2} \text{ C m}^{-2}$  was assumed for the whole surface (Figure 2.12(a)), the electric barrier height was approximately 60 mV. Even when a negative point charge was located on the surface of the cylindrical pore (Figure 2.12(b)), an electric potential barrier of approximately 50 mV formed around the cylindrical pore.

The result shows that the electric potential around the cylinder is higher than that around the sphere, suggesting that an electric potential barrier was created at the cylinder. We confirmed that the similar electric potential distribution could be obtained by assuming discrete point charges on the pore surface, which were equivalent to a uniform surface charge density of  $-10^{-2} \text{ C m}^{-2}$ .

## 2.7 Calculation of 1D PNP equations

To quantitatively discuss the  $I - V$  curve, ionic current in the steady state was analyzed. Ion transport on this scale should be analyzed using stochastic dynamics or molecular dynamics simulations because the multiple interplays between different types of intermolecular interactions characterize the transport [25-28]. Among important three intermolecular forces, since van der waals and electrostatic interactions except for steric interactions can be described as thermophysical properties through continuum dynamics, for larger than  $\sim 5 \text{ nm}$  in diameter, transport phenomena by continuum dynamics provides an reasonable result [29]. In the case of the length scale smaller than  $\sim 5 \text{ nm}$  in diameter, local diffusion coefficient of water decreases compared to the diffusion coefficient of bulk, depending on the location of pores and the degree of silanol density and hydration [30]. For  $\sim 2 \text{ nm}$  in diameter, the diffusion coefficient was approximately  $\sim 85, 60,$  and  $25\%$  of its bulk value in the pore center, in the intermediate between the pore center and surface and on the surface, respectively [31]. However, in this study, we intended to use continuum dynamics simulations

because the main objective of this analysis was to understand the cause of the nonlinear  $I-V$  curve. For simplicity, we assumed that the negatively charged pore was filled with a unipolar solution (including only positive ions) and the system was 1D.

Figure 2.14 shows the model pore consisting of a spherical pore ( $r_0 = 5 \text{ nm}$ ) and a cylindrical pore ( $r_1 = 1 \text{ nm}$  and  $l = 2 \text{ nm}$ ).

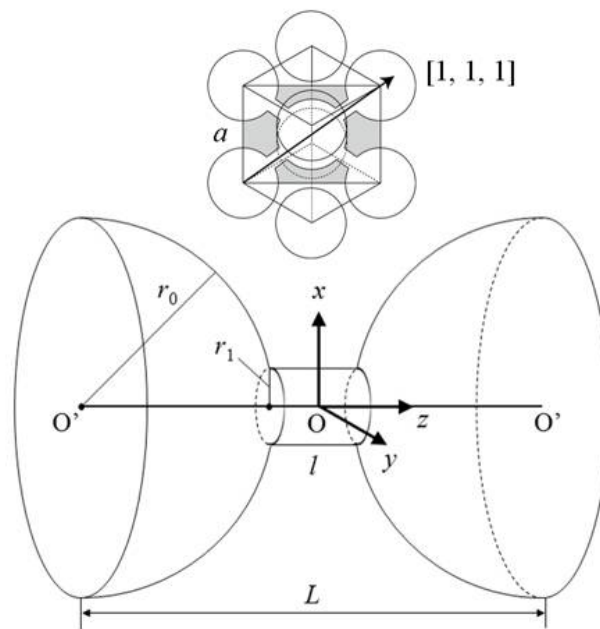


Figure 2.14 Calculation system of a model pore for calculation of 1D PNP equation.

Because the spherical pores were arranged in a body-centered-cubic (bcc) array and that the spherical pores were connected through cylindrical pores, the pore direction ( $z$  axis) of the model pore was along the  $[1, 1, 1]$  zone axis in a bcc array.

The governing equations were the modified Poisson-Nernst-Planck equations.

$$\frac{d^2V}{dz^2} = -\frac{1}{\varepsilon_0\varepsilon} \left( n_a z_a e + \frac{\rho_e}{C_1} \right), \quad (2.6)$$

$$\frac{dJ_a}{dz} = 0 \quad (2.7)$$

, where

$$J_a = -z_a e D_a \left[ C_2 \left( \frac{dn_a}{dz} \right) + \frac{z_a n_a e}{kT} \left( \frac{dV}{dz} \right) \right] \quad (2.8)$$

Here,  $J_a$ ,  $D_a$ ,  $z_a$  and  $n_a$ , are the ionic current density, diffusion coefficient, valence and number density of ion a, respectively.  $V$  is the electric potential,  $\varepsilon_0$  is the permittivity of vacuum,  $\varepsilon$  is the dielectric constant of water,  $e$  is the elementary charge,  $\rho_e$  is the charge density equivalent to the surface charge,  $k$  is the Boltzmann constant, and  $T$  is the absolute temperature.

$C_1$  and  $C_2$  denote two parameters that express the discreteness of molecules in pores which are a few nanometers in diameter. The parameter  $C_1$  ( $0 < C_1 < 1$ ) suppresses the dielectric constant around surface charges. The counterions could be considered electrically well shielded by hydration water molecules, but the surface charges are less shielded. The electric field generated from the surface charge could be more dominant than that generated from counterions; therefore, we introduced parameter  $C_1$ . The parameter  $C_2$  ( $0 < C_2 < 1$ ) suppresses the ion diffusion due to the concentration gradient. Ion diffusion, i.e., the entropic effect toward a homogeneous distribution of ions, could be considered marginal in

comparison with the electrophoresis in pores measuring a few nanometers in diameter. If the temperature decreases, the diffusion effect weakens relative to the electrophoretic effect due to the suppression of the entropic effect, as shown by Eq. (2.8). If the system is confined to pores measuring a few nanometers in diameter, the diffusion effect could also weaken for the same reason. Therefore, we introduced parameter  $C_2$ .

Based on the calculated electric potential distribution inside a model pore as shown in Figure 2.12(a), the equivalent charge density  $\rho_e$  was assumed, and then the modified Poisson-Nernst-Planck equations were solved using a finite difference algorithm. The charge density,  $\rho_e$ , in Eq. (2.6) is given by

$$\rho_e(z) = \bar{\rho}_e + \tilde{\rho}_e(z) \quad (2.9)$$

, where  $\bar{\rho}_e$  is the average component and  $\tilde{\rho}_e$  is the variation component.  $\rho_e$  was determined by the following procedure. First, the calculated electric potential inside the model pore was simplified as follows:

$$V(z) = V_0 \cos(2\pi z/L) \quad (2.10)$$

, where  $V_0$  is the amplitude of the electric potential and  $L$  is the unit length of the model pore. The equivalent charge density,  $\tilde{\rho}_e$ , required to determine the above electric potential,  $V(z)$ , was given by

$$\tilde{\rho}_e(z) = \rho_{e0} \cos(2\pi z/L) \quad (2.11)$$

, where  $\rho_{e0} = \varepsilon_0 \varepsilon V_0 (2\pi/L)^2$ . The average charge density,  $\bar{\rho}_e$ , was given by  $\bar{\rho}_e = -\rho_{e0}$ . From Figure 2.14, the lattice constant of the bcc unit cell,  $a$ , and is given by

$$a = \frac{2\sqrt{3}}{3} L \quad (2.12)$$

Assuming that the direction of  $[1, 1, 1]$  zone axis was along the  $x$  direction and the direction of  $[\bar{2}, 1, 1]$  zone axis was along the  $z$  direction of a device for ionic current measurement (see Figure 2.2 and 2.3), the number density of the pores in the  $(\bar{2}, 1, 1)$  surface plane,  $n$ , is given by

$$n = \frac{2}{\frac{\sqrt{3}}{2} a \times \sqrt{2} a} = \frac{2\sqrt{6}}{3a^2} \quad (2.13)$$

If the cross-sectional area in the  $(\bar{2}, 1, 1)$  surface plane was  $A$ , then the total number of pores that the ionic current would pass through, namely,  $N$ , is given by

$$N = nA \quad (2.14)$$

From the requirement of electro-neutrality, the effective cross-sectional area of ionic current for each pore,  $A_{\text{eff}}$ , is given by

$$A_{\text{eff}} = \frac{\sigma S}{\bar{\rho}_e L} \quad (2.15)$$

, where  $L$ ,  $S$ , and  $\sigma$  are the length, surface area, and surface charge density of the model pores, respectively. The ionic current should flow along the  $[1, 1, 1]$

zone axis, but the  $[\sqrt{2}, 1, 1]$  zone axis was assumed to be along the  $z$  direction of a device for ionic current measurement, thus the travel distance of ions was  $\sqrt{2}$  times larger than the linear distance along the  $[\sqrt{2}, 1, 1]$  zone axis (see Figure 2.3). The ratio between the travel distance and linear distance of ions was defined as the parameter  $R$ . From Eqs. (2.12)–(2.15) and the parameter  $R$  ( $=\sqrt{2}$ ), the measured current,  $I$ , could be estimated using the calculated current density,  $J$ , as follows:

$$I = \frac{NA_{\text{eff}}}{R} J = \alpha AJ, \quad (2.16)$$

where  $\alpha$  is a conversion factor, which is given by  $\alpha = \sqrt{3}\sigma S/2\bar{\rho}_e L^3$ . The parameters employed in this study are as follows:  $D_{\text{K}^+} = 1.96 \times 10^{-9} \text{ m}^2 \text{ s}^{-1}$ ,  $L = 12 \text{ nm}$ ,  $S = 102\pi \text{ nm}^2$ ,  $T = 300 \text{ K}$ ,  $V_0 = 30 \text{ mV}$ ,  $\varepsilon = 80$ , and  $\sigma = 10^{-2} \text{ C m}^{-2}$ . The calculated  $\bar{\rho}_e$  and  $\alpha$  are  $5.82 \times 10^6 \text{ C m}^{-3}$  or 60 mM and 0.276, respectively. It is noted that if the direction of  $[1, 1, 1]$  zone axis is along the  $z$  direction of a device for ionic current measurement,  $R = 1$  and  $\alpha = 3\sqrt{3}\sigma S/4\bar{\rho}_e L^3 = 0.414$ .

## 2.8 Influence of parameters $C_1$ and $C_2$ on $J$ – $V$ curves

Figure 2.15 shows the calculated  $\text{K}^+$  current density vs. the electric potential bias ( $J$ – $V$ ) curves. When  $C_1 = 1$  and  $C_2 = 1$ , the  $J$ – $V$  curve was almost linear.

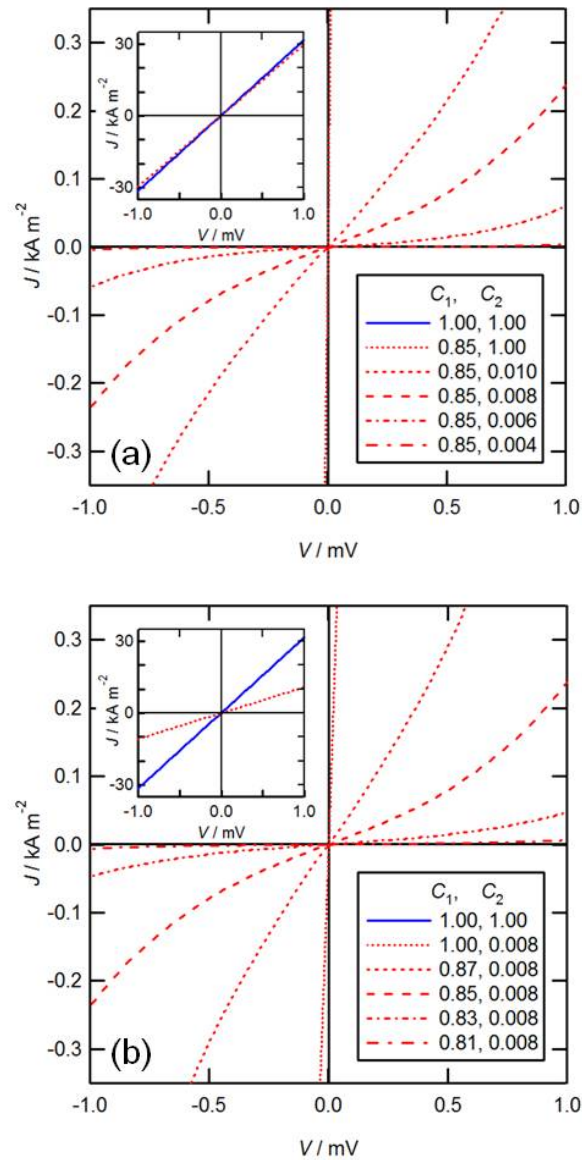


Figure 2.15 Calculated  $K^+$  current density vs. electric potential bias ( $J-V$ ) curves showing (a) the effect of  $C_2$  and (b) the effect of  $C_1$  on  $J-V$  curves.

Even when potential barriers were located inside the pore, the  $J-V$  curve calculated by the Poisson-Nernst-Planck equations was almost linear. When  $C_1$

remained constant at 0.85 and  $C_2$  decreased, the curvature of the  $J-V$  curves increased, as shown in Figure 2.15(a). As  $C_2$  decreased, ions moved while electrophoretically obeying the local electric field rather than obeying the local ion concentration gradient. Thus, the  $J-V$  curve became nonlinear.

When  $C_2$  remained constant at 0.008 and  $C_1$  decreased, the curvature of  $J-V$  curves also increased, as shown in Figure 2.15(b). As  $C_1$  decreased, i.e., as the electric field generated from surface charges became more dominant, the electric field generated from counterions became less dominant, and a larger external electric field was required to overcome the electric barrier. As  $C_1$  and  $C_2$  decreased, the distributions of the electric potential and ion concentration increased, i.e., the effect of the electric potential barrier on ion transport increased, yielding nonlinear  $J-V$  curves.

However, it was difficult to distinguish between the effects of  $C_1$  and  $C_2$  on the  $J-V$  curves within a range of electric potential bias from -1 to 1 mV as shown in Figure 2.15(a) and 2.15(b). To clarify the effects of parameters  $C_1$  and  $C_2$  on  $J-V$  curves, the calculated  $J-V$  curves in a wider range of electric potential bias from -50 to 50 mV are shown in Figure 2.16. Figure 2.16(a) shows the calculated  $J-V$  curves showing the effect of  $C_1$  at  $C_2 = 1$ . The calculated  $J-V$  curves were linear at any  $C_1$  if  $C_2$  remained constant at 1, suggesting that the parameter  $C_2$  is critical for nonlinear behavior of  $J-V$  curves. Figure 2.16(b) shows the calculated  $J-V$  curves showing the effect of  $C_2$  at  $C_1 = 0.85$ . As  $C_2$

decreased, the curvature of  $J - V$  curves increased and approached to a nonlinear  $J - V$  curve.

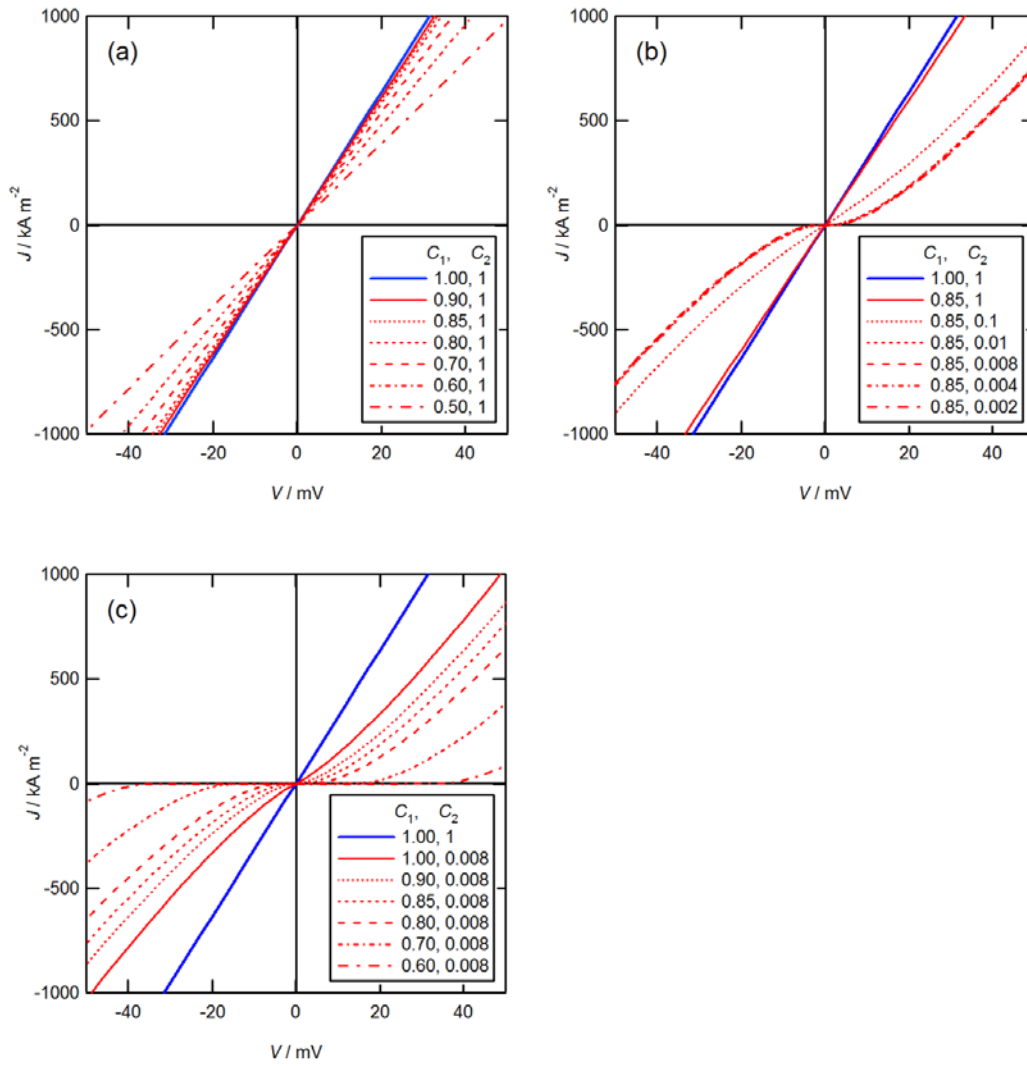


Figure 2.16 Calculated  $K^+$  current density vs. electric potential bias ( $J - V$ ) curves showing (a) the effect of  $C_1$  at  $C_2 = 1$ , (b) the effect of  $C_2$  and (c) the effect of  $C_1$  on  $J - V$  curves.

Figure 2.16(c) shows the calculated  $J - V$  curves showing the effect of  $C_1$  at  $C_2 = 0.008$ . As  $C_2$  decreased, the electric potential bias at which the current

began to increase exponentially increased, suggesting that the parameter  $C_1$  controls the height of electric potential barrier. The parameters  $C_1$  and  $C_2$  affect  $J-V$  curves in totally different ways. However, within a range of electric potential bias from -1 to 1 mV, which was close to that in the experiment, it was difficult to distinguish between the effects of  $C_1$  and  $C_2$  on the  $J-V$  curves.

## 2.9 Comparison between experiment and calculation of conductance

Finally, the calculated results were compared with the experimental results. The model pore was filled with a unipolar solution of  $K^+$ , with  $J = 3.16 \times 10^4 \text{ A m}^{-2}$ , at 1.0 mV for  $C_1 = C_2 = 1$ . The electric potential bias of 1.0 mV for a 12 nm long pore corresponds to 8.33 V for a 100  $\mu\text{m}$  long pore. In addition, assuming that the cross sectional area  $A = 1.0 \text{ mm} \times 35 \text{ nm}$  and the conversion factor  $\alpha = 0.276$ ,  $J = 3.16 \times 10^4 \text{ A m}^{-2}$  corresponds to  $I = 3.05 \times 10^2 \text{ nA}$ . Thus, the conductance is 36.6 nS. In contrast, when the model pore is filled with a 1 M KCl aqueous solution,  $J = 1.22 \times 10^6 \text{ A m}^{-2}$  at 1.0 mV for  $C_1 = C_2 = 1$ , yielding the conductance  $G = 1.41 \mu\text{S}$ . Here, the diffusivity of  $\text{Cl}^-$  was assumed to be  $D_{\text{Cl}^-} = 2.03 \times 10^{-9} \text{ m}^2 \text{ s}^{-1}$ . Ideally, in the surface charge governed regime, the conductance should remain constant at  $G = 36.6 \text{ nS}$ , whereas in the bulk concentration governed regime, the conductance should be proportional to the bulk concentration.

Figure 2.17 shows these model calculation results. However, it could be said that for 1 M KCl aqueous solution, the measured value was 9.3% of the calculated value, because 131 nS (measured) divided by 1.41  $\mu$ S (calculated) equals 0.093. In the synthesized SBA-16 mesoporous silica thin film, the pores were not aligned perfectly and the grain boundaries were included. Thus, this reduction is reasonable. For simplicity, we assumed that the cross-sectional area was 9.3% of that considered in the former calculation. The corresponding results are shown as a modified model calculation in Figure 2.17. The measured conductance at  $10^{-2}$  M was similar to that obtained in the modified calculation result and the measured values of differential conductance at  $|V| = 3.15$  V for  $10^{-4}$  and  $10^{-3}$  M KCl solutions were approximately 20% of the calculated values. However, the measured conductance at  $10^{-3}$  and  $10^{-4}$  M was still 10–100 times smaller than the calculated value. This was attributed to the electric potential barrier created by the ink-bottle pore structure and the resulting nonlinear  $I - V$  curves.

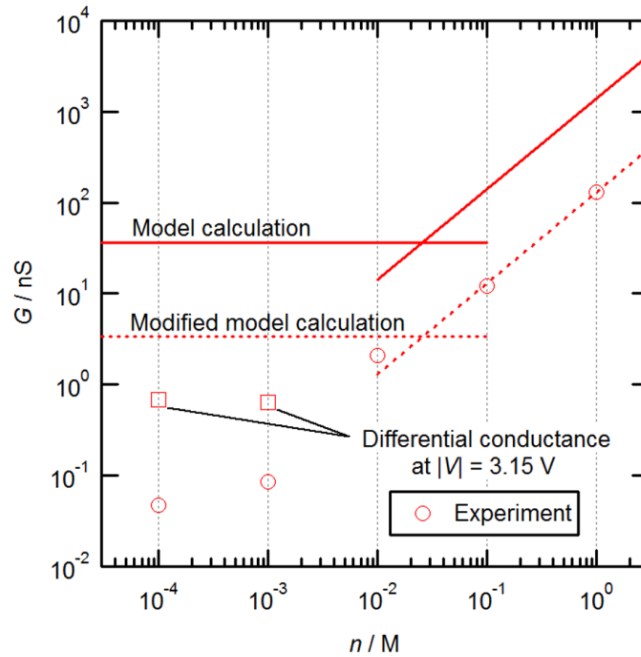


Figure 2.17 Comparison between calculated and experimental results of the conductance vs. ion concentration ( $G - n$ ) curves.

## 2.10 Experimental reproducibility of $I-V$ curves

In order to confirm experimental reproducibility of the measured  $I-V$  curves, we have measured total 12 times (4 times a day) for 5 days on identical device and conditions such as temperature, aqueous solution concentrations and applied potential bias range. After completing the measurement of  $I-V$  curves, the nanofluidic device chip was rinsed for 12 hrs to restore initial condition (silanol group state of inner surface) before measurement of the ionic current passing through nanopores. Figure 2.18 shows the measured  $I-V$  curves to check the experimental reproducibility of the nonlinear behavior at  $10^{-4}$  M KCl aqueous

solution, which is the surface charged governed regime. The standard deviation of the measured  $I-V$  curves was within  $\sim 4\%$  from the mean value.

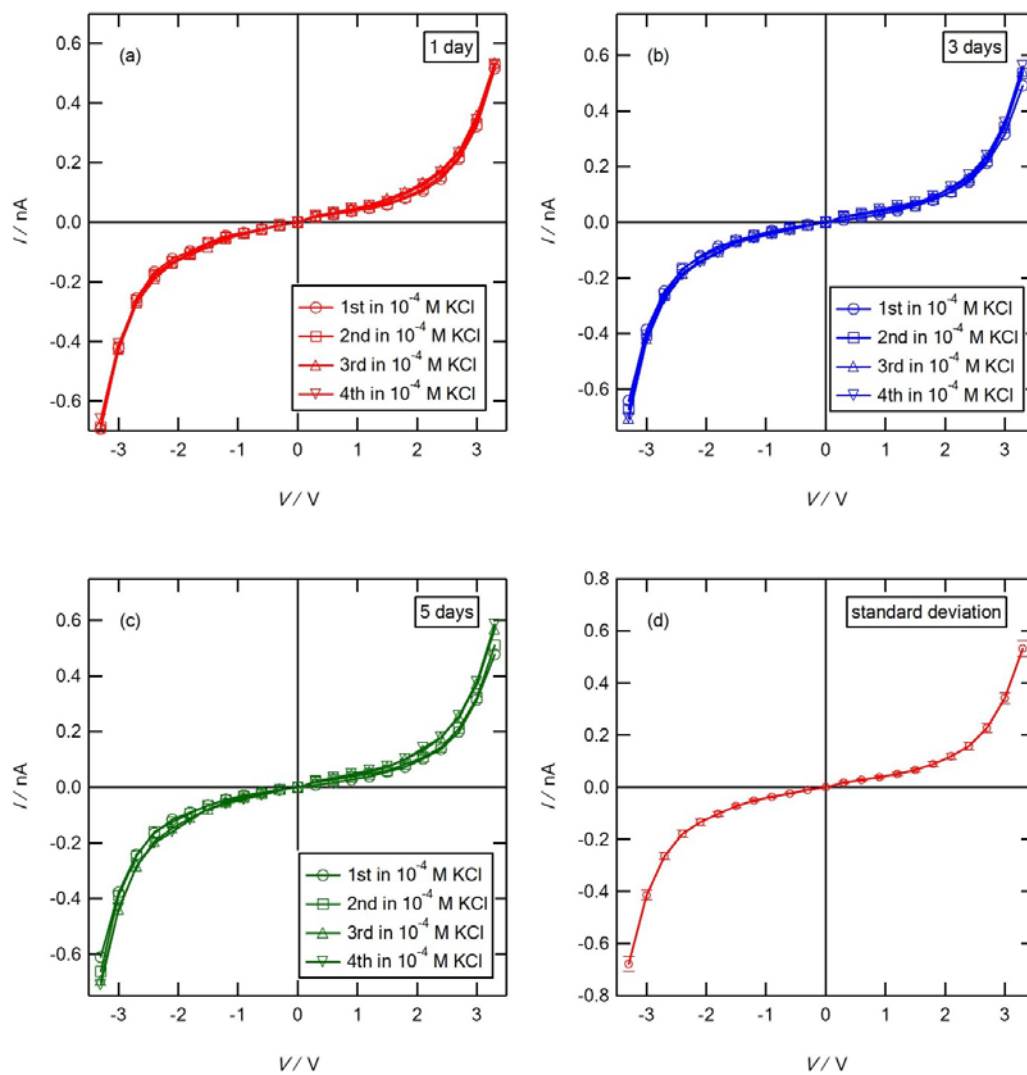


Figure 2.18 The measured  $I-V$  curves to confirm reproducibility at  $10^{-4}$  M KCl aqueous solution: (a) 1 day, (b) 3 days, (c) 5 days, and (d) standard deviation, respectively.

## 2.11 Conclusion

In this chapter, (1) mesoporous silica SBA-16 thin films with highly ordered 3D cubic structures were synthesized on a Si substrate, (2) the ionic currents of KCl aqueous solutions passing through the mesopores were measured by applying DC electric fields, and (3) the measured  $I-V$  curves were analyzed. The measured  $I-V$  curves were nonlinear when the Debye length of the solution clearly exceeded the spherical pore radius. As the ion concentration increased, the  $I-V$  curve approached linear behavior. More precise control of the pore structure and a more quantitative analysis of the measured  $I-V$  curves are required for a complete understanding of this mechanism; however, the nonlinear behavior of  $I-V$  curves at low ion concentrations can be reasonably attributed to the electric potential barrier created in pores measuring a few nanometers in diameter.

## 2.11 Reference

1. Sparreboom, W.; Berg, A. v. d.; Eijkel, J. Principle and applications of nanofluidic transport. *Nat Nanotechnol.* **2009**, *4*, 713-720.
2. Abgrall, P.; Nguyen, N. Nanofluidic devices and their applications. *Anal. Chem.* **2008**, *80*, 2326-2341.
3. Karnik, R.; Fan, R.; Yue, M.; Li, D.; Yang, P.; Majumdar, A. Electrostatic Control of Ions and Molecules in Nanofluidic Transistor. *Nano Lett.* **2005**, *5* (5), 943-948.
4. Duan, C.; Majumdar, A. Anomalous ion transport in 2-nm hydrophilic nanochannels. *Nat Nanotechnol.* **2010**, *5*, 848-852.
5. Dellago, C.; Naor, M.; Hummer, G. Proton Transport through Water-Filled Carbon Nanotubes. *Phys. Rev. Lett.* **2003**, *90*, 105902.
6. Schmidt, R.; Hansen, E.; Stoecker, M.; Akporiaye, D.; Ellestad, O. Pore size determination of MCM-51 mesoporous materials by means of <sup>1</sup>H NMR Spectroscopy, N<sub>2</sub> adsorption, and HREM. A Preliminary study. *J. Am. Chem. Soc.* **1995**, *117* (14), 4049-4056.
7. Schreiber, A.; Ketelsen, I.; Findenegg, G. Melting and freezing of water in ordered mesoporous silica materials. *Phys. Chem. Chem. Phys.* **2001**, *3*, 1185-1195.
8. Cooper, K.; Jakobsson, E.; Wolynes, P. *Prog. Biophys. Mol. Biol.* **1985**, *46*, 51-96.
9. Hille, B. *Ion Channels of Excitable Membranes*, 3rd ed.; Sinauer Associates Inc.: Sunderland, MA, 2001.
10. Sakamoto, Y.; Kaneda, M.; Terasaki, O.; Zhao, D.; Kim, J.; Stucky, G.; Shin, H.; Ryoo, R. Direct imaging of the pores and cages of three-dimensional mesoporous materials. *Nature* **2000**, *408*, 449-453.
11. Song, C.; Villemure, G. Electrode modification with spin-coated films of mesoporous molecular sieve silicas. *Microporous Mesoporous Mater.* **2001**, *44-45*, 679-689.
12. Etienne, M.; Quach, A.; Grosso, D.; Nicole, L.; Sanchez, C.; Walcarius, A. Molecular Transport into Mesoporous Silica Thin Films: Electrochemical Monitoring and Comparison between p6m, P63/mmc, and Pm3n Structures. *Chem. Mater.* **2007**, *19*, 844-856.
13. Zhao, D.; Yang, P.; Melosh, N.; Feng, J.; Chmelka, B.; Stucky, G. Continuous Mesoporous Silica Films with Highly Ordered Large Pore Structures. *Adv. Mater.* **1998**, *10* (16), 1380-1985.
14. Zhao, D.; Huo, Q.; Feng, J.; Chmelka, B.; Stucky, G. Nonionic Triblock and Star Diblock Copolymer and Oligomeric Surfactant Syntheses of highly Ordered, hydrothermally Stable, Mesoporous Silica Structures. *J. Am. Chem. Soc.* **1998**, *120* (24), 6024-6036.
15. Kataoka, S.; Endo, A.; Harada, A.; Inagi, Y.; Ohmori, T. Characterization of mesoporous catalyst supports on microreactor walls. *Applied Catalysis A: General* **2008**, *342* (1-2), 107-112.
16. Kataoka, S.; Endo, A.; Harada, A.; Ohmori, T. Fabrication of mesoporous silica thin films inside microreactor. *Mater. Lett.* **2008**, *62*, 723-726.
17. Satyanarayana, S.; Karnik, R.; Majumdar, A. Stamp-and-stick room-temperature

- bonding technique for microdevices. *IEEE J. Microelectromechanical Syst.* **2005**, *14*, 392-399.
18. Daiguji, H.; Oka, Y.; Shirono, K. Nanofluidic Diode and Bipolar Transistor. *Nano Lett.* **2005**, *5* (11), 2274-2280.
  19. Karnik, R.; Duan, C.; Castelino, K.; Daiguji, H.; Majumdar, A. Rectification of Ionic Current in a Nanofluidic Diode. *Nano Lett.* **2007**, *7* (3), 547-551.
  20. Daiguji, H.; Yang, P.; Majumdar, A. Ion Transport in Nanofluidic Channels. *Nano Lett.* **2004**, *4* (1), 137-142.
  21. Victor, L.; Ana, R.; Luis, V. Diffusion Coefficients in Aqueous Solutions of Potassium Chloride at High and Low Concentrations. *Journal of Molecular Liquids* **1998**, *78*, 139-149.
  22. Stein, D.; Kruithof, M.; Dekker, C. Surface-charge-governed ion transport in nanofluidic channels. *Phys. Rev. Lett.* **2004**, *93*, 035901.
  23. Kim, S.; Wang, Y.; Lee, J.; Jang, H.; Han, J. Concentration Polarization and Nonlinear Electrokinetic Flow near a Nanofluidic Channel. *Physical Review Letters* **2007**, *99*, 044501.
  24. Salis, A.; Parsons, D. F.; Boström, M.; Medda, L.; Barse, B.; Ninham, B. W.; Monduzzi, M. Ion Specific Surface Charge Density of SBA-15 Mesoporous Silica. *Langmuir* **2010**, *26* (4), 2484-2490.
  25. Chung, S. H.; Hoyles, M.; Allen, T.; Kuyucak, S. Study of Ionic Currents across a Model Membrane Channel Using Brownian Dynamics. *Biophys. J* **1998**, *75* (2), 793-809.
  26. Moy, G.; Corry, B.; Kuyucak, S.; Chung, S. H. Tests of Continuum Theories as Models of ion Channels. I. Poisson-Boltzmann Theory versus Brownian Dynamics. *BioPhys. J* **2000**, *78* (5), 2349-2263.
  27. Corry, B.; Kuyucak, S.; Chung, S. H. Test of Continuum Theories as Model of Ion Channels. II. Poisson-Nernst-Planck Theory versus Brownian Dynamics. *BioPhys. J* **2000**, *78* (5), 2364-2381.
  28. Shirono, K.; Tatsumi, N.; Daiguji, H. Molecular Simulation of Ion Transport in Silica Nanopores. *J. Phys. Chem. B* **2009**, *113* (4), 1041-1047.
  29. Daiguji, H. Ion transport in nanofluidic channels. *Chem. Soc. Rev.* **2010**, *39*, 901-911.
  30. Shirono, K.; Daiguji, H. Molecular Simulation of the Phase Behavior of Water Confined in Silica Nanopores. *J. Phys. Chem. C* **2007**, *111*, 7938-7946.
  31. Siboulet, b.; Molina, J.; Coasne, B.; Turq, P.; Dufreche, F. Water self-diffusion at the surface of silica glasses: effect of hydrophilic to hydrophobic transition. *Molecular Physics* **2013**, *111*, 3410-3417.



# CHAPTER 3

## Proton Transport in Mesoporous Silica SBA-16 Thin Film

*In this chapter, we elucidated proton transport phenomena through mesopores of SBA-16 thin films. At low concentrations, ranging from  $10^{-7}$  to  $10^{-5}$  M, the  $I$ - $V$  curves of KCl and HCl aqueous solutions were nonlinear. However, at  $10^{-4}$  and  $10^{-3}$  M, while  $I$ - $V$  curves of KCl aqueous solutions displayed nonlinear behavior, those of HCl aqueous solutions were almost linear. The linear behavior can be attributed to a decrease in the electric potential barrier owing to a reduction in the surface charge density, which is caused by the protonation of silanol groups on the inner surface of mesopores. At high concentrations, ranging from  $10^{-2}$  to 1 M, the  $I$ - $V$  curves of KCl and HCl aqueous solutions were almost linear because the effect of surface charge of mesopores on ion transport was marginal.*

### 3.1 Introduction

In the case of ink-bottle-like mesopores (diameters less than 10 nm) of mesoporous silica SBA-16 thin films with a 3D cubic pore structure, the measured  $I$ - $V$  curves are nonlinear, owing to electric potential barriers inside mesopores at low ion concentrations. In chapter 2, theoretical analysis showed that the electric potential barriers were created because of the surface charge of silica pores that have ink-bottle-like pore geometry and pore diameter of a few nanometers. Furthermore, we found that the local dielectric constant of aqueous solutions around surface charge and the ion diffusion due to concentration gradient should

be suppressed, in order to attain nonlinear  $I$ - $V$  curves in the continuum dynamics calculations of ion transport.

For better estimation of ion transport of aqueous solutions confined in mesopores, we have to consider the discreteness of molecules, i.e., the hydration structure around surface charge and the ion distribution of aqueous solutions in mesopores. However, experimental work on the effect of electric potential barriers on ion transport has not yet been performed. If mesopores of SBA-16 thin films are filled with HCl aqueous solutions, the electric potential barrier could be tuned by the concentration of solutions because the surface charge density on the inner surface of mesopores could change owing to protonation /deprotonation of silanol groups.

In this chapter, we investigated proton transport of HCl aqueous solutions confined in a well-ordered mesoporous silica SBA-16 thin film with a 3D cubic pore structure, using electrochemical measurements. The proton transport of water or aqueous solutions confined in nanopores of various materials plays an important role in science and technological applications such as cell pH stabilization [1], formation of ATP (adenosine triphosphate) in biological system [2], and in the operation of fuel cells [3,4] and electrochemical sensors [5]. However, ion channels of biological systems [6] and polymer electrolyte membranes (e.g., Nafion by DuPont) [7,8] usually possess highly complex structures. This study could be fundamental for understanding proton transport in various pores with complex structures and with diameters of a few nanometers.

## 3.2 Measurement of proton current

Before starting the ionic current measurements, a nanofluidic device was hydrothermally treated in an autoclave using 0.1 M HCl vapor at 393 K for 3 h, in order to improve the hydrophilicity of the inner surface of SBA-16 thin films, since as-made mesoporous silica had low surface charge density because of low wettability. In order to measure ionic or proton current passing through mesopores, the reservoirs of nanofluidic device and mesopores of the SBA-16 thin film were filled with either HCl or KCl aqueous solutions, with concentrations of  $10^{-7}$ ,  $10^{-6}$ ,  $10^{-5}$ ,  $10^{-4}$ ,  $10^{-3}$ ,  $10^{-2}$ ,  $10^{-1}$ , or 1 M, and Ag/AgCl electrodes were inserted into both reservoirs. The ionic or proton current measurement was performed using an electrochemical system (ModuLab System, Solartron Analytical) in the voltage range of 0 to  $\pm 4.5$  V and an applied voltage interval of 0.3 V. All measurements were carried out in a shielding box at room temperature (298 K) to eliminate the influence of external electromagnetic waves.

### 3.2.1 Effect of concentration on $I$ - $V$ curves of HCl and KCl aqueous solutions

Figure 3.1 shows the measured  $I$ - $V$  curves of HCl and KCl aqueous solutions with concentration ranging from  $10^{-7}$  to 1 M. SBA-16 mesoporous silica has spherical cavities with diameters of 9.5 nm, which are connected by a narrow cylindrical pore with diameter and length of approximately 2.3 nm and 2.0 nm [9].

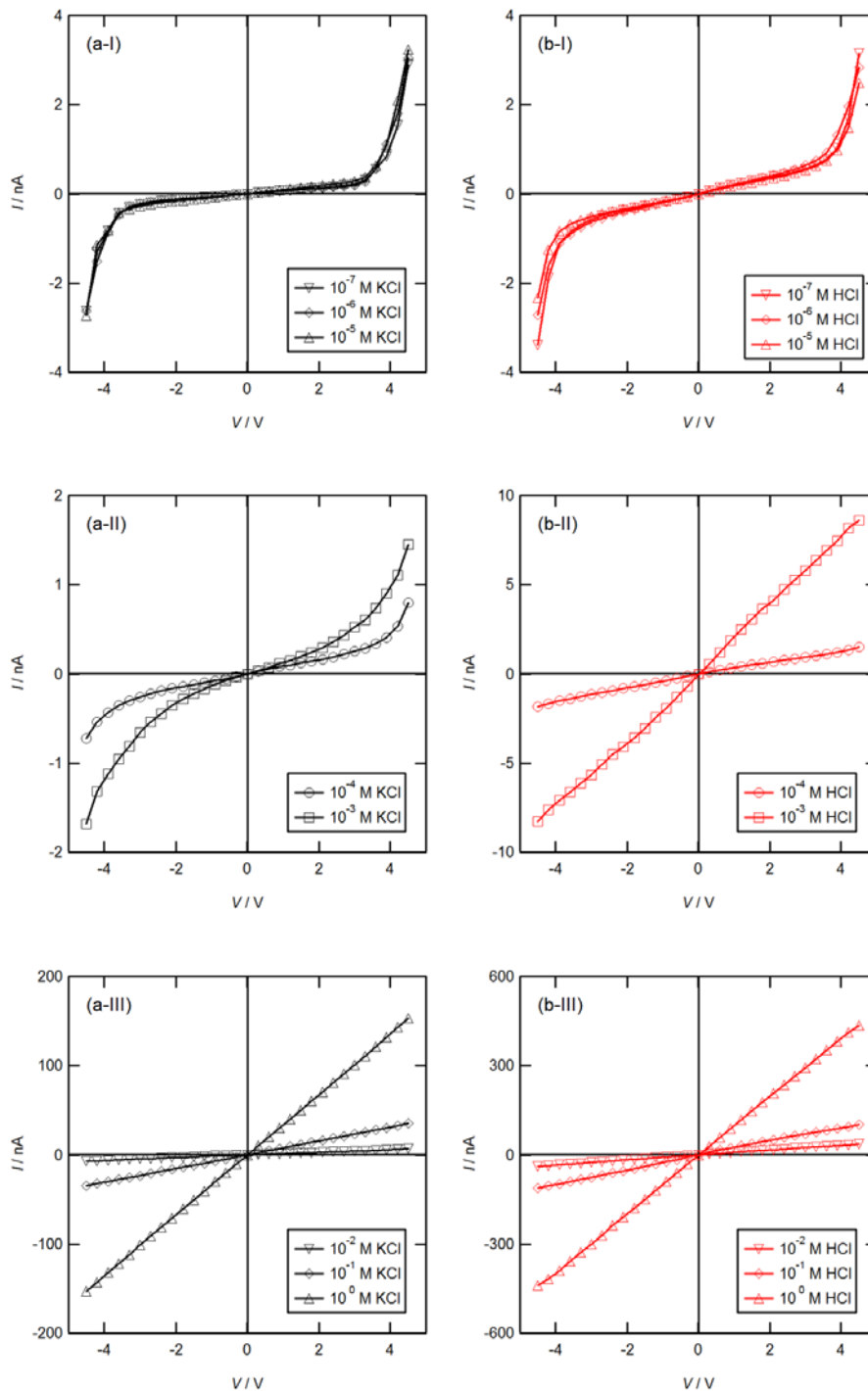


Figure 3.1 The measured current vs. electric potential bias ( $I$ - $V$ ) curves of (a) KCl and (b) HCl aqueous solutions at (I) low concentrations ( $10^{-7}$ ,  $10^{-6}$ , and  $10^{-5}$  M), (II) intermediate concentrations ( $10^{-4}$  and  $10^{-3}$  M), and (III) high concentrations ( $10^{-2}$ ,  $10^{-1}$ , and 1 M).

As explained in Chapter 2, in the case of KCl aqueous solutions, the  $I$ - $V$  curve was nonlinear below  $10^{-3}$  M (surface charge governed regime), because electric potential barriers are created in narrow cylindrical pore regions by surface charge and ink-bottle-like geometry of mesopores. On the other hand, the  $I$ - $V$  curve became linear above  $10^{-2}$  M (bulk concentration-governed regime), because electric potential barriers were absent owing to the cancelation of surface charge by counterions.

However, in the case of HCl aqueous solutions, the  $I$ - $V$  curves were nonlinear below  $10^{-5}$  M; in contrast, the  $I$ - $V$  curves were linear above  $10^{-4}$  M. The Debye lengths of the solutions at  $10^{-3}$  and  $10^{-4}$  M were 9.7 and 30.4 nm respectively; therefore at these concentrations, the lengths distinctly exceed the radii of the spherical cavities. This result suggests that the  $I$ - $V$  curves of HCl aqueous solutions were linear even in the surface charge governed regime.

Figure 3.2(b) shows the calculated  $K^+$  current density vs. the electric potential bias ( $J$ - $V$ ) curves with three different values of  $C_1$  and  $C_2$ . If  $C_1$  increases, i.e. the surface charge is better shielded, and  $C_2$  decreases, i.e. the diffusion due to ion concentration gradient is more strongly suppressed, the nonlinear behavior of  $J$ - $V$  curves becomes more obvious. The trend of the  $J$ - $V$  curves is quite similar to that of the measured measured current vs. electric potential bias ( $I$ - $V$ ) curves of KCl aqueous solutions at  $10^{-7}$ ,  $10^{-4}$ , and  $10^{-3}$  M concentrations as shown in Figure 3.2(a).

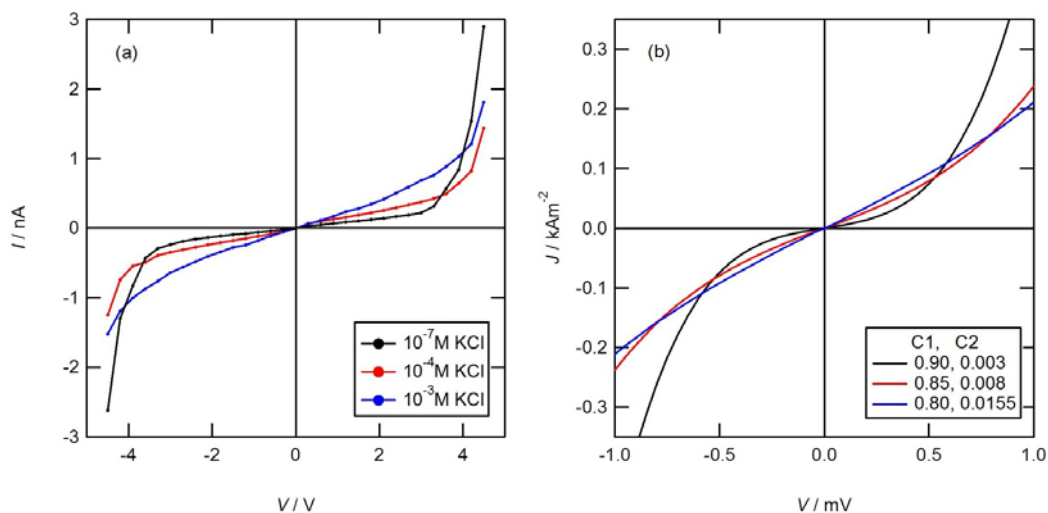


Figure 3.2 The measured current vs. electric potential bias ( $I$ - $V$ ) curves of (a) KCl aqueous solutions at  $10^{-7}$ ,  $10^{-4}$ , and  $10^{-3}$  M concentrations, and (b) calculated  $K^+$  current density vs. electric potential bias ( $J$ - $V$ ) curves.

In KCl aqueous solutions, the surface charge density should be independent of the ion concentrations in the bulk solutions. From the requirement of electroneutrality, ion concentration in the nanopores should be independent of that in the bulk. Therefore, surface charge density being equal at surface charged regime, ion concentrations inside the nanopore should be identical regardless of the bulk concentrations. The  $I$ - $V$  curves of Figure 3.2(a) were measured at surface charged regime, but the curvature of  $I$ - $V$  curves was different. The different nonlinear behavior of  $I$ - $V$  curves in surface charged regime can be attributed to change of condition such as the shielded surface charge and diffusion in nanopores due to bulk concentration change.

### 3.2.2 Effect of concentration on $I-t$ curves of HCl and KCl aqueous solutions

To better understand the characteristics of  $I-V$  curves, we analyzed the curves of current vs. time ( $I-t$ ) for KCl and HCl aqueous solutions. Figure 3.3(a) and 3.3(b) show the measured  $I-t$  curves of HCl aqueous solutions at  $10^{-5}$  and  $10^{-3}$  M. The time when a step potential  $V$  was applied to the electric circuit was defined as  $t = 0$  and  $I-t$  curves for seven selected step potentials,  $V = 0.3, 1.2, 2.4, 3.3, 3.9, 4.2$  and  $4.5$  V, were shown in Figure 3.3(a) and 3.3(b).

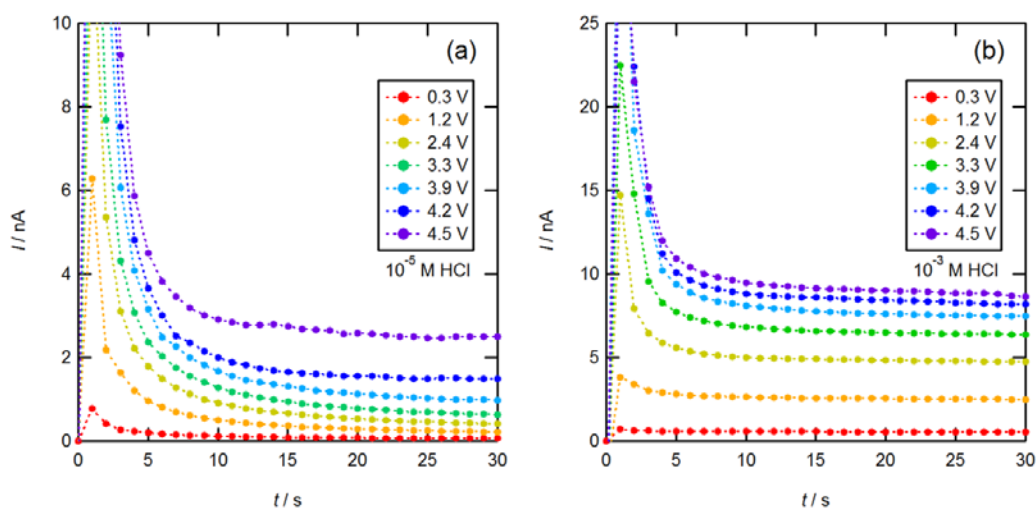


Figure 3.3 The measured ionic current vs. time ( $I-t$ ) curves of HCl aqueous solutions with concentrations of (a)  $10^{-5}$  M and (b)  $10^{-3}$  M.

The  $I-V$  curves shown in Figure 3.1 were obtained using the relaxation curve equilibrium values corresponding to each stepwise change in the applied voltage. Because the time to reach equilibrium depended on the kind of solutions and concentrations, the time interval of the applied voltage changed for each condition.

The relaxation rate of HCl aqueous solutions was about 5 times higher than that of KCl aqueous solutions with the same concentration, and in both solutions, the relaxation rate increased with increasing concentrations, which were attributed to the difference in diffusivity and the Debye length of the solutions, respectively [10].

The relaxation rate,  $k$ , for each step potential  $V$  was obtained by fitting the following equation to the  $I-t$  curve:

$$I(t) = I_0 + A \exp(-kt) \quad (3.1)$$

where,  $I_0$ ,  $A$ , and  $k$  were fitted parameters. The range of the curve-fitting was from about 5 to 30 s.

Figure 3.4 shows the calculated relaxation rate vs. step potential ( $k-V$ ) curves for HCl aqueous solutions at  $10^{-5}$  and  $10^{-3}$  M. At low concentration ( $10^{-5}$  M), the relaxation rate was almost constant about  $k = 0.2 \text{ s}^{-1}$  at low  $V$ , while it increased with respect to voltage at high  $V$ . The corresponding  $I-V$  curve exhibited the non-linear behavior, where the current increased exponentially with respect to voltage around  $V = 3.3 \text{ V}$ . These results suggest that with increasing  $V$  above 3.3 V,  $\text{H}^+$  can overcome the electric potential barriers created inside the thin film. In the equivalent electric circuit of a model demonstrated in Chapter 2, because  $\text{H}^+$  can transport smoothly without polarization, both a resistance and a capacitance inside the thin film decrease, and thus the relaxation rate increases. At middle concentration ( $10^{-3}$  M), the relaxation rate was almost constant about  $k = 0.2 \text{ s}^{-1}$  in the entire region of  $V$  and the corresponding  $I-V$  curve exhibited the linear

behavior. In Figure 3.4, the red line is curve fitting line to describe the tendency of the relaxation rate measured with increasing  $V$ , even though it does not correspond perfectly with those data measured.

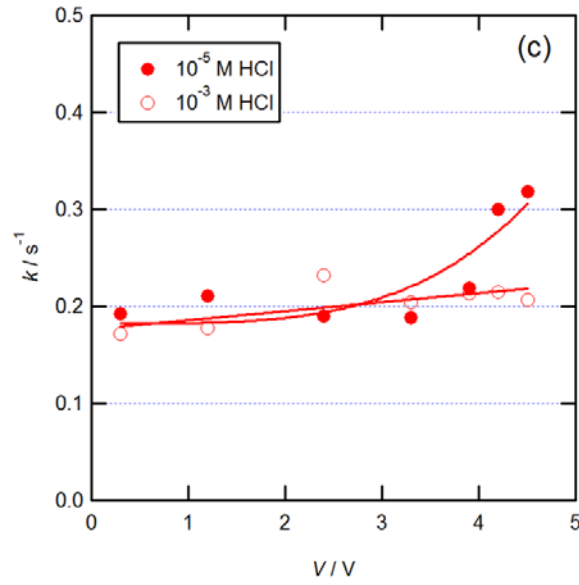


Figure 3.4 Calculated relaxation rate vs. step potential ( $k$ - $V$ ) curves.

Figures 3.5(a) and 3.5(b) show the measured  $I$ - $t$  curves of KCl and HCl aqueous solutions at  $10^{-4}$  and  $10^{-3}$  M. From Eq. (2.1), the  $I_0$ - $V$  and  $I_\infty$ - $V$  curves are

$$\text{given by } I_0 = \frac{(r/R) + (1 - V_{-1}/V)}{(r/R) + 1} \left( \frac{V}{r} \right) \text{ and } I_\infty = \frac{(r/R)}{(r/R) + 1} \left( \frac{V}{r} \right), \text{ respectively, where}$$

$I_0$  is the current at  $t = 0$  and  $I_\infty$  is the current at  $t = \infty$ . The dotted curves in Figures 3.5(a) and 3.5(b) show the  $I_0$ - $V$  curves. When the  $I$ - $V$  curve was linear, the corresponding  $I_0$ - $V$  curve was also linear, except in the case of the  $10^{-4}$  M HCl aqueous solution, since this concentration could correspond to the transient regime between linear and nonlinear regimes for HCl aqueous solutions.

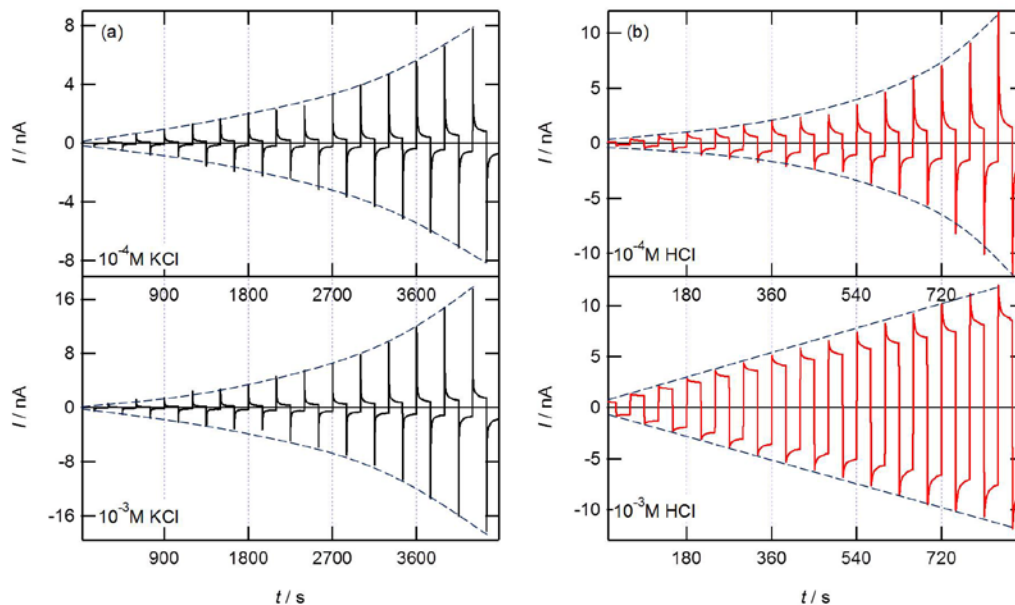


Figure 3.5 The measured ionic current vs. time ( $I-t$ ) curves of (a) KCl and (b) HCl aqueous solutions with concentrations of  $10^{-4}$  and  $10^{-3}$  M.

### 3.2.3 Comparative analysis of $G-n$ curves of HCl and KCl aqueous solutions

To better understand the characteristics of ion and proton transport in SBA-16 thin films with 3D cubic structures, we compared the conductance of KCl and HCl aqueous solutions within concentrations ranging from  $10^{-7}$  to 1 M. Figure 3.6(a) and 3.6(b) show the measured and calculated conductance vs. concentrations ( $G-n$ ) curves of KCl and HCl aqueous solutions, respectively. The measured conductance was obtained from the gradient of  $I$  with respect to  $V$  from 0 to 1.5 V for nonlinear  $I-V$  curves and from 0 to 4.5 V for linear  $I-V$  curves.

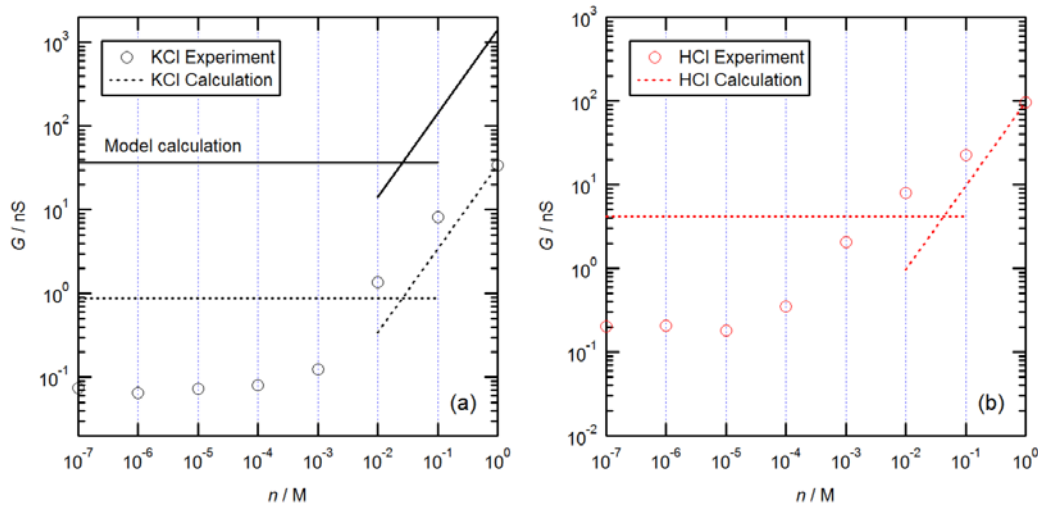


Figure 3.6 Comparisons between the measured and calculated conductance vs. concentration ( $G-n$ ) curves of (a) KCl and (b) HCl aqueous solutions.

Figure 3.6(a) also shows the  $G-n$  curve of model calculations from ion transport work explained in Chapter 2. Briefly, at high concentrations (bulk concentration governed regime), the conductance was calculated by assuming that the model pore was filled with bulk solution.

On the other hand, at low concentrations (surface charge-governed regime), the conductance was calculated by assuming that the model pore with a fixed surface charge density was filled with a unipolar solution of counterions, the concentration of which was determined from the requirement of electroneutrality to the surface charge of the model pore.

The calculated  $G-n$  curve of KCl aqueous solutions was obtained by shifting the  $G-n$  curve of model calculation downward, as the curve passed through the point of measured conductance at 1 M. The calculated  $G-n$  curve of HCl aqueous

solutions was obtained from that of KCl aqueous solutions. It was assumed that the difference in conductance between KCl and HCl aqueous solutions was due to the difference between the diffusivities of  $K^+$  and  $H^+$  only. Here, the diffusivities of  $K^+$ ,  $H^+$ , and  $Cl^-$  in water were assumed to be  $D_{K^+} = 1.96 \times 10^{-9}$ ,  $D_{H^+} = 9.31 \times 10^{-9}$ , and  $D_{Cl^-} = 2.03 \times 10^{-9} \text{ m}^2 \text{ s}^{-1}$ , respectively. The conductance of HCl aqueous solutions was 4.75 ( $= 9.31/1.96$ ) times larger than that of KCl aqueous solution in the surface charge-governed regime and 2.84 ( $= (9.31 + 2.03)/(1.96 + 2.03)$ ) times larger than that of KCl aqueous solution in the bulk concentration-governed regime, as illustrated in Figure 3.6(b).

The measured  $G$ - $n$  curve of KCl aqueous solutions was larger than the calculated one in the bulk concentration-governed regime. SBA-16 thin films have pores measuring a few nanometers in diameter and the Debye length of solutions at  $10^{-2}$  and  $10^{-1}$  M concentrations are 3.0 and 0.97 nm, respectively. Thus, the electrical double layer still occupies a substantial proportion of the total cross sectional area of the pore. It was reported that the surface charge-governed regime expands above  $10^{-1}$  M in 2 nm nanochannels [12]. Therefore, the measured conductance was larger than the calculated one.

On the other hand, in the surface charge-governed regime, the measured  $G$ - $n$  curve was considerably smaller than the calculated one. The main reason for this difference is the nonlinearity of  $I$ - $V$  curves; the  $I$ - $V$  curves of KCl aqueous solutions became nonlinear below  $10^{-3}$  M, and so the conductance decreased sharply between  $10^{-2}$  and  $10^{-3}$  M [10].

The measured and calculated  $G$ - $n$  curves of HCl aqueous solutions did not agree with each other in the entire concentration range. At low concentrations ( $10^{-7}$ – $10^{-5}$  M), it can be inferred that the measured  $G$ - $n$  curve is considerably smaller than the calculated one because of the nonlinearity of  $I$ - $V$  curves. At intermediate concentrations ( $10^{-4}$  and  $10^{-3}$  M), the measured conductance of HCl aqueous solutions increased appreciably as the concentration increased. In the case of proton transport in mesoporous silica SBA-15 containing 7–8 nm diameter cylindrical pores, it was reported that as the concentration of HCl aqueous solutions increased, the silanol groups protonated and the surface charge density decreased, resulting in the decrease in conductance within the surface charge-governed regime [11]. This trend can also be reproduced by a continuum dynamics simulation using a model pore of which surface charge density decreases with increasing the bulk concentration [12].

In contrast, in the case of proton transport in mesoporous silica SBA-16 with ink-bottle-like pore structures, in the same regime, the conductance increased monotonically with increasing the concentration of HCl aqueous solutions. This trend cannot be reproduced by the same continuum dynamics simulation even if a unique pore structure is considered. If the surface charge density decreases, two different effects will appear: (1) the height of electric potential barriers in mesopores reduced, leading to linear  $I$ - $V$  curves, and (2) the density of  $H^+$  in mesopores decreased owing to the requirement of electroneutrality, leading to the suppression in conductance. Thus, the  $I$ - $V$  curves should gradually become linear,

and the conductance should decrease as the concentration increases. Details were well described in Chapter 3.3.

However, the measured  $G-n$  curve of HCl aqueous solutions showed that the conductance increases as the concentration increases. To explain this trend, the following scenario could be considered: The effective surface charge density to create electric potential barriers was reduced, but the real surface charge density that determines the density of  $H^+$  was not reduced appreciably, because some of the dissociated  $H^+$  and  $SiO^-$  were very close to each other.  $H^+$  located close to  $SiO^-$  sites also became charge carriers and might transport by hopping between  $SiO^-$  sites. The electric potential barrier was therefore lowered, but the density of  $H^+$  did not decrease appreciably, thus increasing the conductance.

The proton transport in water or aqueous solutions confined in nanopores and nanochannels needs to be investigated. Furthermore, the precise control of surface charge density of mesoporous silica is yet to be challenged. This study, however, highlights the difference between proton transport and  $K^+$  transport, and elucidates that the primary difference in  $I-V$  curves appear at intermediate concentrations ( $10^{-4}$  and  $10^{-3}$  M) in the surface charge-governed regime.

### **3.3 Calculation method of 1D PNP equations and $J_{H^+} - V$ curves**

In order to calculate  $J_{H^+} - V$  curves in the surface charge governed regime, we assumed that the negatively charged pore was filled with a unipolar solution of  $H^+$  (including only positive charge carriers) and the system was 1D. In practice, ion

transport on this scale should be analyzed using stochastic dynamics or molecular dynamics simulations because the multiple interplays between different types of intermolecular interactions characterize the transport. However, in this Chapter, in order to discuss tendency associated with conductance in the surface charge governed regime when the electric potential barrier and proton concentrations increase due to the deprotonation reaction, we intended to use continuum dynamics simulations. Details relevant to calculation method were described in Chapter 2.7. The governing equations were the Poisson-Nernst-Planck equations:

$$\frac{d^2V}{dz^2} = -\frac{1}{\varepsilon_0\varepsilon} (n_{\text{H}^+}e + \rho_e) \quad (3.2)$$

$$\frac{dJ_{\text{H}^+}}{dz} = 0 \quad , \quad (3.3)$$

where

$$J_{\text{H}^+} = -eD_{\text{H}^+} \left[ \left( \frac{dn_{\text{H}^+}}{dz} \right) + \frac{n_{\text{H}^+}e}{kT} \left( \frac{dV}{dz} \right) \right] . \quad (3.4)$$

Here,  $J_{\text{H}^+}$ ,  $D_{\text{H}^+}$ , and  $n_{\text{H}^+}$ , are the current density, diffusion coefficient, and number density of proton, respectively.  $V$  is the electric potential,  $\varepsilon_0$  is the permittivity of vacuum,  $\varepsilon$  is the dielectric constant of water,  $e$  is the elementary charge,  $\rho_e$  is the charge density equivalent to the surface charge,  $k$  is the Boltzmann constant, and  $T$  is the absolute temperature.  $\rho_e$  is given by

$$\rho_e(z) = \bar{\rho}_e + \tilde{\rho}_e(z), \quad (3.5)$$

where  $\bar{\rho}_e$  is the average component and  $\tilde{\rho}_e$  is the variation component.  $\rho_e$  was determined by the following procedure. First, the calculated electric potential inside a 3D model pore was simplified as follows:

$$V(z) = V_0 \cos(2\pi z/L), \quad (3.6)$$

where  $V_0$  is the amplitude of the electric potential and  $L$  is the unit length of the model pore. The equivalent charge density,  $\tilde{\rho}_e$ , required to determine the above electric potential,  $V(z)$ , was given by

$$\tilde{\rho}_e(z) = \rho_{e0} \cos(2\pi z/L), \quad (3.7)$$

where  $\rho_{e0} = \varepsilon_0 \varepsilon V_0 (2\pi/L)^2$ . The average charge density,  $\bar{\rho}_e$ , was given by  $\bar{\rho}_e = -\rho_{e0}$ . Here,  $D_{H^+} = 9.31 \times 10^{-9} \text{ m}^2 \text{ s}^{-1}$ ,  $L = 12 \text{ nm}$ ,  $T = 300 \text{ K}$ , and  $\varepsilon = 80$ . In the calculation of the electric potential inside a 3D model pore,<sup>1</sup> when the surface charge density  $\sigma$  was assumed to be  $-10^{-2} \text{ C m}^{-2}$ , the electric potential inside the model pore was simplified to Eq. (3.6), where  $V_0 = 30 \text{ mV}$ . In this calculation condition, the  $\bar{\rho}_e = 5.82 \times 10^6 \text{ C m}^{-3}$ ; i.e., the average proton density  $\bar{n}_{H^+}$  was 60 mM. Because the electric field inside the 3D model pore is proportional to  $\sigma$ ,  $V_0$  should also be proportional to  $\sigma$ . Furthermore, because  $\bar{\rho}_e = -\varepsilon_0 \varepsilon V_0 (2\pi/L)^2$ ,  $\bar{n}_{H^+}$  is proportional to  $V_0$ .

Figure 3.7(a) shows the calculated  $J_{\text{H}^+} - V$  curves for five different values of  $V_0$ : 6, 15, 30, 60, and 150 mV. The corresponding  $\bar{n}_{\text{H}^+}$  were 12, 30, 60, 120, and 300 mM, respectively.

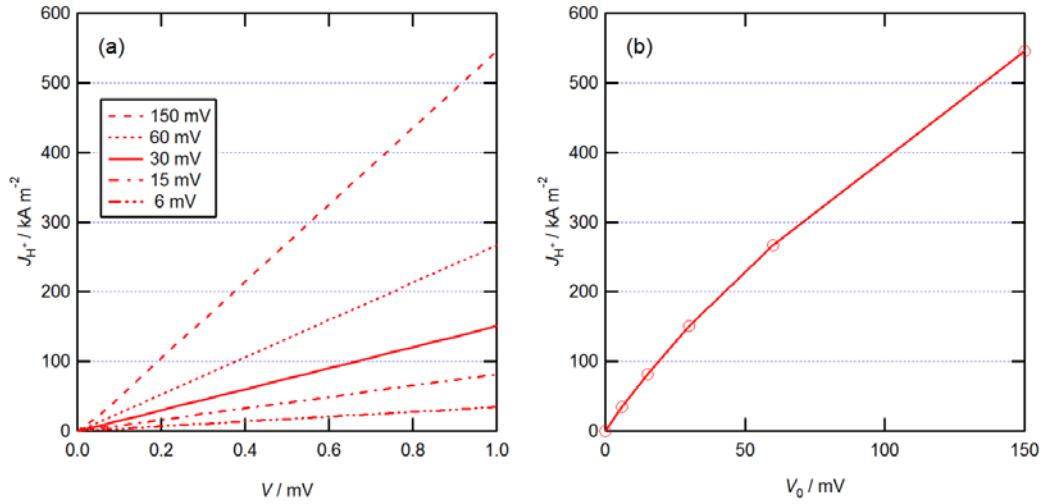


Figure 3.7 (a) Calculated  $J_{\text{H}^+} - V$  curves for five different values of  $V_0$ , 6, 15, 30, 60, and 150 mV, and (b)  $J_{\text{H}^+}$  at  $V = 1.0$  mV as a function of  $V_0$ .

The calculated  $J_{\text{H}^+} - V$  curves were almost linear. Figure 3.7(b) shows the calculated  $J_{\text{H}^+}$  at  $V = 1.0$  mV as a function of  $V_0$ . The calculated  $J_{\text{H}^+} \Big|_{V=1.0\text{mV}}$  increased monotonically with increasing  $V_0$  although the gradient of  $J_{\text{H}^+} \Big|_{V=1.0\text{mV}}$  with respect to  $V_0$  decreased gradually with increasing  $V_0$ . These calculation results suggest that if silanol groups are deprotonated and  $|\sigma|$  increases, both average proton density  $\bar{n}_{\text{H}^+}$  and the potential barrier height  $V_0$  increase, resulting in an increase in proton current density  $J_{\text{H}^+}$ . In this model, the conductance

should increase with decreasing concentration of HCl aqueous solutions in the surface charge governed regime.

### 3.4 Restoration of electric potential barriers by deprotonation reaction

To elucidate the effect of surface charge density of mesopores on  $I-V$  curves, the  $I-V$  curves were measured by changing the soaking duration of a nanofluidic device in deionized (DI) water (18.2 M $\Omega$ ·cm). Figure 3.8 shows the measured  $I-V$  curves for four different soaking durations.

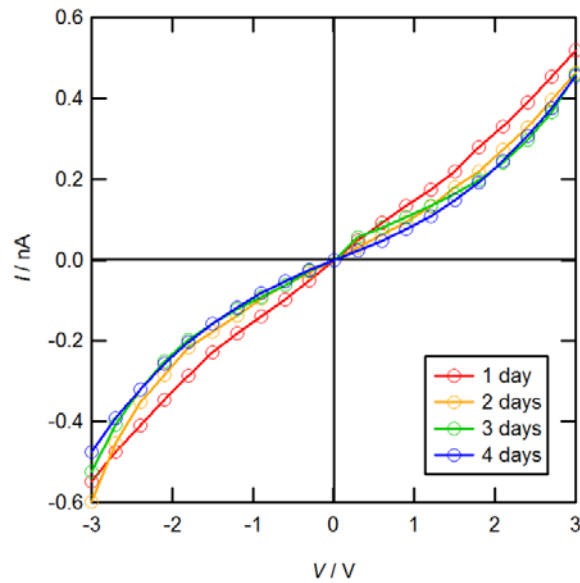


Figure 3.8 Effect of soaking duration of a nanofluidic device in DI water on current vs. electric potential bias ( $I-V$ ) curves.

Following the measurement of the  $I-V$  curve of 1 M HCl aqueous solution, a nanofluidic device was immersed in DI water for several days to restore silanol

groups in the pore surface. The  $I$ - $V$  curve of  $10^{-7}$  M HCl aqueous solution was measured every 24 h. Despite the extremely low concentration, the measured  $I$ - $V$  curve was almost linear at 1 day, since the silanol groups were not yet fully restored from the previous protonation.

Eventually, however, the measured  $I$ - $V$  curve became nonlinear because the silanol groups were restored by deprotonation, and the electric potential barriers increased. After 4 days, the silanol groups were fully restored and the  $I$ - $V$  curve agreed with the measured one. These results suggest that the  $I$ - $V$  curve of HCl aqueous solutions was sensitive to the surface state of mesopores, and control of the surface state was crucial to elucidate the characteristics of  $I$ - $V$  curves.

### **3.5 Conclusion**

In this chapter, mesoporous silica SBA-16 thin films with highly ordered 3D cubic structures were synthesized by evaporation-induced self assembly method via dip coating, to investigate proton transport of aqueous solutions confined in mesopores. Using electrochemical measurements of current under DC electric fields, we elucidated proton transport phenomena through mesopores of SBA-16 thin films. The measured  $I$ - $V$  curves of KCl aqueous solutions were linear above  $10^{-2}$  M, while those of HCl aqueous solutions were linear above  $10^{-4}$  M. It was concluded that the concentration range of linear  $I$ - $V$  curves in HCl aqueous solutions was wider than that in KCl aqueous solutions, and the linear  $I$ - $V$  curves and high proton conductance were measured in the surface charge-governed

regime only for HCl aqueous solutions. The precise mechanism of proton transport in silica mesopores in this regime has not been clarified, but the surface charge density of mesopores can be controlled on the basis of the pH of the solutions, which affects both of the electric field and the carrier density in mesopores, and results in linear  $I$ - $V$  curves and high proton conductance. Such characteristic may be applied in the development of nanopores, such as artificial ion channels and polymer electrolyte membranes with complex structures, for smooth proton transport, and could be useful to design 1 nm order structures for sensor, fuel cell and desalination technologies.

### 3.6 Reference

1. Williams, R. Proton Circuits in Biological Energy Interconversions. *Annu. Rev. Biophys. Biophys. Chem.* **1988**, *17*, 71-97.
2. Elston, T.; Wang, H.; Oster, G. Energy Transduction in ATP Synthase. *Nature* **1998**, *391*, 510-513.
3. Wang, C. Fundamental Models for Fuel Cell Engineering. *Chem. Rev.* **2004**, *104*, 4727-4766.
4. Kreuer, K.; Paddison, S.; Spohr, E.; Schuster, M. Transport in Proton Conductions for Fuel-Cell Application: Simulation, Elementary Reactions, and Phenomenology. *Chem. Rev.* **2004**, *104*, 4637-4678.
5. Iwahara, H. Technological Challenges in the Application of Proton Conducting Ceramics. *Solid State Ionics* **1995**, *77*, 289-298.
6. Hille, B. *Ion Channels of Excitable Membranes*, 3rd ed.; Sinauer Associates Inc.: Sunderland, MA, 2001.
7. Schultz, T.; Zhou, S.; Sundmacher, S. Current Status of and Recent Developments in the Direct Methanol Fuel Cell. *Chem. Eng. Techno* **2001**, *24*, 1223-1233.
8. Seger, B.; Vinodgopal, K.; Kamat, P. Proton Activity in Nafion Films: Probing Exchangeable Protons with Methylene Blue. *Langmuir* **2007**, *23*, 5471-5476.
9. Y.; Kaneda, M.; Terasaki, O.; Zhao, D.; Kim, J. M.; Stucky, G.; Shin, H. J.; Ryoo, R. Direct imaging of the pores and cages of three-dimensional mesoporous materials. *Nature* **408**, *408*, 449-453.
10. Daiguji, H.; Hwang, J.; Takahashi, A.; Kataoka, S.; Endo, A. Ion Transport in Mesoporous Silica SBA-16 Thin Films with 3D Cubic Structures. *Langmuir* **2012**, *28* (7), 3671-3677.
11. Fan, R.; Huh, S.; Yan, R.; Arnold, J.; Yang, P. Gated Proton Transport in Aligned Mesoporous Silica Films. *Nat. Mater.* **2008**, *7*, 303-307.
12. Duan, C.; Majumdar, A. Anomalous Ion Transport in 2-nm Hydrophilic Nanochannels. *Nat. Nanotech.* **2010**, *5*, 848-852.



# CHAPTER 4

## Thickness and Hexagonal Pore–Array Dimensions of SBA-15 Thin Film

*In this chapter, two-dimensional hexagonal mesoporous silica thin films of SBA-15 were synthesized via dip-coating using an evaporation-induced self-assembly process. The effect of the withdrawal speed on the thickness of the films, one-dimensional pore alignments and two-dimensional hexagonal pore arrays was elucidated. The film thickness increases with increasing withdrawal speed and also increases upon decreasing the withdrawal speed to ultraslow region where capillary rise of the solution occurs. Detailed analyses of FE-SEM and TEM images and XRD and XRR patterns of the synthesized thin films clarified that the pore sizes and interplanar spacing also depend on the withdrawal speed.*

### 4.1 Introduction

Micelle-templated mesoporous silica materials have attracted considerable interest in a variety of practical fields, including catalysis, optics, electronics, biotechnology, and separation, owing to their highly ordered and uniform pore size, high surface area to volume ratio, and simple synthesis (i.e., the liquid crystal templating mechanism) [1-3]. Precise control of the properties of mesoporous silica, such as pore size and structure, is important for their practical application and is attained by adjusting the surfactant that acts as an organic template [4-9].

In particular, mesoporous silica materials with two-dimensional hexagonal arrays have attracted significant attention owing to the simplicity of their geometry and the ease of analysis of the pore structure. These mesoporous silica materials can be synthesized using amphiphilic triblock copolymer surfactants and have a highly ordered two-dimensional hexagonal structure (space group  $P6mm$ ) with uniform pore sizes ranging from 50 to 300 Å [5]. Furthermore, it has been reported that the morphology of these materials can be controlled by varying the surfactants and silica sources [10]. Nanostructured films such as SBA-15 thin films with highly ordered mesoporous structures are potentially applicable for use in optoelectronic devices, membrane-based separations, nanofluidic systems, sensors/actuator arrays, and for the fabrication of nanowires [11-15]. These SBA-15 thin films are fabricated using the dip-coating method because of the increased ability to align the pores parallel to the substrate in the desired direction as compared to spin-coating [16]. Using the dip-coating process, a well-ordered mesostructured thin film can be deposited onto the substrate by evaporation-induced self-assembly [17-19].

It was reported that the thickness of thin films deposited by employing the moving solid substrates can increase or decrease with variation of withdrawal speed and can be divided into two main regimes: i) at high speed, viscous drag forces interacting with substrates has a predominant role in depositing thin films and the liquid films dragged onto the substrate dry shortly after the motion of the substrate was stopped (Landau-Levich regime). The thickness of liquid thin film

formed in this regime increases with increasing the withdrawal speed at the power of  $2/3$  [20]. ii) at low speed enough to neglect viscous drag force, solutes accumulate near the contact line of the solution and substrate due to evaporation-induced flow, depositing the dried film above the meniscus (Evaporation regime) [21]. This deposition process is similar to the phenomena known as the “coffee-ring-effect” caused by the nonuniform evaporation flux at surface of drying droplets [22,23]. The theoretical and experimental research in Landau-Levich regime has been investigated for several decades while few studies concerning evaporation regime under the moving substrate was conducted until a recent date. Faustini et al. experimentally showed that for sol-gel film formation by dip-coating, the thickness deposited in evaporation regime increases upon decreasing the withdrawal speed and there is a minimum value at critical speed,  $V_{crit}$ , for which the capillarity rise effect counterbalances the viscous drag [24]. Berteloot et al. also proposed a simple model which can predict the thickness in evaporation regime and the thickness based on the proposed model is proportional to the inverse of the square of withdrawal speed [25]. However, although both thin film formation processes were completely different as mentioned above, it never took into account the fact that the structure of dried films deposited in each process regime can be influenced by a multiplicity of several factors such as evaporation rate, surface tension gradient, and viscosity variation. In reality, each evaporation rate measured at different place of liquid droplet surface depends on the contact angle between the solid substrate and

liquid [26,27]. If the contact angle is  $90^\circ$ , the evaporation rate is uniform across the entire surface. In contrary, in the case of lower contact angle, the evaporative flux is enhanced at the droplet edge. In evaporation regime, the drying film is formed at an edge to the film and the presence of the edge complicates the boundary condition, and the structure of dried films affects the evaporation rate.

In SBA-15 mesoporous silica thin films with two-dimensional hexagonal pore structures, the uniaxially oriented alignment, interplanar spacing, and pore size are important to improve the performance of various devices with mesoporous structures. Therefore, in conjunction with a constant withdrawal speed, a variety of techniques, e.g., using a substrate with lithographically designed confined nanospaces [28-30], photoinduced anisotropic polymer orientation processes [31], and electrically [32] or magnetically [33] induced orientation, have been reported for the fabrication of two-dimensional hexagonal mesoporous thin films with the desired mesochannels. The sizes of the mesopores can be varied by employing surfactants with different poly(alkylene oxide) triblock copolymers and by the addition of cosolvent organic molecules [5]. To control the thickness of the films, the organic/inorganic precursor solutions can be either diluted or concentrated and the deposition time can be adjusted [34]. However, few studies have reported the simultaneous control of film thickness and pore alignment of two-dimensional hexagonal mesoporous silica thin films by tuning the withdrawal speed during dip-coating.

In this chapter, we focus on the effect of withdrawal speeds ranging from 0.02 to 3.0 mm s<sup>-1</sup> on the thickness and pore array of SBA-15 mesoporous silica thin films with two-dimensional hexagonal pore structures. The film thickness, pore size, and pore structures were investigated via field-emission scanning electron microscopy (FE-SEM) and transmission electron microscopy (TEM) and X-ray diffraction (XRD) and X-ray reflectivity (XRR) analysis of the synthesized thin films. Furthermore, we discuss the pore alignment mechanism and the potential for controlling the film thickness and hexagonal pore-array dimensions of SBA-15 mesoporous silica thin films with nanometer precision.

## **4.2 Preparation of SBA-15 mesoporous silica thin films**

Si substrates underwent sequential 10 min cleanings with n-hexane, acetone, and pure water in an ultrasonic bath. The substrates were then soaked in piranha solution for 30 min and rinsed with pure water to remove contaminants and make them wettable with a water/ethanol solution. They were then cleaned with 2-propanol for 1 h and dried in air. The precursor solution was prepared as follows: Tetraethyl orthosilicate (TEOS; 1.50 g) as the silica source, EtOH (15.0 g), pure water (0.78 g), and 0.1 M HCl (0.15 g) were stirred at room temperature for 1 h in a capped vial. Triblock copolymer Pluronic P123 (0.30 g) as the structure-directing agent and EtOH (14.25 g) were stirred at room temperature for 1 h in a separate capped vial. After stirring, the two different solutions were mixed and then stirred at room temperature for 1 h.

The final TEOS/P123/EtOH/H<sub>2</sub>O/0.1 M HCl molar ratio of the precursor solution was 1:0.0072:88.2:7.17:0.0021. We referred to the SBA-15 thin film fabrication procedures reported by Fan et al. [11]

The prepared precursor solution was then deposited on a Si substrate using the dip-coating method, as follows: The cleaned Si substrate was vertically immersed in the precursor solution and withdrawn at a rate of 0.02, 0.05, 0.1, 0.2, 0.5, 1.0, or 3.0 mm s<sup>-1</sup> then aged for 24 h. The coating processes were performed at 298 K at a relative humidity (RH) of 60% inside a glove box. Subsequently, the as-prepared thin films were dried at 343 K for 1 h and calcined to remove the block copolymer surfactant at 773 K for 5 h in air with a very slow ramping rate (<0.5 K min<sup>-1</sup>) to minimize the deformation caused by thermal stress.

### **4.3 Characterization of SBA-15 mesoporous silica thin films**

The synthesized transparent mesoporous silica thin films were observed using a field-emission scanning electron microscope (S-4800, Hitachi High-Technologies, Japan) at an accelerating voltage of 1.0–1.2 kV without any metal coating. Furthermore, TEM images of cross-sections of the film were obtained using a transmission electron microscope (H-9000UHR, Hitachi High-Technologies, Japan) at an acceleration voltage of 300 kV. Prior to the TEM analysis, the specimen was prepared using the ion-beam milling method with a GATAN 691 PIPS at an acceleration voltage of 6 kV; an Ar ion beam was used and the milling angle was 5° (See APPENDIX A associated with TEM specimen preparation).

The average film thickness and hexagonal pore-array dimensions of the SBA-15 thin films were analyzed using an X-ray reflectivity (XRR) and X-ray diffraction system (XRD) (SmartLab 9 kW system, RIGAKU, Japan) with Cu K $\alpha$  radiation (wavelength = 1.54 Å) and 45 kV/200 mA. GlobalFit software was used to analyze the XRR data.

### 4.3.1 FE-SEM and TEM measurements

Figure 4.1 shows cross-sectional FE-SEM and TEM images of SBA-15 thin films synthesized on Si substrates at four different withdrawal speeds: 0.02, 0.5, 1.0, and 3.0 mm s<sup>-1</sup>.

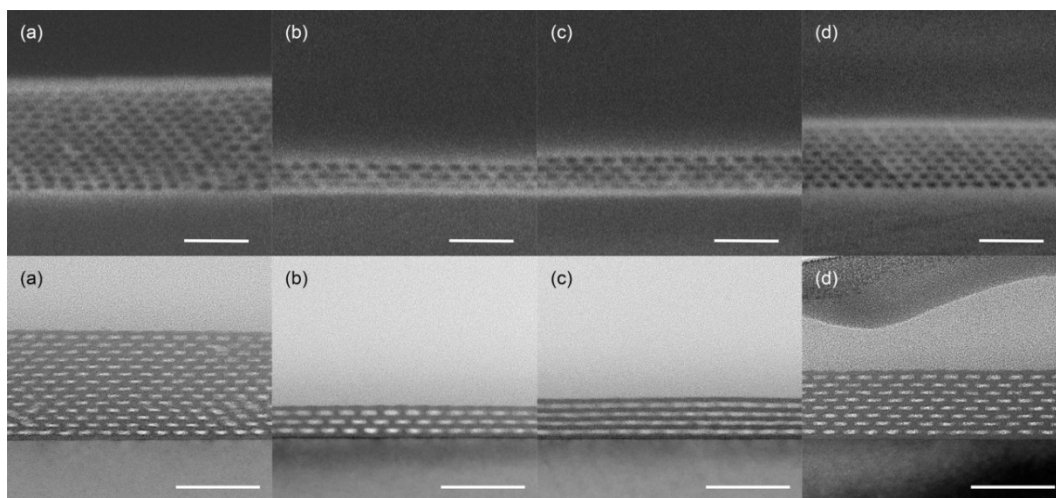


Figure 4.1 Cross-sectional FE-SEM (top) and TEM (bottom) images of SBA-15 thin films synthesized on Si substrates at four different withdrawal speeds: (a) 0.02, (b) 0.5, (c) 1.0, and (d) 3.0 mm s<sup>-1</sup>. The scale bar is 50 nm.

FE-SEM images show the surface of a cross-section; therefore, it cannot be used to determine if the pore structures along the dip-coating direction behind a

cross-sectional image are the same as those on the surface. In contrast, TEM images show a projection of the interior of a specimen; thus, the alignment of the pores in the thin film along the dip-coating direction can be verified. Accordingly, FE-SEM and TEM analyses are complementary and enable the detailed characterization of the interior structure of thin films. The TEM measurements analyzed the SBA-15 thin film specimens to a depth of a few hundred nanometers.

Although the film thickness determined via TEM is slightly smaller than that via FE-SEM, the number of pores normal to the Si surface is similar in both the TEM and FE-SEM images. As the withdrawal speed increased from 0.5 to 3.0  $\text{mm s}^{-1}$ , the film thickness increased; similarly, as the withdrawal speed decreased to 0.02  $\text{mm s}^{-1}$ , the film thickness also increased. The average film thicknesses measured by analyzing FE-SEM images of the thin films produced at withdrawal speeds of 0.02, 0.5, 1.0, and 3.0  $\text{mm s}^{-1}$  were 81.6, 23.7, 28.9, and 51.3 nm, respectively.

The FE-SEM images revealed that the pore arrays contained regularly arrayed pores with two-dimensional hexagonal structures at withdrawal speeds of 0.5, 1.0, and 3.0  $\text{mm s}^{-1}$ ; this was not the case for films produced at a withdrawal speed of 0.02  $\text{mm s}^{-1}$ . However, as shown in the TEM images, these thin films do have well-controlled two-dimensional hexagonal pore structures, which suggests that the thin film produced at a 0.02  $\text{mm s}^{-1}$  withdrawal speed has two-dimensional hexagonal pore array but lacks the perfect pore array seen at withdrawal speeds of 0.5, 1.0, and 3.0  $\text{mm s}^{-1}$ . Furthermore, in the TEM images of the thin film

produced with a withdrawal speed of  $1.0 \text{ mm s}^{-1}$ , the pores were located in the same interval normal to the substrate. However, each pore (i.e., the white regions in Figure 4.1(c)) was not independent but rather was connected to an adjacent pore; this supports that the local two-dimensional hexagonal pore array were well controlled, although the directions of the pore array varied at some plane within a few hundred nanometers deep in the specimens and the pores were not perfectly aligned in one direction over the entire film. In the case of withdrawal speeds of  $0.02, 0.5 \text{ mm s}^{-1}$ , 1D alignment of the pores estimated from TEM images (Figure 4.1(a) and 4.1(b)) seems to be well aligned compared to that of  $1.0 \text{ mm s}^{-1}$ , but in comparison with  $3.0 \text{ mm s}^{-1}$  for a larger area, the degree of alignment was not that good. Figure 4.2 shows TEM image viewed in wider space at four withdrawal speeds: (a)  $0.02$ , (b)  $0.5$ , (c)  $1.0$ , and (d)  $3.0 \text{ mm s}^{-1}$ .

In both the FE-SEM and energy-filtered TEM images, the interplanar spacing of the (100) planes [ $d(100)$ ], i.e., the distance between two adjacent planes normal to the Si surface where the mesopores are located, decreased with increasing film thickness. The average  $d(100)$  values measured from the FE-SEM images were  $6.3, 7.9, 7.2,$  and  $6.4 \text{ nm}$  for withdrawal speeds of  $0.02, 0.5, 1.0,$  and  $3.0 \text{ mm s}^{-1}$ , respectively. Furthermore, the sizes of the pores (i.e., the black and white areas in the FE-SEM and TEM images in Figure 4.1, respectively) also decreased with increasing film thickness. The detail is explained later on. The image analysis showed that as the film thickness increases, the both the interplanar spacing and pore size decrease, yielding more compact structures.

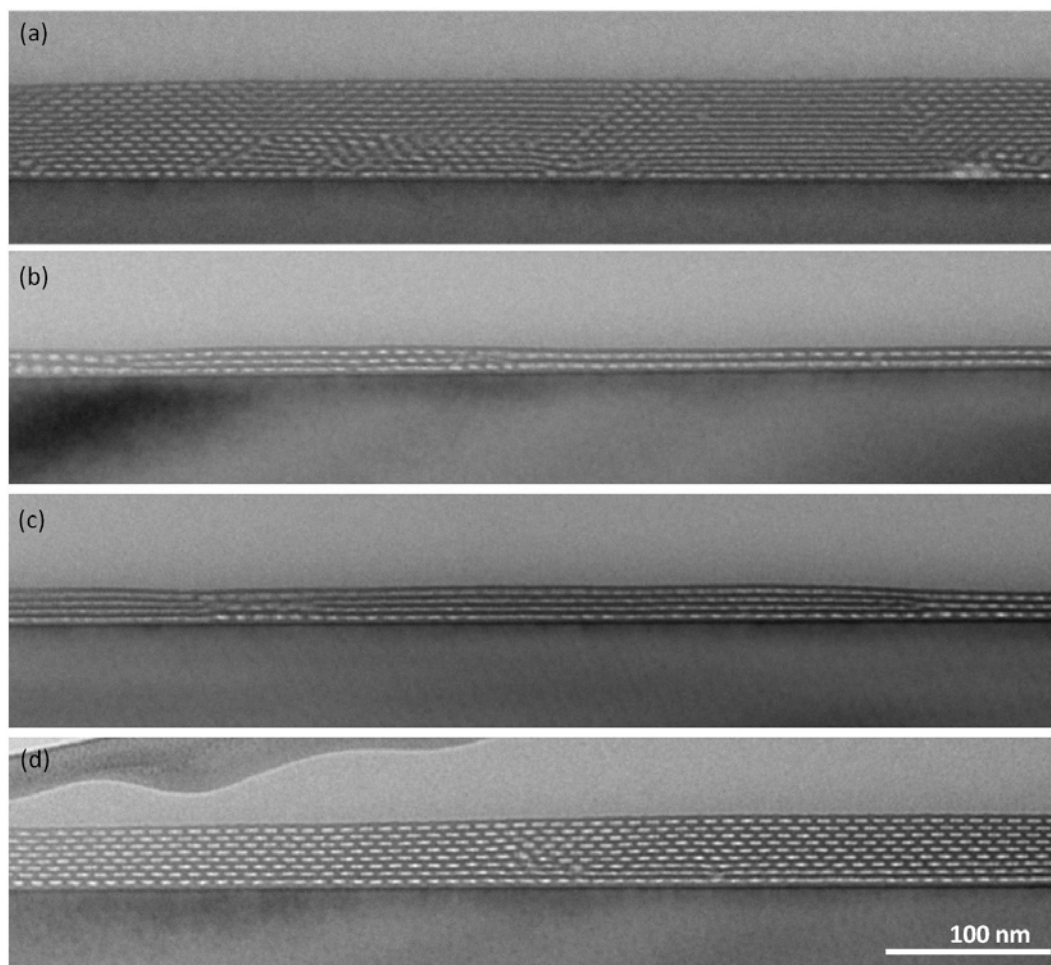


Figure 4.2 Cross-sectional TEM images of SBA-15 thin films synthesized on Si substrates at four withdrawal speeds: (a) 0.02, (b) 0.5, (c) 1.0, and (d) 3.0  $\text{mm s}^{-1}$ .

### 4.3.2 X-ray reflectivity (XRR) measurements

To measure the average film thicknesses of the SBA-15 thin films, we performed XRR measurements. The XRR patterns were analyzed using the GlobalFit software (RIGAKU), and the average thickness of a  $5 \text{ mm} \times 5 \text{ mm}$  area of the SBA-15 thin films was calculated by comparing the periodic vibration,  $\Delta\theta$ , of the XRR spectrum with simulated patterns within  $2\theta < 2^\circ$ . Figure 4.3(a) shows

XRR patterns of SBA-15 thin films synthesized on Si substrates at seven different withdrawal speeds: 0.02, 0.05, 0.1, 0.2, 0.5, 1.0, and 3.0 mm s<sup>-1</sup>. The critical angle (peak of intensity value at about 0.4°),  $\theta_c$ , describes the density of materials. Higher frequency oscillations correspond to a thicker film of mesoporous silica. The measured XRR patterns show that the frequency was the lowest at 0.2 mm s<sup>-1</sup> and increased with either an increase or decrease in withdrawal speed.

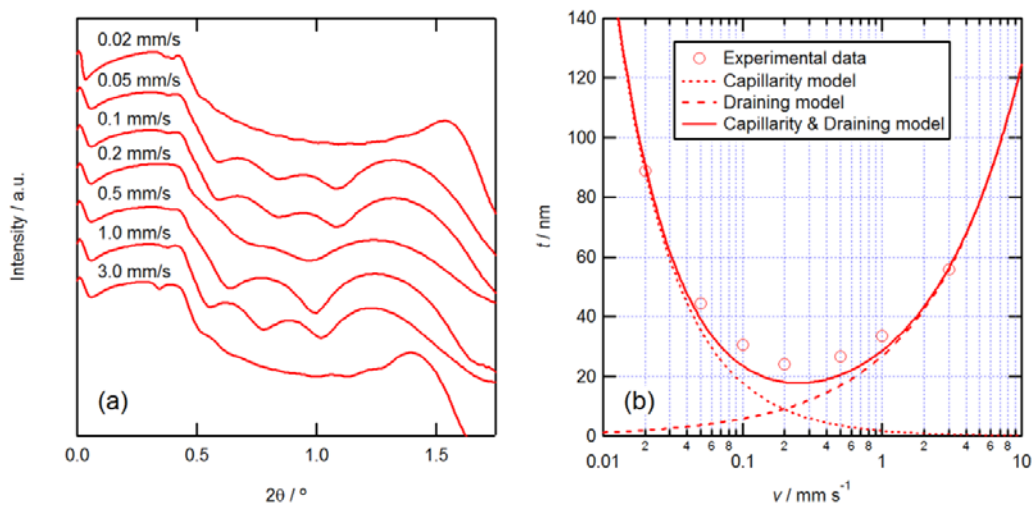


Figure 4.3 (a) XRR patterns of SBA-15 thin films synthesized on Si substrates at withdrawal speeds: 0.02, 0.05, 0.1, 0.2, 0.5, 1.0, and 3.0 mm s<sup>-1</sup>. (b) Film thickness versus withdrawal speed plots.

Figure 4.3(b) shows plots of the film thickness versus withdrawal speeds for seven different withdrawal speeds. The measured and calculated thicknesses were 88.9, 44.4, 30.6, 24.0, 26.6, 33.6, and 55.7 nm for films with withdrawal speeds of 0.02, 0.05, 0.1, 0.2, 0.5, 1.0, and 3.0 mm s<sup>-1</sup>, respectively. Figure 4.3(b) also shows the prediction curves from semi-empirical models proposed by Faustini et al. [24] Details relevant to semi-empirical model will be explained in

Chapter 4.4. These models comprise two different models, i.e., capillarity and draining models, that correspond to ultraslow and fast withdrawal speeds, respectively. The prediction curves from these two models were determined using experimental data for the thicknesses of films produced at withdrawal speeds of 0.02 and 3.0 mm s<sup>-1</sup>, respectively. We confirmed that the linear combination of these two models can predict the film thicknesses at intermediate withdrawal speeds of 0.05–1.0 mm s<sup>-1</sup>.

### 4.3.3 X-ray diffraction (XRD) measurements

We also performed XRD measurements to confirm the formation of SBA-15 films with hexagonally arrayed pores. Figure 4.4(a) shows out-of-plane XRD patterns of SBA-15 thin films synthesized on Si substrates at seven different withdrawal speeds: 0.02, 0.05, 0.1, 0.2, 0.5, 1.0, and 3.0 mm s<sup>-1</sup>. These XRD patterns are in good agreement with previously reported patterns [5, 10, 16, 35]. The diffraction patterns of the SBA-15 films produced at withdrawal speeds of 0.02 and 3.0 mm s<sup>-1</sup> feature intense peaks with  $d$  values of 6.3 nm (100) and 3.2 nm (200), which indicate the formation of a 2D hexagonal mesostructure parallel to the substrate.

Figure 4.4(b) shows the interplanar spacings of the (100) planes that were obtained from the first peak in the corresponding XRD pattern versus withdrawal speed for seven different withdrawal speeds. The measured  $d(100)$  values for withdrawal speeds of 0.02, 0.05, 0.1, 0.2, 0.5, 1.0, and 3.0 mm s<sup>-1</sup> were 6.27, 6.76,

7.08 , 7.60, 7.24, 7.03, and 6.33 nm, respectively. The results show that the interplanar spacing of the (100) planes decrease with increasing film thickness. The  $d(100)$  values measured from the TEM images were slightly smaller than those of the FE-SEM images and XRD patterns. However, all the results feature similar trends.

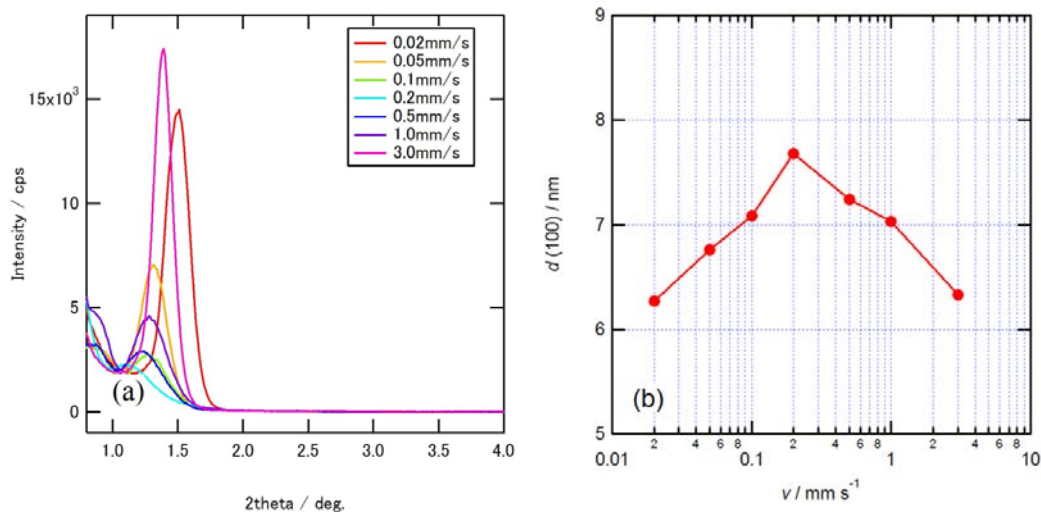


Figure 4.4 (a) XRD patterns of SBA-15 thin films synthesized on Si substrates at seven different withdrawal speeds: 0.02, 0.05, 0.1, 0.2, 0.5, 1.0, and 3.0 mm s<sup>-1</sup>. (b) Plots of the interplanar distance [ $d(100)$ ] versus withdrawal speed.

## 4.4 Model of the thickness of films synthesized by dip-coating

### 4.4.1 Film thickness in the capillarity regime

From the mass-conservation law, the rate of film formation,  $F$  (m<sup>3</sup> s<sup>-1</sup>), can be related to the rate of solution feeding to the upper zone of the meniscus, which is directly related to the rate of solvent evaporation,  $E$  (m<sup>3</sup> s<sup>-1</sup>), as follows:

$$\alpha\rho F = cME, \quad (4.1)$$

where  $c$  ( $\text{mol L}^{-1}$ ) is the inorganic molar concentration of a solution,  $M$  ( $\text{g mol}^{-1}$ ) is the molar weight,  $\alpha$  is the volume fraction of inorganic material, and  $\rho$  ( $\text{g cm}^{-3}$ ) is the density of the thermally stabilized inorganic material. The rate of film formation is also given by

$$F = Ltv, \quad (4.2)$$

where  $L$  and  $t$  are the width and thickness of the final film, respectively, and  $v$  is the withdrawal speed. From Eq. 4.1 and 4.2, the thickness of the film,  $t$ , is given by

$$t = (cME/\alpha\rho L)v^{-1} = C_1v^{-1}, \quad (4.3)$$

where  $C_1$  is the coefficient, which is determined using  $C_1 = cME/\alpha\rho L$ . By substituting  $t = 89.9 \text{ nm}$  and  $v = 0.02 \text{ mm s}^{-1}$  into Eq. 3, the coefficient,  $C_1$ , was calculated to be  $1.778 \times 10^{-12} \text{ m}^2 \text{ s}^{-1}$ .

#### 4.4.2 Film thickness in the draining regime

At fast withdrawal speeds, the formation of a film is usually described by the Landau-Levich equation [14]. In this equation, the fluid thickness,  $t$ , is given by

$$t = 0.94l_c \text{Ca}^{2/3}, \quad (4.4)$$

where  $l_c [(\gamma/\rho g)^{1/2}]$  is the capillary length and  $\text{Ca} [\eta v/\gamma]$  is the capillary number. Here,  $\eta$ ,  $\gamma$ , and  $\rho$  are the viscosity, surface tension, and density of the fluid, respectively, while  $g$  is the gravitational acceleration. The final film thickness,  $t$ , is given by

$$t = C_2 v^{2/3} . \quad (4.5)$$

where  $C_2$  is the coefficient. By substituting  $t = 55.7$  nm and  $v = 3.0$  mm s<sup>-1</sup> into Eq. 4.5, the coefficient,  $C_2$ , was calculated to be  $2.677 \times 10^{-6}$  m<sup>1/3</sup> s<sup>2/3</sup>.

#### 4.4.3 Combined model

From equations (4.3) and (4.5), the film thickness,  $t$ , can be expressed as

$$t = C_1 v^{-1} + C_2 v^{2/3} . \quad (4.6)$$

Specifically,

$$t [\text{m}] = (1.778 \times 10^{-12} [\text{m}^2 \text{s}^{-1}]) \times (v [\text{m s}^{-1}])^{-1} + (2.677 \times 10^{-6} [\text{m}^{1/3} \text{s}^{2/3}]) \times (v [\text{m s}^{-1}])^{2/3} .$$

#### 4.5 1D Alignments and 2D hexagonal arrays of pores

Experimentally, as shown in Figure 4.1, the mesoporous silica thin films formed at various withdrawal speeds feature two-dimensional hexagonal pore structures. However, the pores in the film produced with a withdrawal speed of 0.02 mm s<sup>-1</sup> were not as perfectly arrayed as those in films with withdrawal speeds of 0.5, 1.0, and 3.0 mm s<sup>-1</sup>. This occurs because the mesostructure in the film depends on the evaporation rate during the self-assembly process. The deposition processes between evaporation regime and Landau-Levich regime is completely different, resulting in the evaporation rate difference under same conditions such as temperature and relative humidity (RH). Figure 4.5 shows (a) the dip-coating and (b) thin film deposition process in evaporation regime,

withdrawal speed  $V < V_{crit}$ .

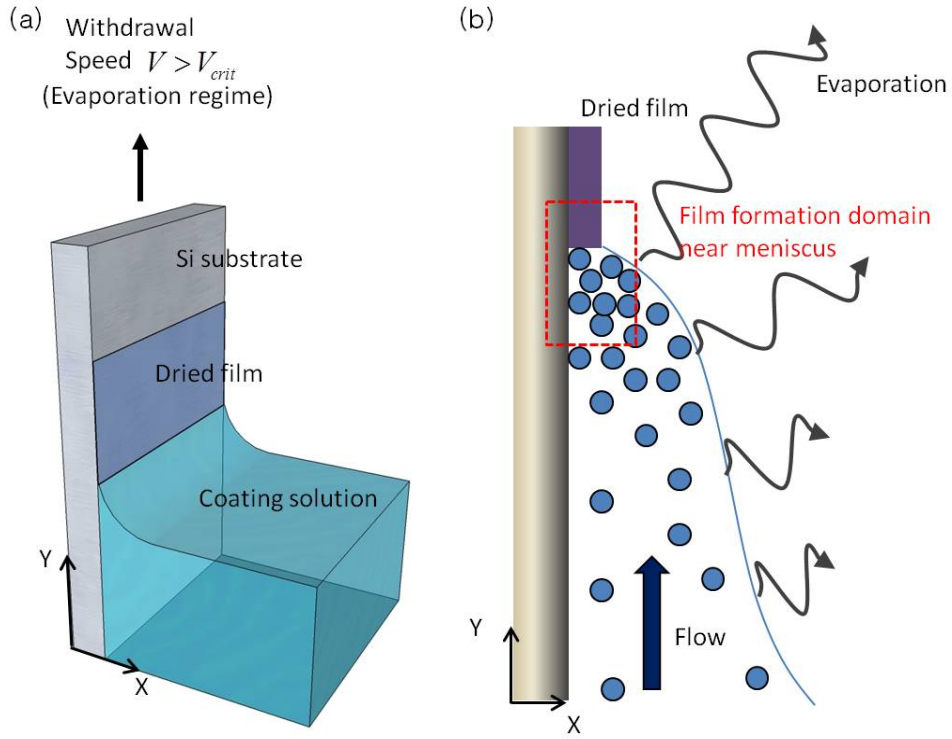


Figure 4.5 The dried film deposited above the meniscus by dip-coating (a) and thin film deposition process in evaporation regime (b).

$V_{crit}$  is a critical speed at which the thin film thickness is minimized. At low speed, the inorganic precursors and the surfactant mesophase accumulate at the contact line (the tip of meniscus) due to evaporation-induced flow and form a dried film just above the meniscus. In dip-coating system, unlike the coffee-ring-effect, because the edge of film is not pinned, it recedes as drying process proceeds. As a result, upward flux of organic/inorganic molecules is caused to replenish those deposited onto the substrate. The red dotted box implies film formation domain as shown in Figure 4.5(b).

However, the local evaporation flux occurring around meniscus depends on the curvature and contact angle [26,27]. If the contact angle is  $90^\circ$ , the evaporation rate is uniform across the entire surface. In contrary, in the case of lower contact angle, the evaporative flux is enhanced at the edge of the film. In this study, since wetting solvent such as ethanol was used, the contact angle should be receding angle as the substrate was withdrawn. Therefore, it is found that the local evaporation rate is higher at the edge of the film, compared to the flat region of the film such as the liquid film dragged out in Landau-Levich regime. Indeed, the degree of silica condensation plays a critical role in formation of the mesostructure by the self-assembly and is influenced by the environmental condition such as temperature, relative humidity, and evaporation rate during dip-coating process. When the evaporation is too fast, it can lead to higher viscosity in the liquid film and thus disrupt complete self-assembly of silica precursors and surfactant mesophase due to a shorter period of time to organize [36].

To better understand the difference of deposition process between the evaporation regime and Landau-Levich regime, we synthesized the SBA-15 thin film at RH 40% and 298 K inside a glove box. Figure 4.6 shows cross-sectional FE-SEM images of SBA-15 thin films synthesized on Si substrates at 0.02 and 3.0  $\text{mm s}^{-1}$  at RH 40%. In case of the RH 40%, the evaporation rate will be further promoted compared with that of RH 60% (as shown in Figure 4.1).

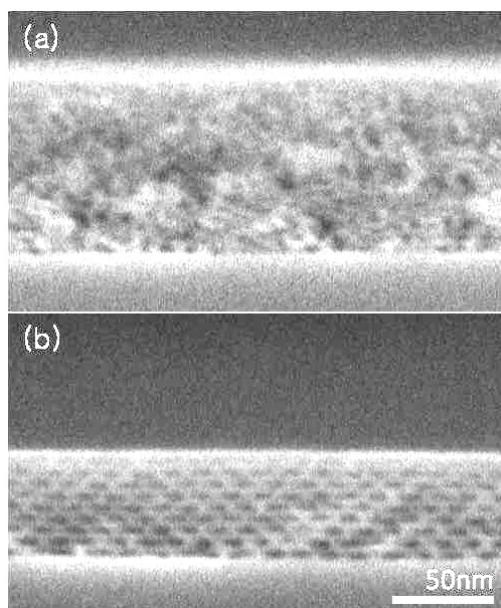


Figure 4.6. Cross-sectional FE-SEM images of SBA-15 thin films synthesized on Si substrates at (a)  $0.02$  and (b)  $3.0 \text{ mm s}^{-1}$  under RH 40%.

The thickness of thin film formed at  $0.02 \text{ mm s}^{-1}$  is similar to RH 60%, but the structure is poorly ordered. In contrast, the corresponding film at  $3.0 \text{ mm s}^{-1}$  looks almost identical to that of RH 60%. Therefore, the higher viscosity due to predominant evaporation rate at the edge of the film at low speed prevents poorly condensed inorganic network surrounding surfactant mesophase from facile rearrangement, thus resulting in the disordered structure.

At withdrawal speeds of  $0.5$  and  $1.0 \text{ mm s}^{-1}$ , the local pore array was well controlled, but the film was too thin; therefore, it could be difficult to form the thin film over the entire surface of the Si substrate and to align the pores in one direction. At a withdrawal speed of  $3.0 \text{ mm s}^{-1}$ , both the global one-dimensional pore alignment and the local two-dimensional hexagonal pore array were achieved

because a thin film of dilute solution was formed uniformly and the micelle self-assembly proceeded slowly.

#### **4.6 Interplanar spacing and pore sizes**

It has been reported that denser films are formed at a slower dip-coating speed (in the capillarity regime), as determined from the relative refractive indices measured by ellipsometry, since more time is available for the inorganic materials to arrange into more compact structures [24]. The drying process is likely dependent on the liquid film thickness: As the liquid film thickness increases, it should dry more slowly and stay in a modifiable steady state for a longer period. As a result, the films could have more compact structures.

For ultrathin films, the films dry too quickly to age the inorganic species and complete micelle self-assembly [18,19,36]. As a result, the interplanar spacing increases and well-defined pore structures are not formed over the entire surface of the Si substrate. The FE-SEM and TEM images and XRR and XRD patterns of the synthesized thin films reflect this trend. Furthermore, to clarify the effect of calcination on the compact structure, the interplanar spacing of  $d(100)$  was measured before the calcination. The measured  $d(100)$  values for withdrawal speeds of 0.02, 0.05, 0.1, 0.2, 0.5, 1.0, and 3.0  $\text{mm s}^{-1}$  were 8.7, 10.19, 10.37, 10.23, 10.17, 9.89 and 9.0 nm, respectively. The reduction ratio of interplanar spacing of  $d(100)$  between before and after calcination was about 30% in all withdrawal speeds. It is fair to say that the correlation between the interplanar

spacing of  $d(100)$  and the withdrawal speed was determined by the dip-coating process.

In general, the pore size distribution of mesoporous silica can be determined from  $N_2$  or Ar adsorption data using Barrett-Joyner-Halenda (BJH), Dollimore-Heal (DH), or nonlocal density functional theory (NLDFT) methods. However, the  $N_2$  adsorption–desorption isotherm measurement could not be applied to the characterization of pore-size distribution inside the thin films because it was difficult to acquire a sufficient amount of sample for the measurement. Therefore, we evaluated the out-of-plane pore radius from the cross-sectional TEM images. Figure 4.7 shows a magnified cross-sectional TEM image of a SBA-15 mesoporous silica thin film synthesized on a (100)-oriented Si substrate at a withdrawal speed of  $0.5 \text{ mm s}^{-1}$ . The direct magnification was 500 000.

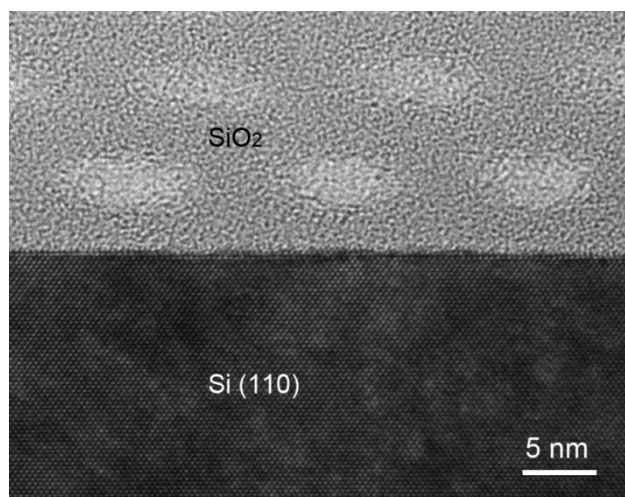


Figure 4.7 Cross-sectional TEM image of a SBA-15 mesoporous silica thin film synthesized on a (100)-oriented Si substrate at a withdrawal speed of  $0.5 \text{ mm s}^{-1}$ . The direct magnification was 500 000.

In the TEM images, the pore geometry appeared to be elliptical. Since the in-plane radius includes the geometrical features of mesopores, such as bending and twisting, the out-of-plane radius was evaluated; the measured values were 0.90, 1.62, 1.37, and 1.05 nm for withdrawal speeds of 0.02, 0.5, 1.0, and 3.0 mm s<sup>-1</sup>, respectively. The out-of-plane radius and interplanar spacing show similar trends with respect to the withdrawal speed: As the film thickness increases, both the out-of-plane radius and interplanar spacing decrease, yielding more compact structures. Furthermore, in Figure 4.7, the interpore distance in the tangential direction to the substrate also show similar trends with respect to the withdrawal speed; the measured values were 12.4, 13.5, 12.9, and 12.7 nm for withdrawal speeds of 0.02, 0.5, 1.0, and 3.0 mm s<sup>-1</sup>, respectively. As the film thickness increases, more compact structures can be attained in the tangential direction to the substrate. Because a SBA-15 mesoporous silica thin film was perfectly contacted with a Si substrate and neither gap nor void was formed at the interface as shown in Figure 4.7, the compact structure in the tangential direction to the substrate could be formed in the micelle self-assembly process not in the calcination process.

#### **4.7 Interplanar spacing of $d(100)$ before and after calcination**

The thickness of mesoporous silica thin films decreased after calcination. Figure 4.8 shows the cross-sectional FE-SEM images of before and after calcination of a SBA-15 thin film synthesized at a withdrawal speed of 3.0 mm s<sup>-1</sup>.

The interplanar spacing of  $d(100)$  was obtained from the first peak position of (100) in the XRD pattern of SBA-15 thin films synthesized on Si substrates. Figure 4.9 shows the plots of the interplanar distance [ $d(100)$ ] versus withdrawal speed before and after calcination. The results are also summarized in Table 4.1.

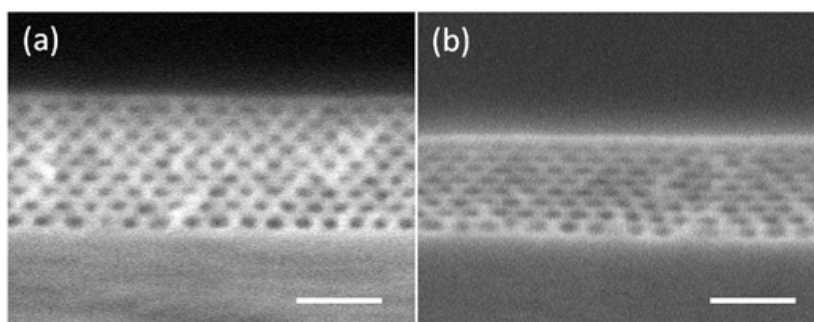


Figure 4.8 Cross-sectional FE-SEM images of (a) before and (b) after calcination of a SBA-15 thin film synthesized on Si substrates at a withdrawal speed of  $3.0 \text{ mm s}^{-1}$ . The scale bar is 50 nm.

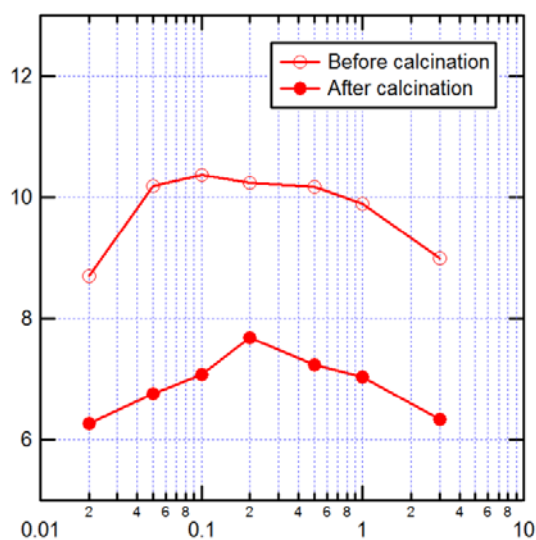


Figure 4.9 Plots of the interplanar distance [ $d(100)$ ] versus withdrawal speed before and after calcination.

Table 4.1 The interplanar spacing of  $d(100)$  in the XRD patterns of films produced at different withdrawal speeds before and after calcinations.

Withdrawal Speed (mm s <sup>-1</sup> )	Before $d(\text{nm})$	After $d(\text{nm})$	Reduction ratio $d_{\text{after}}/d_{\text{before}}$
0.02	8.7	6.27	0.72
0.05	10.19	6.74	0.66
0.1	10.37	7.08	0.68
0.2	10.23	7.60	0.74
0.5	10.17	7.24	0.71
1.0	9.89	7.03	0.71
3.0	9.0	6.33	0.70

## 4.8 Conclusion

In this study, we synthesized two-dimensional hexagonal mesoporous silica SBA-15 thin films via dip-coating and investigated the influences of withdrawal speeds in the range 0.02–3.0 mm s<sup>-1</sup> on the film thickness and pore array using FE-SEM, TEM, XRD, and XRR analyses. The following conclusions could be drawn from this study:

1. The film thickness increased with increasing withdrawal speed and also increased after decreasing the withdrawal speed to the ultraslow region where capillary rise of the solution occurs. The film thickness was minimized at an intermediate withdrawal speed. At intermediate withdrawal speeds of 0.05–1.0 mm s<sup>-1</sup>, the local two-dimensional hexagonal pore array was well controlled,

but the film was too thin; therefore, it could be difficult to form the thin film over the entire surface of the Si substrate and to align the pores in one direction.

2. The pores in the film produced with a ultraslow withdrawal speed of  $0.02 \text{ mm s}^{-1}$  were not as perfectly two-dimensional hexagonal arrayed as those in films with higher withdrawal speeds. Because the condensation of the silica solution and the formation of the thin film occurred simultaneously just around the meniscus, the copolymer micelles were arrayed in a more concentrated and viscous solution.
3. The interplanar spacing and pore size decreased with increasing withdrawal speed and also decreased upon decreasing the withdrawal speed to the ultraslow region. The interplanar spacing and pore size were maximized at an intermediate withdrawal speed. As the liquid-film thickness increases, the liquid film dries more slowly and thus remains in a modulable steady state for a longer period. As a result, the films have more compact structures.
4. The films produced at a withdrawal speed of  $3.0 \text{ mm s}^{-1}$  featured the most perfect pore structure of the global one-dimensional pore alignment and local two-dimensional hexagonal pore array because a thin film of dilute solution was formed uniformly and the micelle self-assembly proceeded slowly.

## 4.9 Reference

1. Kresge, C.; Leonowicz, M.; Roth, W.; Vartuli, J.; Beck, J. Ordered Mesoporous Molecular Sieves Synthesized by a Liquid-Crystal Template Mechanism. *Nature* **1992**, *359*, 710-712.
2. Beck, J.; Vartuli, J.; Roth, J.; Leonowicz, M.; Kresge, C.; Schmit, K.; Chu, C.; Sheppard, E.; McCullen, S.; Higgins, J.; Schlenker, J. A New Family of Mesoporous Molecular Sieves Prepared with Liquid Crystal Templates. *J. Am. Chem. Soc.* **1992**, *114*, 10834–10843.
3. Ariga, K.; Vinu, A.; Yamaguchi, Y.; Ji, Q.; Hill, J. Nanoarchitectonics for Mesoporous Materials. *Bull. Chem. Soc. Jpn.* **2012**, *85*, 1-32.
4. Zhao, D.; Yang, P.; Margolese, D.; Chmelka, B.; Stucky, G. Synthesis of Continuous Mesoporous Silica Thin Films with Three-Dimensional Accessible Pore Structures. *Chem. Commun.* **1998**, 2499-2500.
5. Zhao, D.; Feng, J.; Huo, Q.; Melosh, N.; Fredrickson, G.; Chmelka, B.; Stucky, G. Triblock Copolymer Syntheses of Mesoporous Silica with Periodic 50 to 300 Angstrom Pores. *Science* **1998**, *279*, 548-552.
6. Kimura, T.; Itoh, D.; Okazaki, N.; Kaneda, M.; Sakamoto, Y.; Terasaki, O.; Sugahara, Y.; Kuroda, K. Lamellar Hexadecyltrimethylammonium Silicates Derived from Kanemite. *Langmuir* **2000**, *16*, 7624-7628.
7. Sakamoto, Y.; Kaneda, M.; Terasaki, O.; Zhao, D.; Kim, J. M.; Stucky, G.; Shin, H. J.; Ryoo, R. Direct Imaging of the Pores and Cages of Three-Dimensional Mesoporous Materials. *Nature* **2000**, *408*, 449-453.
8. Brinker, C.; Lu, Y.; Sellinger, A.; Fan, H. Evaporation-Induced Self-Assembly: Nanostructures Made Easy. *Adv. Mater.* **1999**, *11*, 579-585.
9. Vartuli, J.; Schmitt, K.; Kresge, C.; Roth, W.; Leonowicz, M.; McCullen, S.; Hellring, J.; Beck, J.; Schlenker, J.; Olson, D.; Sheppard, E. Effect of Surfactant/Silica Molar Ratios on the Formation of Mesoporous Molecular sieves: Inorganic Mimicry of Surfactant Liquid-Crystal Phases and Mechanistic Implications. *Chem. Mater.* **1994**, *6*, 2317-2326.
10. Zhao, D.; Sun, J.; Li, Q.; Stucky, G. Morphological Control of Highly Ordered Mesoporous Silica SBA-15. *Chem. Mater.* **2000**, *12*, 275-279.

11. Fan, R.; Huh, S.; Yan, R.; Arnold, J.; Yang, P. Gated Proton Transport in Aligned Mesoporous Silica Films. *Nat. Mater.* **2008**, *7*, 303-307.
12. Bearzotti, A.; Bertolo, J.; Innocenzi, P.; Falcaro, P.; Traversa, E. Humidity Sensors Based on Mesoporous Silica Thin Films Synthesized by Block Copolymers. *J. Eur. Ceram. Soc.* **2004**, *24*, 1969-1972.
13. Sakai, H.; Baba, R.; Hashimoto, K.; Fujishima, A.; Heller, A. Local Detection of Photoelectrochemically Produced H<sub>2</sub>O<sub>2</sub> with a “Wired” Horseradish Peroxidase Microsensor. *J. Phys. Chem.* **1996**, *99*, 11896-11900.
14. Tamagawa, C.; Schiller, P.; Polla, D. Pyroelectric PbTiO<sub>3</sub> Thin Films for Microsensor Applications. *Sens. Actuators A* **1992**, *35*, 77-83.
15. Li, W.; Xie, S.; Qian, L.; Chang, B.; Zou, B.; Zhou, W.; Zhao, R.; Wang, G. Large-Scale Synthesis of Aligned Carbon Nanotubes. *Science* **1996**, *274*, 1701-1703.
16. Wu, C.; Yamaguchi, Y.; Ohsuna, T.; Kuroda, K. Structural Study of Highly Ordered Mesoporous Silica Thin Films and Replicated Pt Nanowires by High-Resolution Scanning Electron Microscopy (HRSEM). *J. Mater. Chem.* **2006**, *16*, 3091-3098.
17. Grosso, D.; Cagnol, F.; Soler-Illia, G.; Crepaldi, E.; Amenitsch, H.; Brunet-Bruneau, A.; Bourgeois, A.; Sanchez, C. Fundamentals of Mesostructuring through Evaporation-Induced Self-Assembly. *Adv. Funct. Mater.* **2004**, *14*, 309-322.
18. Brinker, C.; Frye, G.; Hurd, A.; Ashley, C. Fundamentals of Sol–Gel Dip Coating. *Thin Solid Films* **1991**, *201*, 97-108.
19. Brinker, C.; Hurd, A.; Schunk, P.; Frye, G.; Ashley, C. Review of Sol–Gel Thin Film Formation. *J. Non-Cryst. Solids* **1992**, *147-148*, 424-436.
20. Landau, L.; Levich, B. Dragging of a Liquid by a Moving Plate. *Acta Physicochim. URSS* **1942**, *17*, 42-54.
21. Berre, M.; Chen, Y.; Baigl, D. From Convective Assembly to Landau-Levich Deposition of Multilayered Phospholipid films of Controlled Thickness. *Langmuir* **2009**, *25*, 2554-2557.
22. Deegan, R.; Bakajin, O.; Dupont, G.; Nagel, S.; Witten, T. Capillary flow as the cause of ring stains from dried liquid drops. *Nature* **1997**, *389*, 827-829.
23. Deegan, R.; Bakajin, O.; Dupont, T.; Huber, G.; Nagel, S.; T., W. Contact line deposits in a evaporating drop. *Phys. Rev. E* **2000**, *62*, 756-765.

24. Faustini, M.; Louis, B.; Albouy, P. A.; Kuemmel, M.; Grosso, D. Preparation of Sol–Gel Films by Dip-Coating in Extreme Conditions. *J. Phys. Chem. C* **2010**, *114*, 7637-7645.
25. Berteloot, G.; Pham, C.-T.; Daerr, A.; Lequeux, F.; Limat, L. Evaporation-induced flow near a contact line: Consequences on coating and contact angle. *Europhys. Lett.* **2008**, *83*, 14003.
26. Popov, Y. Evaporative deposition patterns: Spatial dimensions of the deposit. *Phys. Rev. E* **2005**, *71*, 036313.
27. Routh, A. Drying of thin colloidal films. *Rep. Prog. Phys.* **2013**, *76*, 046603.
28. Wu, C.; Ohsuna, T.; Edura, T.; Kuroda, K. Orientational Control of Hexagonally Packed Silica Mesochannels in Lithographically Designed Confined Nanospaces. *Angew. Chem. Int. Ed.* **2007**, *46*, 5367-5368.
29. Trau, M.; Yao, N.; Kim, E.; Xia, Y.; Whitesides, G.; Aksay, I. Microscopic Patterning of Orientated Mesoscopic Silica through Guided Growth. *Nature* **1997**, *390*, 674-676.
30. Daiguji, H.; Tatsumi, N.; Kataoka, S.; Endo, A. One-Dimensional Alignment of SBA-15 Films in Microtrenches. *Langmuir* **2009**, *25*, 1121-1124.
31. Kawashima, Y.; Nakagawa, M.; Seki, T.; Ichimura, K. Photo-orientation of Mesosstructured Silica via Hierarchical Multiple Transfer. *Chem. Mater.* **2002**, *14*, 2842-2844.
32. Walcarius, A.; Sibottier, E.; Etienne, M.; Ghanbaja, J. Electrically Assisted Self-Assembly of Mesoporous Silica Thin Films. *Nature* **2007**, *6*, 602-608.
33. Yamaguchi, Y.; Sawada, M.; Sugiyama, A.; Osaka, T.; Sakka, Y.; Kuroda, K. Magnetically Induced Orientation of Mesochannels in 2D-Hexagonal Mesoporous Silica Films. *J. Mater. Chem.* **2006**, *3693-3700*, 16.
34. Grosso, D.; Balkenende, A.; Albouy, P.; Ayral, A.; Amenitsch, H.; Babonneau, F. Two-Dimensional Hexagonal Mesoporous Silica Thin Films Prepared from Block Copolymers: Detailed Characterization and Formation Mechanism. *Chem. Mater.* **2001**, *13*, 1848-1856.
35. Zhao, D.; Huo, Q.; Feng, J.; Chmelka, B.; Stucky, G. Nonionic Triblock and Star Diblock Copolymer and Oligomeric Surfactant Syntheses of Highly Ordered, Hydrothermally Stable, Mesoporous Silica Structures. *J. Am. Chem. Soc.* **1998**, *120*, 6024-6036.

36. Cagnol, F.; Grosso, D.; Soler-Illia, G.; Crepaldi, E.; Babonneau, F.; Amenitsch, H.; Sanchez, C. Humidity-Controlled Mesostructuration in CTAB-Templated Silica Thin Film Processing. The Existence of a Modulable Steady State. *J. Mater. Chem.* **2003**, *13*, 61-66.



# CHAPTER 5

## **Ion Transport in Mesoporous Silica SBA-15 Thin Film with Two-Dimensional Hexagonal Structures**

### **5.1 Introduction**

In this chapter, the hybrid top-down and bottom-up fabrication method was employed to employ the synthesized mesoporous silica SBA-15 thin film as a nanofluidic device. However, in the case of SBA-15, there are no access holes to inject an aqueous solution into the nanopores from the top surface of the thin films compared to SBA-16 thin films case. This is, SBA-16 thin films can be integrated with PDMS microfluidic devices without any artificial processing thanks to access naopores due to 3D cubic structure, but this cannot be done with SBA-15 thin films. Therefore, in order to fill SBA-15 thin films with aqueous solution, we need to develop access holes by employing top-down methods such as lithographically sculpting process. With the synthesis of inorganic nanotubular membranes and their integration into nanofluidic devices, we can investigate the ion transport phenomena in the sub-10 nm regime. This chapter focuses on the ion transport (monovalent ion) through mesoporous silica SBA-15 thin film with 2D hexagonal

arrays. When SBA-15 thin films are compared to SBA-16 thin films, a different behavior was observed.

## **5.2 Fabrication of nanofluidic device**

The nanofluidic device was fabricated by aligning a PDMS microfluidic chip with a patterned mesoporous silica SBA-15 thin film. Figure 5.1 shows the fabrication process of nanofluidic device embedded mesoporous silica SBA-15 thin film. All the procedures associated with MEMS mentioned above were conducted in AIST Nano-Processing Facility (NPF). First, the SBA-15 thin film synthesized at a dip-coating rate of  $\sim 3 \text{ mm s}^{-1}$  were coated with a layer of  $\sim 6.5 \mu\text{m}$  thick OFPR-800 30cP photoresist using a spin-coater, exposed using maskless arbitrary optical pattern generator to form the square pattern ( $1000 \mu\text{m} \times 100 \mu\text{m}$ ), and developed with a NMD-3 solution for 90 sec. The photoresist pattern was hard-baked at  $130^\circ\text{C}$  for 5 min to produce a robust masking layer. Second, the square mask patterned SBA-15 thin films were defined by reactive ion etching (SAMCO RIE-200L, Japan) in the  $\text{CF}_4/\text{O}_2$  plasma at 80 W and 5 Pa for 1 min to etch through the entire thickness of SBA-15 thin films. Afterwards, the remaining photoresist layer was stripped off using an acetone remover, then it was rinsed with pure water for 3 min, and finally the sample was hard-baked at  $110^\circ\text{C}$ . Third, a  $\text{SiO}_2$  layer of  $\sim 100 \text{ nm}$  in thickness was deposited onto the entire substrate via plasma chemical vapor deposition (SAMCO PCVD PD-20SS, Japan). Subsequently, the mask pattern process on substrates with deposited  $\text{SiO}_2$  thin

film was conducted to make two reservoirs ( $1200\ \mu\text{m} \times 1500\ \mu\text{m}$ ) around the patterned square. RIE process on SBA-15 thin films with deposited a  $\text{SiO}_2$  layer of  $\sim 100\ \text{nm}$  in thickness was performed in the  $\text{CF}_4/\text{O}_2$  plasma at 80 W and 5 Pa for 2 min to etch a  $\text{SiO}_2$  layer and sequentially in the  $\text{SF}_6/\text{O}_2$  plasma at 80 W and 5 Pa for 8 min to etch a Si substrates.

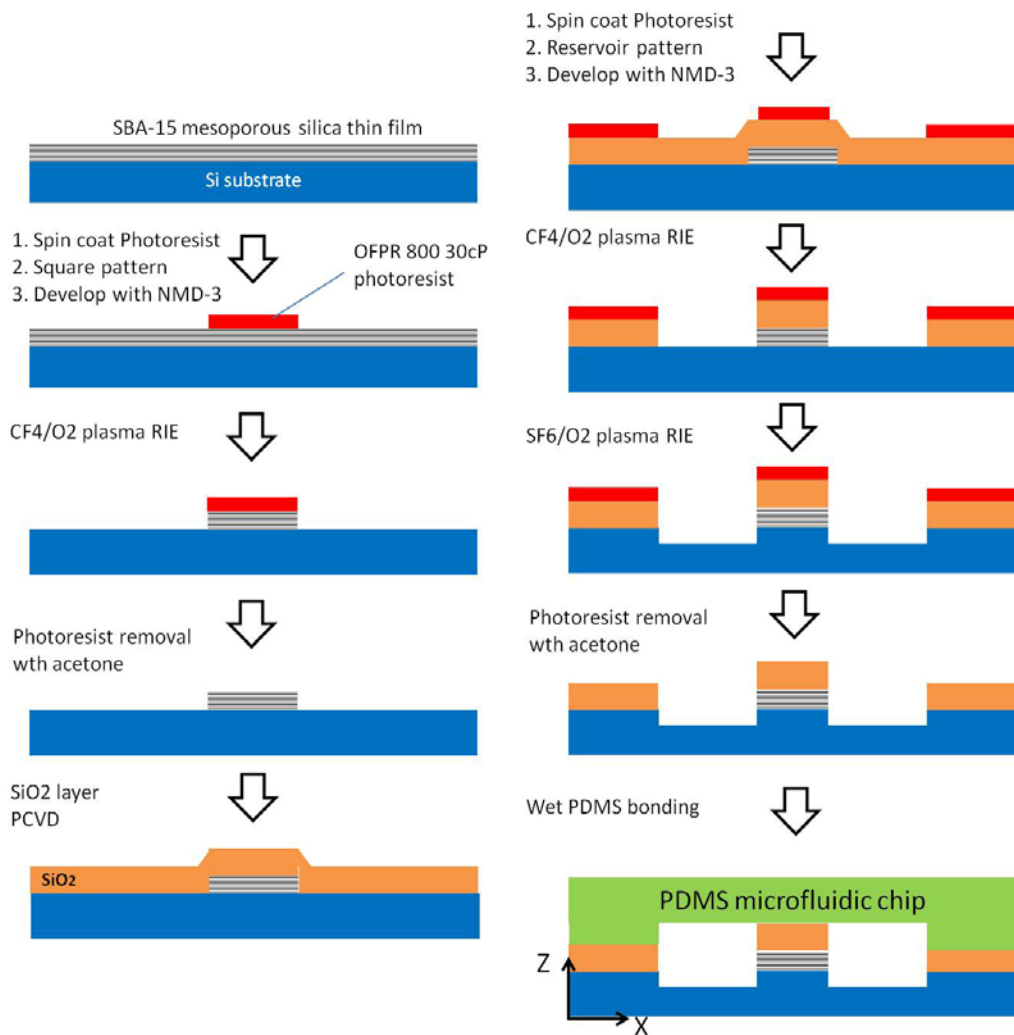


Figure 5.1 Fabrication process flow of nanofluidic device embedded mesoporous silica SBA-15 thin film.

Figure 5.2 shows the schematic of the nanofluidic device layout before bonding the PDMS microfluidic chip. The completed device features a one square-shaped mesoporous silica thin film ( $1\text{mm} \times 100\ \mu\text{m}$ ) and two microfluidic reservoirs ( $12\text{mm} \times 15\text{mm}$ ,  $\sim 1\ \mu\text{m}$  in depth) at both sides.

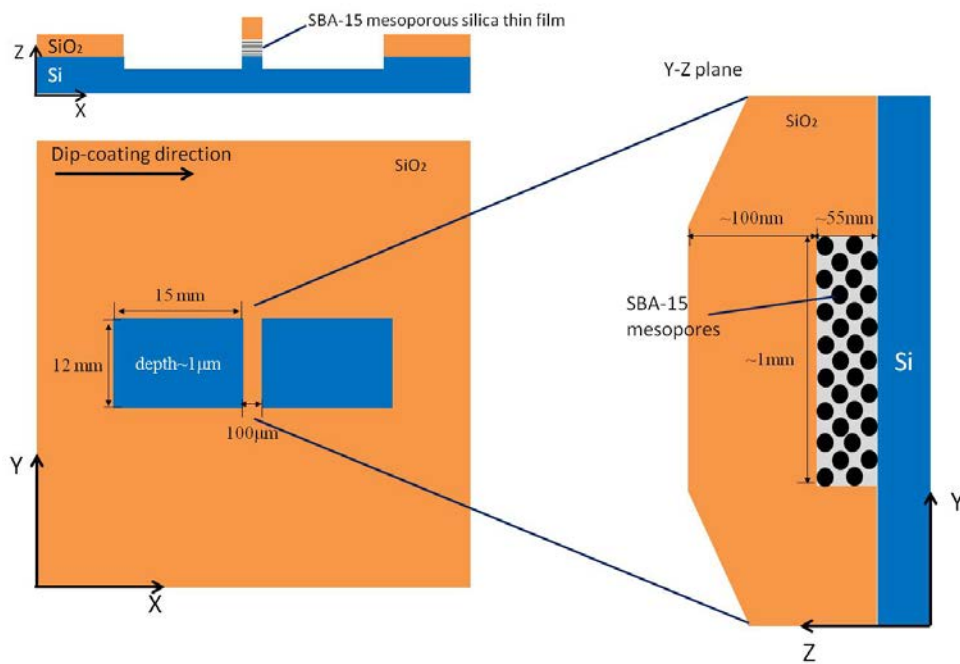


Figure 5.2 Schematic of nanofluidic device layout. A silicon dioxide film deposited onto Si substrate and mesoporous silica thin film is to prevent leakage of aqueous solutions between both reservoirs.

Finally, the PDMS microfluidic chip, which is identical to nanofluidic device of SBA-16 as mentioned in Chapter 2, was bonded onto the mesoporous silica SBA-15 thin film using a wet-PDMS bonding method [1]. First, the PDMS chip was cleaned with isopropanol and pure water assisted by ultrasonication, and the one inlet hole was formed on each PDMS reservoir using a 1 mm-diameter disposable

biopsy punch with a plunger system (Kai Industries Co. Ltd., Japan). Second, a thin layer of wet PDMS monomer/curing agent mixture (10:1) was spun onto a clean silicon substrate for 2 min at 7500rpm to yield a thin layer of wet PDMS (~10  $\mu\text{m}$  in thickness). A layer of wet PDMS was transferred to the feature side of PDMS chip by direct contact. Within half an hour, this PDMS chip was carefully aligned and bonded onto the patterned  $\text{SiO}_2/\text{Si}$  described above using a stereomicroscope (model SMZ-1000, Nikon Instruments Inc., Japan) and a manipulator (Narishige, Japan) to control exquisitely. It was then moved into a convection oven and cured at 80°C for another hour to completely seal the whole device.

Figure 5.3 shows a microscope image (top view) and cross-sectional view of the nanofluidic device chip combined with the PDMS microfluidic chip.

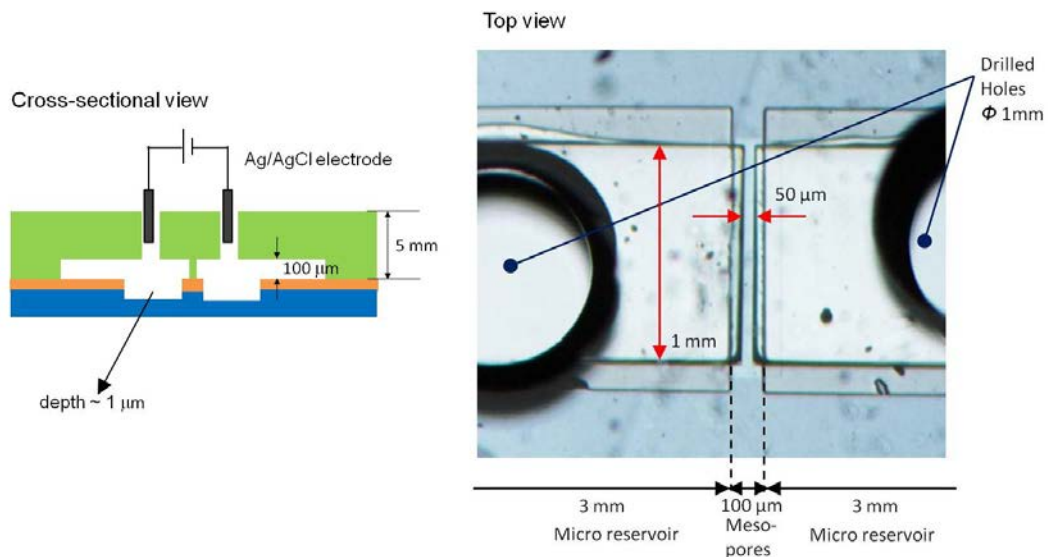


Figure 5.3 Microscope image (top view) and cross-sectional view of the nanofluidic device chip combined with the PDMS microfluidic chip.

The gap between two reservoirs of PDMS chip was smaller ( $\sim 50 \mu\text{m}$ ) compared to the patterned mesoporous silica width ( $\sim 100 \mu\text{m}$ ) to prevent wet PDMS from flowing down.

To increase the wettability and surface charge density in the calcined SBA15 thin film, the mesoporous silica thin film substrate was hydrothermally treated in an autoclave using the vapor of a 0.1M HCl solution at  $120^\circ\text{C}$  for  $\sim 3$ hrs before it was bonded onto PDMS device. This step is critical to restore the silanol group on the inner silica surface such that the nanochannels become sufficiently hydrophilic and allow aqueous solutions to be pulled in via capillary action. This surface activation is critical to improve the effective ion/proton conductivity.

### **5.3 Measurement of ionic current**

Before measuring the ionic current, the reservoirs were filled with KCl aqueous solutions, and then Ag/AgCl electrodes were inserted into each reservoir. An electric potential bias was applied between the two electrodes, and the ionic current passing through the mesopores was measured by an electrochemical research system with the femtoammeter option (Modulab System, Solartron Analytical). Furthermore, all measurements were carried out in a shielding box to eliminate the influence of external electromagnetic waves. Ag/AgCl electrodes, fabricated by a chemical method using a chloride solution (NaClO), were used to measure ionic current. The ionic current measurement was performed in the voltage range from 0 to  $\pm 4.5 \text{ V}$ . The interval of the applied voltage was 0.3 V.

## 5.4 Ionic current–voltage characteristics

The study of the ion transport was performed with different concentrations of KCl solutions. Figure 5.4 shows the measured  $I$ – $V$  curves of KCl aqueous solutions with six different concentrations: (a)  $10^{-5}$ ,  $10^{-4}$ ,  $10^{-3}$  and (b)  $10^{-2}$ ,  $10^{-1}$ , 1M.

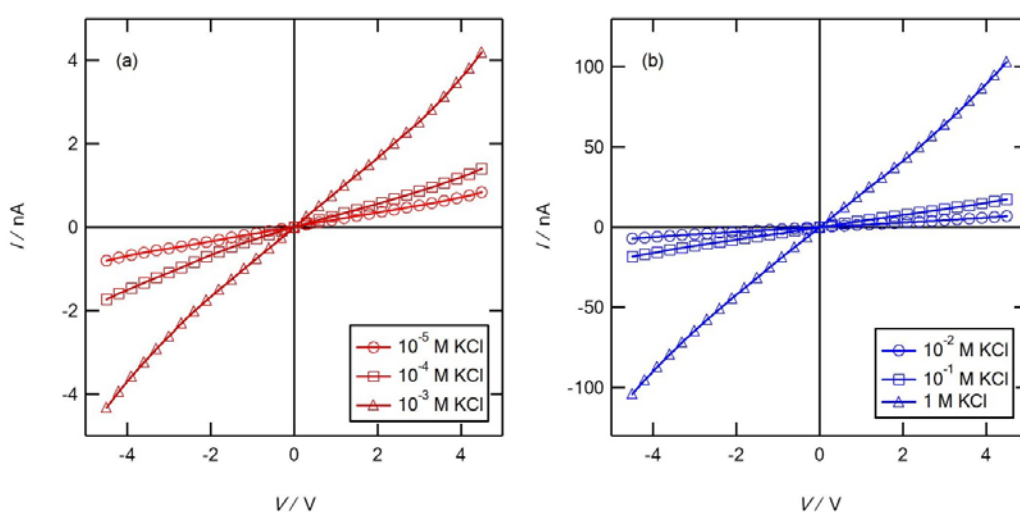


Figure 5.4 Ionic current vs. electric potential bias ( $I$ – $V$ ) curves of an SBA-15 thin film with KCl aqueous solutions with concentrations of (a)  $10^{-5}$ ,  $10^{-4}$ ,  $10^{-3}$  and (b)  $10^{-2}$ ,  $10^{-1}$ , 1M.

The measured  $I$ – $V$  curves were almost symmetric and became linear at all concentrations. The major difference compared with mesoporous silica SBA-16 thin film is that the measured  $I$ – $V$  curves become linear independently of the aqueous solution concentrations, suggesting that the nonlinear behavior of the measured  $I$ – $V$  in SBA-16 thin film could be attributed to the electric potential barrier created in nanopores due to its 3D cubic structure (ink-bottle-like

nanopores). The conductance vs. ion concentration ( $G-n$ ) curve for the SBA-15 thin film device was plotted in Figure 5.5. The conductance decreased with decreasing the ion concentration and it exhibits an apparent deviation from bulk behavior (dashed line) at approximately  $10^{-2}$  M. As in Figure 4.4 of Chapter 4, X-ray diffraction peak on SBA-15 thin film synthesized at  $3.0 \text{ mm s}^{-1}$  detected at  $\sim 1.39^\circ$  and the measured diffraction peak corresponds to the  $d(100)$  spacing,  $\sim 6.33 \text{ nm}$ .

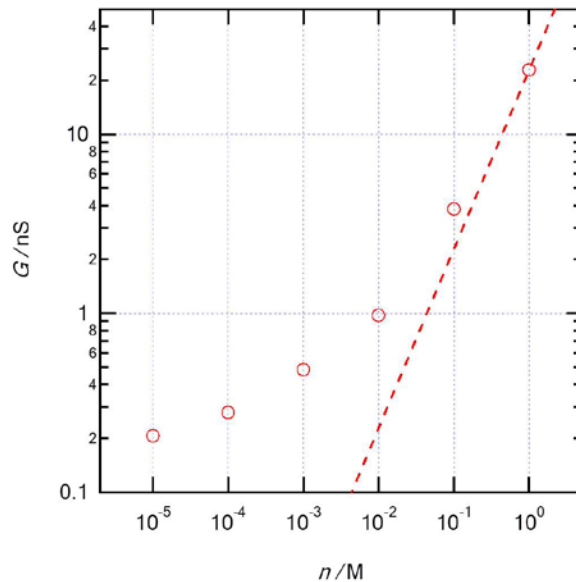


Figure 5.5 Conductance vs. ion concentration ( $G-n$ ) curve.

On the basis of this  $d(100)$  spacing, interpore distance (centre-to-centre) is  $\sim 7.3 \text{ nm}$  using  $d(100)/\cos 30^\circ$  from 2D hexagonal structures as shown in Figure 5.6.

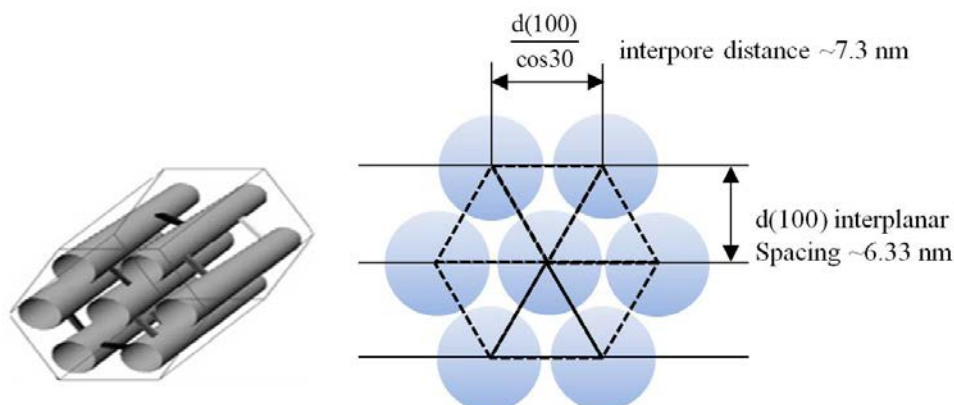


Figure 5.6 Interpore distance of mesoporous silica SBA-15 from 2D hexagonal structures.

Therefore, considering the silica wall thickness, the inner diameter of the mesopores is smaller than  $\sim 7.3$  nm and the nanopores should be almost filled with the electric double layer (EDL) at  $10^{-2}$  M concentration. The Debye characteristic length,  $\lambda_D$ , at 300 K is 96.3, 30.5, 9.6, 3.1, 1.0, and 0.3 nm at  $10^{-5}$ ,  $10^{-4}$ ,  $10^{-3}$ ,  $10^{-2}$ ,  $10^{-1}$ , and 1M KCl, respectively. At  $10^{-5}$ ,  $10^{-4}$ , and  $10^{-3}$  M, the Debye length apparently exceeded the inner diameter of mesopores. The conductance in the low concentration regime (the unipolar regime) was governed by the surface charge density of mesopores, resulting in deviation from bulk behavior not depending on the aqueous solution concentrations. In other words, the surface-governed unipolar regime is expanded around  $10^{-2}$  M in the SBA-15 thin films.

## 5.5 Conclusion

In this chapter, a nanofluidic device with the mesoporous silica SBA-15 thin film was fabricated using traditional MEMS techniques. The ionic currents of KCl aqueous solutions passing through the SBA-15 thin film with 2D hexagonal structures were measured by applying DC electric fields. The measured  $I$ - $V$  curves were almost linear, independent of the aqueous solution concentrations. The conductance deviated from the bulk behavior at approximately  $10^{-2}$  M, and gradually decreased with decreasing aqueous solution concentration.

## 5.6 Reference

1. Satyanarayana, S.; Karnik, R.; Majumdar, A. Stamp-and-stick room-temperature bonding technique for microdevices. *IEEE J. Microelectromechanical Syst.* **2005**, *14*, 392-399.



# CHAPTER 6

## Conclusion

In the last decade the studies associated with transport phenomena in nanofluidic device with channel sizes with a scale comparable to the Debye length ( $\sim 100$  nm) progressed at a fast pace. However, the pace at which the studies of nanofluidics with a characteristic length of less than 10 nm and with complex geometry (e.g. 3D cubic) progress is slower due to difficulties in fabricating the devices and of analysis.

In this thesis, the investigation of ionic conduction in mesoporous silica SBA-16 thin films is one of the objectives. It was observed that, at low ion concentrations, inorganic nanopores with 3D cubic structures and in measuring a few nanometers in diameter showed a nonlinear ionic current behavior ( $I$ - $V$  curve). This is the first study (this thesis) to report these nonlinear findings for inorganic nanochannels/ nanopores. This nonlinearity is due to the fact that the electric potential barrier created in cylindrical nanopores cannot be masked completely by counter-ions, and as a result the ions are either polarized or transported at the electric potential barrier. We found that the dielectric constant around the surface charges and the ion diffusion due to concentration gradients were suppressed when the system is confined to pores measuring a few nanometers in diameter.

The proton transport behavior through the mesopores of SBA-16 showed a considerably different result compared to the nanofluidic systems with dimensions ranging of 10-100nm. When the proton current was measured in surface-governed regime, the conductance generally decreases with increasing the concentrations of the aqueous solution because the surface charge density on the inner surface of mesopores decreases due to the protonation of silanol groups. However, in the case of nanopores of a few nanometers in diameter, the conductance increases in spite of active protonation. Since the dissociated proton and silanol groups were very close to each other, proton close to silanol sites also becomes a charge carrier and might transport by hopping between silanol sites. The electric potential barrier was therefore lowered, but the density of proton did not decrease appreciably, thus increasing the conductance. Such characteristic may be applied in the development of nanopores, such as artificial ion channels and proton exchange membranes (PEM) with complex structures, for smooth proton transport, and could be useful to design 1 nm order structures for sensor, fuel cell and desalination technologies.

Mesoporous silica SBA-15 thin films with dimensions ranging of 5-10 nm and more simple geometry (1D alignment and 2D hexagonal arrays) compared to the SBA-16 thin films were synthesized to investigate the ion or water transport phenomena of aqueous solution confined in mesopores. Because SBA-16 has limitations such as a complex 3D geometry and very small sized nanopores (~2 nm), it is somewhat difficult to apply commonly general conditions. The film

thickness increases when the withdrawal speed is increased, but it also increases when the withdrawal speed is in the ultraslow region where capillary rise of the solution occurs. The film thickness was minimized at an intermediate withdrawal speed. In contrast, the interplanar spacing and pore size decreased with increasing the withdrawal speed and also decreased upon decreasing the withdrawal speed to the ultraslow region. The interplanar spacing and pore size were maximized at an intermediate withdrawal speed. As the liquid-film thickness increases, the liquid film dries more slowly and thus remains in a modulable steady state for a longer period. As a result, the films have more compact structures. In this thesis, the films produced at a withdrawal speed of  $3.0 \text{ mm s}^{-1}$  displayed the best alignment of the local and global pore structures because a thin film of diluted solution formed uniformly and the self-assembly of micelles proceeded slowly, resulting in the best possible condition to synthesize mesoporous silica thin films suitable for transport investigation.

The nanofluidic device with the mesoporous silica SBA-15 thin film was fabricated using traditional MEMS techniques. The ionic conduction of KCl aqueous solutions passing through the SBA-15 thin film was measured by applying DC electric fields. The measured  $I$ - $V$  curves were linear and independent of the concentration of KCl aqueous solutions contrary to the  $I$ - $V$  curves measured in SBA-16 thin films. This is because SBA-15 is unaffected by the electric potential barrier which is due to the complex geometry (3D cubic structures)

In summary, this work focused on the investigation of ion and proton transport phenomena induced by electrostatic interaction in ordered nanoporous structures with nanopores below  $\sim 10$  nm and the development of nanofluidic devices using mesoporous silica materials to perform the field effect manipulation of ion transport. The geometry of the nanopores and the modification of its inner surface charge distribution allow ion transport to have unique features. This thesis makes progress towards understanding the possibility of employing mesoporous silica materials as nanofluidic devices and investigating new phenomena and functionalities observed in mesoporous silica thin films with complex geometry.



## **APPENDIX A: TEM Specimen Preparation techniques**

This APPENDIX A is mainly written out on reference to distributed information associated with TEM specimen preparation technique from Hitachi High-Tech (URL: <http://www.hitachi-hitec.com/group/hms/>).

### **1. Introduction**

Transmission electron microscopy (TEM) is a powerful technique in investigating the micro-/nanostructure of materials, which provide crystallographic information at the nanometer scale [1]. In transmission electron microscopy involved with such studies as mentioned above, since a high-energy beam (~300 keV) is employed with respect to TEM specimen materials, the specimen samples should be transparent (~ a number of nanometers in thickness) to the electron beam. There are several TEM specimen preparation methods for different kind of materials, for instance, i) metals and alloys, ii) multilayers and metallic coatings, iii) nanomaterials, particles/powders, composites and various materials including brittle materials [2]. In this appendix, we will particularly give full details of preparing TEM specimen for cross-sectional view associated with multilayer thin films.

## **2. Methodology for preparing cross-sectional TEM specimens**

### **2.1 Preparation of slices**

The thin film coated is sliced into small rectangular pieces (length ~ 20 mm, width ~ 2.5 mm) using a sharp-edged surgical blade. We might occasionally have trouble cutting the thin film. In such a case, a low-speed diamond wire saw (Buehler Isomet) or Struers Accutom high speed wafering saw can be used to slice with required rectangular. The prepared pieces are cleaned in acetone solution and dried in room temperature.

### **2.2 Preparation of sandwich structures/discs**

A sandwich structures is prepared by bonding two slices with coating layers facing each other. A fast –curing epoxy including a resin and hardener can be used to bond two slices. The epoxy is applied to the surface of coating thin film. While the epoxy sets, the sandwich structure is held with tweezers with some pressure in order to obtain good mechanical bonding between the pieces. The epoxy is applied only one piece to avoid being too thick epoxy layer. After allowing sufficient time for curing (about 2hours), the thickness of the sandwich structure is mechanically polished to ~300  $\mu\text{m}$ . The next step is to cut 3mm discs from the prepared sandwich structures using the ultrasonic cutter (Model Gatan 601) for brittle/hard materials.

### **2.3 Dimple grinding**

Dimpling is performed to reduce the thickness of the disc in the central portion to decrease the time for ion beam thinning process as well as obtaining large regions with electron transparent thicknesses. Samples with the region of interest on one surface, for instance, the coated thin film onto substrate, should be dimpled only from the back side (i.e. the side of substrate). The prepared 3 mm disc is affixed onto the center of the dimple stub with melted wax or cyanoacrylate glue and then, the stub is positioned into the positioning ring on the Gatan Dimple Grinder (Model Gatan 656) for mechanical pre-thinning. Dimpling is performed to a depth of about 50  $\mu\text{m}$  in thickness. After dimpling, the disc is cleaned in acetone for removing the traces of glue.

### **2.4 Ion milling**

The dimpled discs are ion milled for obtaining electron transparent regions. Ion milling is a sputtering process in which energetic ( $\sim 5\text{keV}$ ) neutral atoms and ions from a cathode impinge on the disc or target at an angle. In this work, the Gatan 691 PIPS (Precision Ion Polishing System) is employed to mill the dimpled discs. Ar ion beam was used and the milling angle was  $5^\circ$ . The Gatan PIPS uses higher flux and lower angles, and is designed for short-term milling (within one hour). In the case of requiring low flux and high angle for long-term milling (several hours), the Gatan Duomill can be applied.

### 3. Reference

1. Goodhew, P. *Specimen preparation in Materials Science*; North Holland Publishing Company: New York, 1973.
2. Sridhara Rao, D.; Muraleedharan, K.; Humphreys, C. TEM specimen preparation techniques. *Microscopy: Science, Technology, Application and Education* **2010**, 1232-1244.



# PUBLICATIONS

## Journal papers

1. Hirofumi Daiguji, Junho Hwang, Asuka Takahashi, Sho Kataoka and Akira Endo  
“Ion transport in mesoporous silica SBA-16 thin films with 3D cubic structures” *Langmuir* **28**, 3671–3677, 2012.
2. Junho Hwang and Hirofumi Daiguji  
“Proton transport in mesoporous silica SBA-16 thin films with three dimensional cubic structures” *Langmuir* **29**, 2406–2411, 2013.
3. Junho Hwang, Naoko Shoji, Akira Endo and Hirofumi Daiguji  
“Effect of withdrawal speed on film thickness and hexagonal pore–array dimensions of SBA-15 mesoporous silica thin film” in progress.

## International conferences

1. Junho Hwang and Hirofumi Daiguji  
“Ion transport in mesoporous silica SBA-16 thin films with 3D cubic structures”  
7th US-Japan Joint Seminar on Nanoscale Transport Phenomena –Science and Engineering, Shima, Japan (2011.12)  
Poster Presentation
2. Junho Hwang and Hirofumi Daiguji  
“Ion and proton transport in mesoporous silica SBA-16 thin films with three dimensional cubic structures”  
11th ASME International Conference on Nanochannels, Microchannels and Minichannels (ICNMM2013), Sapporo, Japan (2013.6)  
doi: 10.1115/ICNMM2013-73112

## Other conferences

1. Junho Hwang, Hirofumi Daiguji, Sho Kataoka, Akira Endo  
“Ion transport in mesoporous silica SBA-16 thin films with 3D Cubic structure”  
The Heat Transfer Society of Japan, Toyama, Japan (2012.5)

2. Junho Hwang, Hirofumi Daiguji, Sho Kataoka, Akira Endo  
“Proton transport in mesoporous silica SBA-16 thin films with 3D cubic structures”  
Thermal Engineering Conference 2012, Kumamoto, Japan (2012.11)
3. Naoko Shoji, Junho Hwang, Daisuke Nakayama, Hirofumi Daiguji  
“Structure Control of Mesoporous Silica SBA-15 Thin Films by Dip-Coating Rates”  
Thermal Engineering Conference 2012, Kumamoto, Japan (2012.11)
4. Junho Hwang, Naoko Shoji, Hirofumi Daiguji, Akira Endo  
“Ion transport in mesoporous silica thin films”  
The Heat Transfer Society of Japan, Sendai, Japan (2013.5)
5. Naoko Shoji, Junho Hwang, Hirofumi Daiguji, Akira Endo  
“Structure Control of Mesoporous Silica SBA-15 Thin Films”  
Thermal Engineering Conference 2012, Hirosaki, Japan (2013.10)